UNIVERSITÀ DEGLI STUDI DI TRIESTE

XXIX CICLO DEL DOTTORATO DI RICERCA IN NANOTECNOLOGIE

DIFFERENT APPROACHES FOR THE GROWTH OF GRAPHENE MONOLAYERS

Settore scientifico-disciplinare:FIS\03

DOTTORANDO
Cristian Alexandru TACHE

COORDINATORE
Prof.ssa Lucia PASQUATO

SUPERVISORE
Prof. Alessandro BARALDI

CO-SUPERVISORE
Dr. Silvano LIZZIT

ANNO ACCADEMICO 2015/2016

Abstract

Graphene became one of the most investigated system in the last decade, being considered by the scientific community the wonder material of this century. It is formed from a single layer of carbon atoms packed in a honeycomb lattice with a series of exotic and unique properties which make this system very convenient for engineering new electronic applications. However, besides the outstanding mechanical and electronic properties, graphene has also some serious limitations due to the difficulty in the synthesis of high-quality monolayers at a large scale, or in creating of an electronic band gap in the material, necessary for on-off switching operations in the transistors technology. To overcame this problem, one solution comes from the interaction between epitaxial graphene and transition metal substrates, but this will results in a hardly controlled opening of an energy band gap at a Fermi level. Another solution arises from the possibility to grow a second layer of graphene which will employ a stable band gap.

At present, only the high temperature Chemical Vapour Deposition (CVD) can supply large flakes of free standing graphene to an industrial level, but unfortunately this process is self-limiting to one single graphene layer. Therefore, a different approach is needed for the growth of high quality single- and multi-layer on a large scale to overcome the aforementioned limitations.

My research activity during these three years was focused in developing a new method of growing graphene, beyond the standard CVD. Specifically, we were interested in the molecular beam epitaxy (MBE) growth, where C atoms are directly delivered on the surface. To this purpose, a new solid carbon source was designed and constructed, which is based on the electron bombardment principle to achieve carbon sublimation from a hot graphite rod. This was used on different substrates like Ir(111), where the CVD technique is well established, Ag(111) and $PbZr_{0.2}Ti0.8O_3$ (PZT(001)), a ferroelectric oxide where CVD is precluded. The first part is dedicated to the study of the growth mechanism of graphene on Ir(111) using the carbon (MBE) at a very low substrate temperature (T=80 K) to reduce surface diffusion. This allowed us to assimilate the origin of different species of carbon atoms present in the incipient stage of graphene formation on the Ir(111). We also exploit the possibility to grow a second layer of graphene using the C source, at a high substrate temperature which was impossible to achieve with standard CVD method. The second part is dedicated to the growth of graphene on substrates where, the dissociation of the hydrocarbon molecules used in the CVD is precluded. To this purpose we involved carbon MBE to grow single and double layers on Ag(111) by keeping the substrate at elevated temperature.

The last part of the thesis is dedicated to the graphene ferroelectric oxides interfaces, which can be considered the forward step in the integration of graphene in the new era of electronics. Specifically we were interested in the synthesis of graphene on top of PZT(001 using the solid carbon source, because on this kind of substrate the hydrocarbon used in CVD does not dissociate. A special cleaning procedure was defined to promote carbon adsorption on the substrate. A key role role is played also by the temperature deposition which not may exceed a certain value in order that carbon to adsorb.

Contents

Chapter 1

Introduction

Graphene, a single layer of carbon atoms packed in a honeycomb lattice, is considered by the scientific community the wonder material of the 21^{th} century. The first discussion of the unique properties of graphene dates back to more than 60 years ago when Wallace came with the first theoretical studies on a single sheet of sp^2 hybridized carbon [1]. Later, in 1962 Boehm *et al.* made the synthesis of single and multilayer graphene from the reduction of graphene oxide [2]. However the scientific community did not show particular interest till the beginning of the new century because the material, in its free standing configurations, was predicted to be thermodynamically unstable [3, 4].

Mono- and multi-layer graphene on transition metal surfaces were prepared for the first time by surface scientists in vacuum, either by segregation of the carbon containing materials or by exposure of hot samples to hydrocarbons. In 1968, a single layer of carbon atoms obtained by hydrocarbon dissociation experiments on Pt (001), was observed by means of low energy electron diffraction (LEED) [5, 6]. Later, most of the interest in carbon-based materials was instead focused on fullerenes discovered by Kroto *et al.* [7] in 1985, and then on carbon nanotubes, firstly identified by Iijima [8] in 1991 (Figure 1.1).

Renewed interest on graphene emerged only in the last decade when Geim and Novoselov succeeded in the isolation of a single layer of graphene in 2004 [9], which brought them the Nobel Prize award for the discovery of many exotic properties of this material. In fact, graphene is strictly two dimensional, is very stable under ambient conditions and has a high crystallographic quality. Moreover, the charge carrier mobility of graphene is very high, making it a better conductor than copper at room temperature. It shows excellent thermal conductivity, high thermal stability [10] and outstanding mechanical properties [11]. From the electronic point of view, its charge carriers exhibit a giant intrinsec mobility with a zero effective mass and at room temperature they can travel on average a few micrometers without scattering [12].

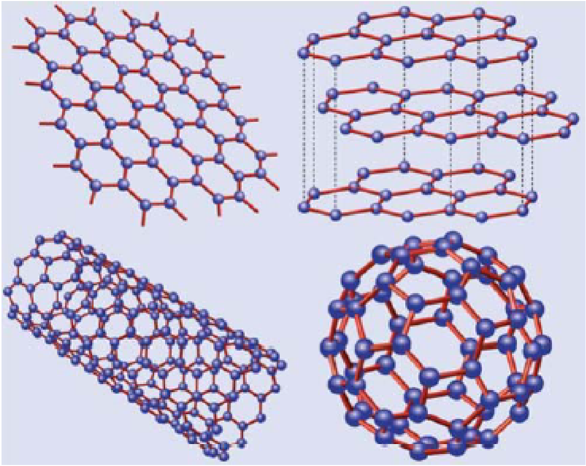

Figure 1.1: *Graphene (top left). Graphite (top right). Carbon nanotubes (bottom left). Fullerenes (bottom right).*

The honeycomb structure of graphene shown in Figure 1.2 consists in two triangular sublattices, or in a unit cell with two non-equivalent atoms (A and B). The lattice vectors can be described as:

$$\mathbf{a_1} = \frac{a}{2}(1, \sqrt{3}), \mathbf{a_2} = \frac{a}{2}(1, -\sqrt{3}) \tag{1.1}$$

where $a = 2.46$ Å is the lattice constant in the plane.

The velocity of delocalized electrons in graphene is constant and independent of momentum, which lead to the conclusion that the charge carriers (electrons and holes) can be described by the Dirac equation for the massless particles with an effective speed of light $v_F \approx 10^6 m/s$. The relativistic character of charge carriers results in some interesting phenomena such as ambipolar electric field effect [13] or an unusual behaviour of the quantum Hall effect [14].

The band structure of graphene presented in Figure 1.3 is different from a metal and is also different from the semiconductor band structure because there is no energy gap. For this reason, graphene can be considered a zero band-gap material.

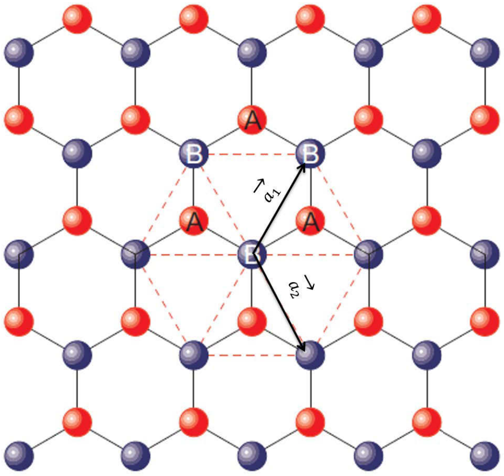

Figure 1.2: *Graphene lattice representation. The two inequivalent atoms of the unit cell, A and B, are highlighted with different colors.*

Actually, the band structure of graphene is positioned somewhere around this two extremes, which make graphene to act like a semimetal. In a closer look at Figure 1.3 it can be observed that the valence and conduction bands meet at the Fermi energy, forming conical bands, which touch at the K and $K^{'}$ high-symmetry points in the Brillouin zone. The extraordinary properties of graphene make it an interesting material for a number of potential applications including spintronic devices [16], fuel cells [17], touch-screens ultracapacitors [18, 19], gas sensors [20], transparent electrodes [21, 22], flexible electronics [23] and high-frequency transistors [24, 25].

One of the main issues for graphene based technology is the synthesis of high-quality monolayers at a large scale. The original method of mechanical exfoliation is not suitable for technological applications due to limitations in the quality and in the large costs of production. The Chemical Vapour Deposition method (CVD) of carbon-containing molecules [26, 27] (*i.e.* hydrocarbons) represents a reliable method for large-scale epitaxial growth of high-quality graphene layers on transition metals. At present, free standing graphene flakes are industrially achieved by high temperature CVD growth on copper foils [28], followed by chemical etching of the metal substrate. Subsequently, graphene is transferred on the substrate of choice, which is usually an insulator. This is because the direct growth of graphene on an insulator using CVD is precluded.

The absence of an electronic band gap in graphene limits its applicability in transistors technology where a band gap is needed for on-off switching operations.

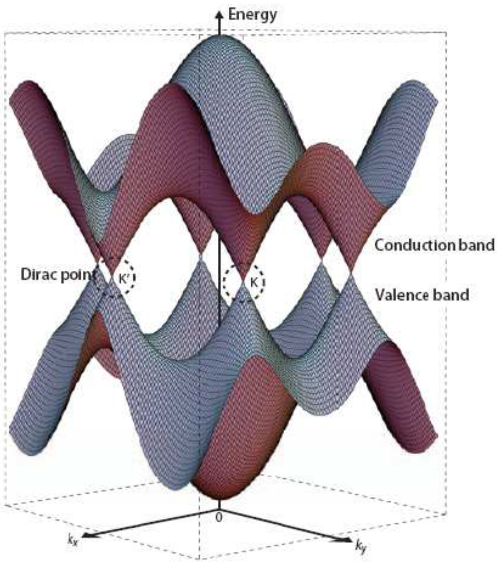

Figure 1.3: *Graphene energy bands close to the Fermi level. The conduction and valence bands touch at K and K′ points. Adapted from [15].*

To overcome this problem, one solution comes from the interaction between epitaxial graphene and transition metal (TM) substrates, which frequently results in the opening of an energy gap at the Fermi level [26, 27]. However, the value of this gap is hardly controllable and evolves as soon as the interaction with the substrate changes. Another solution arises from the possibility to grow a second layer of graphene on the TM substrate, which creates a stable band gap [29]. Unfortunately, the CVD graphene growth on metals is a self-limiting process which stops at monolayer completion [30].

A different approach is therefore needed for the growth of high-quality single- and multi-layer graphene on a large scale which overcomes the aforementioned limitations. The strategy adopted in this PhD research activity is based on Molecular Beam Epitaxy (MBE) and involves the use of a solid carbon source, able to deliver elemental carbon species directly on the substrate of choice.

In order to do this, a solid carbon source has been designed and constructed. The first part of this PhD thesis is dedicated to the investigation of the growth mechanism of graphene on Ir(111), with the aim of comparing the growth process and the quality of the graphene layer obtained by using the carbon source and those obtained by using the standard CVD method. Different strategies were adopted:

- Graphene growth using the carbon source and the Temperature Programmed

Growth (TPG) method (deposition at liquid nitrogen or room temperature and then annealing of the substrate to high temperature);

- Graphene growth using the solid carbon source while keeping the substrate at high temperature (HTG).

Photoemission spectroscopy was used to investigate the presence of the carbon species on the Ir(111) surface. The assignment of the multiple components observed in the photoemission spectra was achieved by comparison with theoretical results obtained by the collaborating group of theoretician at King's College London, led by Prof. Lev Kantorovich. With this approach it was possible to reconstruct the incipient stage of graphene growth on Ir(111), dominated by the diffusion of monomers on the surface. We also demonstrate that a second layer of graphene can be achieved using the solid carbon source.

The second part of the research activity of the present project was dedicated to the growth of graphene on substrates where the dissociation of the hydrocarbon molecules used in CVD is precluded, like noble metals or oxides. New architectures based on graphene interface could pave the way for the manipulation of extreme light concentration, highly efficient photoconversion [31, 32] or printed electronics [33, 34]. However, the preparation of these interfaces is achieved after a complex material processing which leads to a high concentration of contaminants and defects in graphene that compromise its extraordinary properties [35, 36]. The direct growth of graphene on the substrate of choice would overcome all these issues and enable the fabrication of clean, well defined interfaces. To this purpose, we studied the growth of graphene on a pristine Ag(111) by means of MBE. Different experiments were performed in order to find the best substrate temperature during carbon deposition for the graphene growth. Good results were obtained by using the HTG growth method by dosing carbon on the sample at 970-1020 K, while with TPG graphene did not form. The Photoelectron Spectroscopy experiments were complemented with Low Energy Electron Diffraction (LEED) and Near Edge X-ray Absorption Spectroscopy (NEXAFS) measurements, which confirmed the formation of graphene flakes on the surface.

The last part of this research activity was dedicated to the study of graphene-ferroelectric oxides interfaces. Associating graphene with ferroelectrics for the exploration of novel catalytic properties is a completely new research area. The basics of the phenomenon consist in the observation that an electric field, such as the one produced by a ferroelectric surface with out-of-plane polarization may induce a considerable change in the density of states in the graphene layer, promoting high electrons or holes mobility which may activate surface reactions. Interesting side effects may appear in stabilizing spin or charge density on the graphene layer, and sometimes the dispersion law can be significantly changed by such interactions [37]. The main bottleneck for this part of the project is related to the modality to grow graphene onto ferroelectric surfaces. This was achieved by depositing elemental carbon atoms directly on the surface using the solid carbon source.

Bibliography

[1] P.R. Wallace, Phys. Review. **71**, 622-634 (1947).

[2] H.P. Boehm, A. Clauss, G.O. Fischer and U. Hoffmann, *Dűnnste Kohlenstoff-Folien*, Z. Naturforsh. B**17**, 150-153 (1962).

[3] L.D. Landau, *Theory of phase transformations*, Phys. Z. Sowjetunion **11**, 26 (1937).

[4] N.D. Mermin, *Crystalline Order in Two Dimensions*, Phys. Rev. **176**, 405-425 (1968).

[5] A.E. Morgan, G.A. Somorjay, *LEED studies of Gas Adsorption on the Platinum(100)*, Surf. Sci. **12**, 405-425 (1968).

[6] W. May, *Platinum surface LEED rings*, Surf. Sci. **17**, 267-270 (1969).

[7] H.W. Kroto, J.R. Heath, S.C. O 'Brien, R.F. Curl, R.E. Smalley, *C_{60}: Buckminsterfullerene*, Nature **318**, 162-163 (1985).

[8] S. Iijima, *Helical microtubules of graphitic carbon*, Nature **354**, 56-58 (1991).

[9] K.S. Novoselov, A.K. Geim, S.V. Morozov, D. Jiang, Y. Zhang, S.V. Dubonos, I.V. Grigorieva, and A.A. Firsov, *Electric Field Effect in Atomically Thin Carbon Films*, Science **306**, 666-669 (2004).

[10] A.A. Balandin, S. Ghosh, W. Bao, I. Calizo, D. Teweldebrhan, F. Miao, and C.N. Lau *Superior thermal conductivity of single-layer graphene*, Nano Lett. **8**, 902-907 (2008).

[11] C. Lee, X. Wei, J.W. Kysar, and J. Hone, *Measurment of the elastic properties and intrinsec strength of monolayer graphene*, Science **321**, 385-388 (2008).

[12] A.K. Geim, *Graphene:Status and Prospects*, Science **324**, 1530-1534 (2009).

[13] A.K. Geim and K.S. Novoselov, *The rise of graphene*, Nat. Mater. **6**, 183-191 (2007).

[14] K.S. Novoselov, D. Jiang, F. Schedin, T.J. Booth, V.V. Khotkevich, S.V. Morozov, A.K. Geim, *Two-dimensional atomic crystals*, Proc. Natl. Acad. Sci. USA. **102**, 10451-10453 (2005).

[15] T. Ando, *The Electronic properties of graphene and carbon nanotubes*, Nature **1**, 17-21 (2009).

[16] W. Han, R.K. Kawakami, M. Gmitra and J. Fabian, *Graphene Spintronics*, Nat. Nanotech. **9**, 794-807 (2014).

[17] L. Qu, Y. Liu, J.B. Baek, and L. Dai, *Nitrogen-doped graphene as efficient metal-free electrocatalyst for oxygen reduction in fuel cells*, ACS Nano **4**, 1321-1326 (2010).

[18] M. Zhi, C. Xiang, J. Li, M. Li, and N. Wu, *Nanostructured carbon-metal oxide composite electrodes for supercapacitors:a review*, Nanoscale **5**, 72-88 (2013).

[19] J.J. Yoo, K. Balakrishnan, J. Huang, V. Meunier, B.G. Sumpter, A. Srivastava, M. Conway, A.L. Mohana Reddy, J. Yu, R. Vajtai, and M.A. Pulickel, *Ultrathin planar graphene supercapacitors*, Nano Lett. **11**, 1423-1427 (2011).

[20] F. Schedin, A.K. Geim, S.V. Morozov, E.W. Hill, P. Blake, M.I. Katsnelson, and K.S. Novoselov, *Detection of individual gas molecules adsorbed on graphene*, Nat. Mater. **6**, 652-655 (2007).

[21] X. Li, Y. Zhu, W. Cai, M. Borysiak, B. Han, D.Chen, R.D. Piner, L. Colombo, and R.S. Ruoff, *Transfer of large-area graphene films for high-performance transparent conductive electrodes*, Nano Lett. **9**, 4359-63 (2009) .

[22] S. Bae, H. Kim, Y. Lee, X. Hu, J.S. Park, Y. Zheng, J. Balakrishnan, T.Lei, H.R. Kim, Y.II. Song, Y.J. Kim, K.S. Kim, B. Ozylmaz, J.H. Ahn, B.H. Hong, and S. Iijima, *Roll-to-roll production of 30-inch graphene films for transparent electrodes*, Nat. Nanotech. **5**, 574-578 (2010).

[23] K.S. Kim, Y. Zhao, H. Jang, S.Y. Lee, J.M. Kim, K.S.Kim, J.H. Ahn, Ph. Kim, J.Y. Choi, and B.H. Hong, *Large-scale pattern growth of graphene film for stretchable transparent electrodes*, Nature **457**, 706-710 (2009).

[24] F. Schwierz, *Graphene transistors*, Nat. Nanotech. **5**, 487-496 (2010).

[25] Y. Wu, Y.M. Lin, A.A. Bol, K.A. Jenkins, F. Xia, D.B. Farmer, Y. Zhu, and Ph. Avouris *High-frequency scaled graphene transistors on diamond-like carbon*, Nature **472**, 74-78 (2011).

[26] M. Batzill, *The surface science of graphene: Metal interfaces, CVD synthesis, nanoribbons, chemical modifications and defects*, Surf. Sci. Rep. **67**, 83-115 (2012).

[27] J. Wintterlin and M.L. Bocquet, *Graphene on metal surfaces*, Surf. Sci. **603**, 1841-1852 (2009).

[28] X.Li, W. Cai, J. An, S. Kim, J. Nah, D. Yang, R. Piner, A. Velamakanni, I. Jung, E. Tutuc, S.K. Banerjee, L. Colombo, and R.S. Ruoff, *Large-area synthesis of high-quality and uniform graphene films on copper foils*, Science **324**, 1312-1314 (2009).

[29] O. Taisuke, A. Bostwick, T. Seyller, K. Horn, and E. Rotenberg, *Controlling the Electronic Structure of Bilayer Graphene*, Science **313**, 951-954, (2006).

[30] E. Loginova, N.C. Bartelt, P.J. Feibelman, K.F. McCarty, *Factors influencing Graphene growth on Metal surfaces*, New J. Phys. **11**, 063046 (2009).

[31] A.N. Grigorenko, N. Polini, and K.S. Novoselov, *Graphene plasmonics*, Nat. Photonics **6**, 749-758 (2012).

[32] Y. Liu, R. Cheng, L. Liao, H. Zhou, J. Bai, G. Liu, L. Liu, Y. Huang, and X. Duan, *Plasmon resonance enhanced multicolour photodetection by graphene*, Nat. Commun. **2**, 579 (2011).

[33] Q. Cao, H. Kim, N. Pimparkar, J.P. Kulkarni, C. Wang, M. Shim, K. Roy, M.A. Alam, and J.A. Rogers, *Medium-scale carbon nanotube thin-film integrated circuits on flexible plastic substrates* , Nature **454**, 459-500 (2008).

[34] N.O. Weiss, H. Zhou, L. Liao, Y. Liu, S. Jiang, Y. Huang, X. Duan, *Graphene: an emerging electronic material*, Adv. Mater. **24**, 5782-5825 (2012).

[35] Y.C. Lin, C.C. Lu, C.H. Yeh, C. Jin, K. Suenaga, and P.W. Chiu, *Graphene annealing: how clean can it be?*, Nano Lett. **12**, 414-419 (2012).

[36] X. Liang, B.A. Sperling, I. Calizo, G. Cheng, C.A. Hacker, Q. Zhang, Y. Obeng, K. Yan, H. Peng, Q. Li, X. Zhu, H. Yuan, A.R. Hight Walkert, Z. Liu, L. Peng, and C.A. Richter, *Toward clean and crackless transfer of graphene* , ACS Nano **5**, 9144-9153 (2011).

[37] H.B. Wang, T. Mayalagan, X. Wang *Review on Recent Progress in Nitrogen-Doped Graphene: Synthesis, Characterization, and Its Potential Applications* , ACS Catal. **2**, 781-794 (2012).

Chapter 2

Experimental techniques and Setup

In this chapter are presented the experimental techniques used in this research project, together with a brief description of the experimental facilities and the instrumentation used to acquire the data. All the experiments were performed in Ultra High Vacuum Conditions (UHV)(pressure of the order of $10^{-10} - 10^{-11}$ mbar), in the experimental chambers of the SuperESCA beamline of Elettra, the italian synchrotron radiation facility and in the Surface Science Laboratory of Elettra Sincrotrone Trieste. The UHV conditions are needed to reduce the surface contamination rate and are adopted to minimize scattering effects between the low energy electrons (50-300 eV) used in electron based techniques and the residual gas molecules. Indeed, according to the Hertz-Knudsen equation [1], if the sticking coefficient is close to 1 and the background pressure 10^{-6} mbar, the surface will be fully covered by contaminants in a few seconds. Only by lowering the pressure to 10^{-10} mbar, the contamination time will be increased to a few hours, thus allowing to conduct surface science experiments on a well defined and clean system. These vacuum conditions are obtained by using a pumping system, but a complementary bake-out procedure of the vacuum chamber is also needed to reach the 10^{-10} mbar range because of the desorption of water molecules from the inner walls of the chamber. Before each experiment, the samples were cleaned using the proper cleaning procedure. For metallic surfaces, this generally consists in Ar^{+} sputtering cycles, followed by annealing to high temperature to reorder the surface and, in some cases, oxygen treatments to remove residual carbon. In the case of the ferroelectric samples, we developed a cleaning procedure consisting in prolonged annealing of the sample introduced in UHV, at high temperature (up to 820 K) in oxygen atmosphere.

The characterization of the samples was performed using a variety of experimental techniques, namely synchrotron radiation X-ray Photoelectron Spectroscopy (XPS), Near Edge X-ray Absorption Fine Structure (NEXAFS) and Low Energy Electron Diffraction (LEED). For the sample synthesis, Molecular Beam Epitaxy technique was used for the graphene growth on different substrates, while Pulsed Laser Deposition (PLD) was used for the fabrication of the oxide-ferroelectric substrates. In addition, some of the experiments were paralleled by complementary theoretical calculations, based on Density Functional Theory (DFT).

2.1 Molecular Beam Epitaxy (MBE)

The carbon Molecular Beam Epitaxy (MBE) method has shown its advantages in controlling the growth of graphene mono or bi-layers on different substrates [2, 3], in addition to the CVD method used on transition metals [3, 4, 5]. One of the main advantages of this method is that carbon is directly deposited on the substrate of interest, eliminating in this way the transfer process of graphene from the metal it is grown on by CVD to the substrate onto which graphene will ultimately be used. However, in order to obtain high quality graphene layers a few parameters, such as substrate temperature, growth time, carbon flux and background pressure, have to be carefully controlled.

MBE is a well known and widely used technique to produce high quality, homogeneous epitaxial layers with reproducible thickness and composition. For all these reasons, the MBE has become an attractive method to synthesize also graphene films. This technique, which was developed for the first time in 1970 at the Bell Laboratories in USA [6] is illustrated in Fig. 2.1. The left panel is intended to be a definition of epitaxy, i.e. the commensurate growth of a single crystal layer onto a single crystal substrate. The right panel evidences the three main growth mechanisms, starting with the two extreme cases layer-by-layer and 3D clustering, with the intermediate and more frequent behaviour (Stransky-Krastanov growth).

The conditions for applying molecular beams are satisfied when the mean free path λ of the atoms is larger than the geometrical size of the chamber. This is easily fulfilled if the total pressure does not exceed 10^{-5} mbar. Therefore, the MBE growth method shows good results if the UHV level is in the range of 10^{-10} mbar. Any increase of this barrier induces contamination rates of the substrate comparable with the growth rate of the target material. In carbon MBE, the Knudsen cell tipically used in a conventional molecular beam epitaxy technique is replaced by a custom made evaporator in which a hot graphite rod is used as a direct source for the carbon atoms in the epitaxial growth. The description of the evaporator and the best working conditions are discussed in the next section.

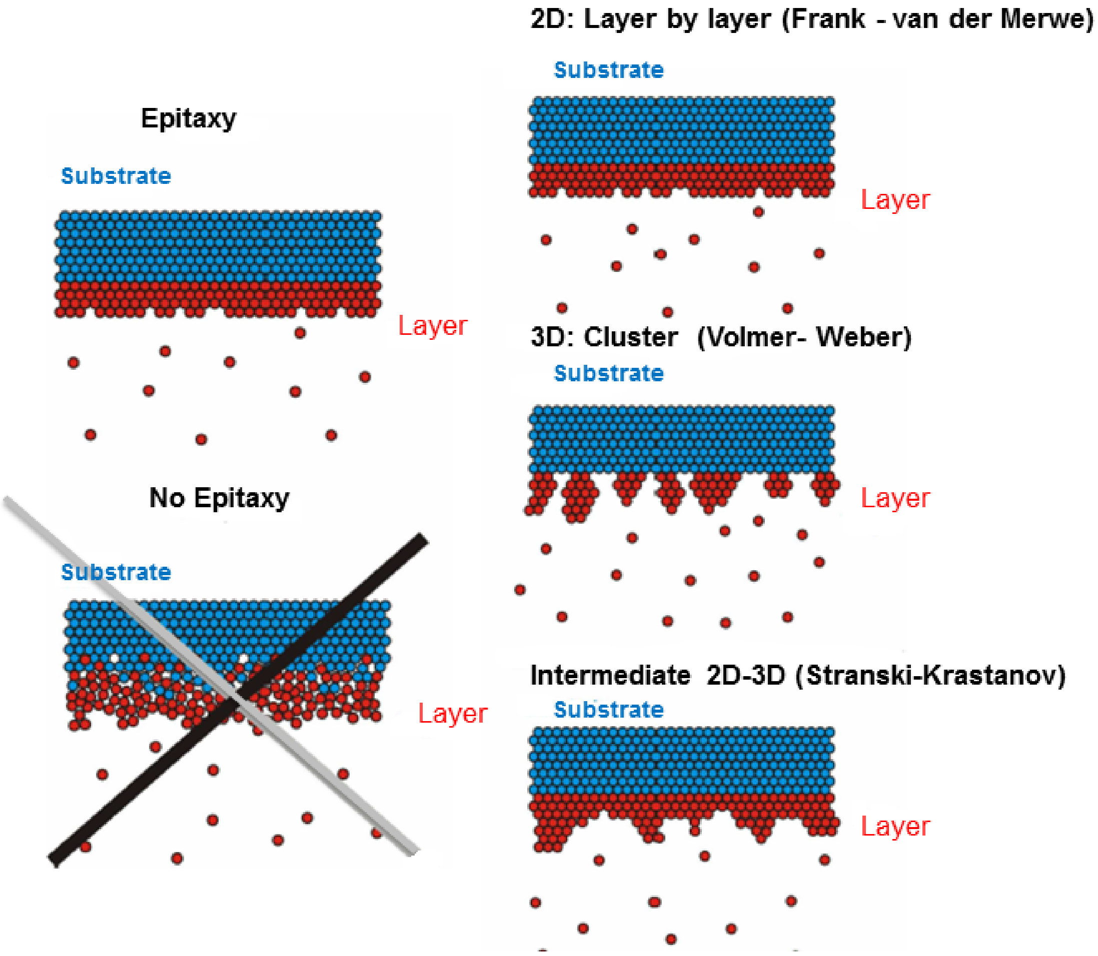

Figure 2.1: *Different growth mechanisms on a single crystal surfaces. Adapted from [7].*

2.2 The solid carbon source evaporator

The carbon evaporator is based on the electron bombardment principle, that allows to increase the temperature of a graphite rod tip to more than 2000 °C, which is needed for carbon sublimation [8]. It is composed by a tip-shaped graphite rod connected to the high voltage, which is heated by the accelerated electrons emitted by W filaments placed close to the target tip. The evaporator is equipped also with a wehnelt, represented by the small ring around the graphite rod (see Fig. 2.2 (b)) which is connected to a negative voltage for focusing the electrons to the carbon tip. In our case, the wehnelt was set to ground.

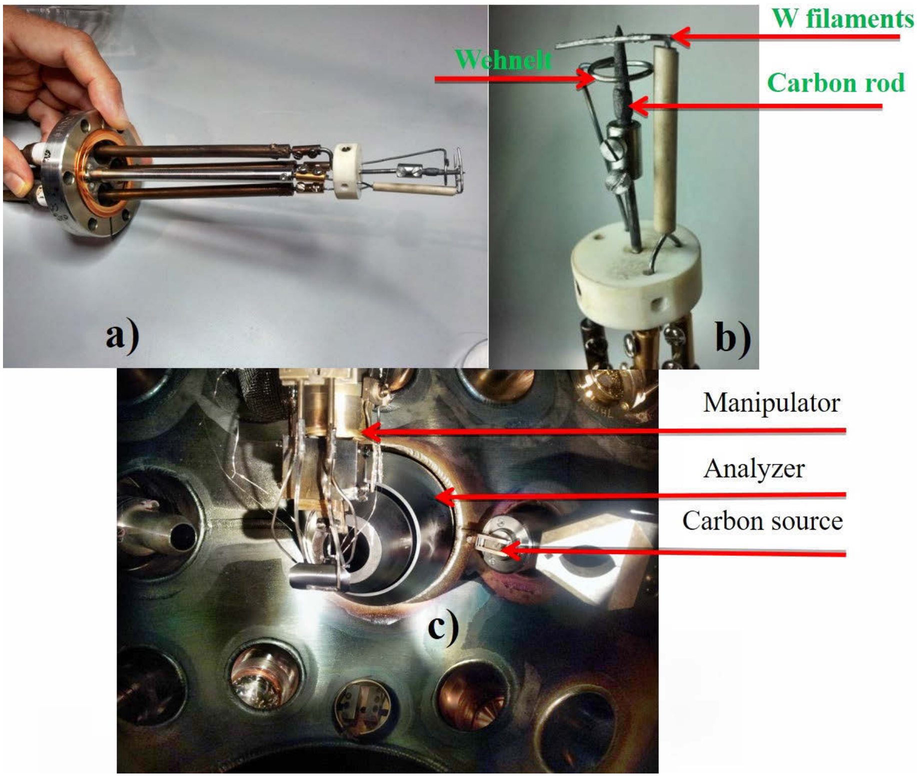

Figure 2.2: *(a) Image of the solid carbon source. (b) Close view of the carbon rod and the W filaments. (c) Configuration of the carbon evaporator for in-situ measurements at the SuperESCA beamline.*

In the preliminary characterization, the working conditions of the carbon source were defined, namely the high voltage to apply to the tip and the current of the W filaments, in order to achieve the proper electron emission current for tuning the carbon flux. The best working conditions were found with a voltage of 1 kV applied to the graphite rod and a current of 5 A in the W filaments, which implies an electron emission current of $\sim$ 150 mA and a carbon deposition rate of $\sim 1.8x10^{-3}$ ML per seconds at the distance of 80 mm, where the sample was placed. A water cooling system was added in order to reduce the contamination in the UHV chamber, due to the excessive heating of the evaporator surroundings. The evaporator was placed on the side of the electron energy analyzer, as shown in Fig. 2.2 (c). This allowed us to make real-time XPS measurements during carbon deposition, maintaining the background pressure in the 10^{-10} mbar range, thus reducing the adsorption of unwanted species on the sample surface.

2.3 Pulse Laser Deposition (PLD)

Among the several applications of lasers, one is for physical vapour deposition where a high-power pulsed and collimated laser beam is used in vacuum to hit a target of the material that has to be deposited [9]. The main advantages of this deposition method, that differentiate it from others such as vacuum thermal evaporation, arc evaporation, chemical vapour deposition, etc., are related to the possibility of producing layers of complex materials (oxides, nitrides) with the same stoichiometry of the target. The use of laser pulses also benefits from the possibility to control a variety of parameters: (i) laser radiation fluency, (ii) wavelength of the radiation (which typically is chosen in the range where the target presents minimal reflectivity), (iii) frequency and duration of pulses, which models the length and geometry of the plasma that forms on the surface of the target. It is worth mentioning here that the characteristics of the plasma are determined by the environmental gas pressure during deposition. In addition the gas may contain a well-defined oxygen or nitrogen concentration, to adjust the stoichiometry of the deposited layers (to avoid the production of coatings deficient in oxygen or nitrogen). Finally the substrate temperature is defining the crystallinity of the deposited layers.

The ferroelectric samples investigated in this work, were prepared in the PLD set-up, shown in Fig. 2.3 and Fig. 2.4, by the group led by Dr. Lucian Pintilie from the National Institute of Material Physics (NIMP), in Magurele, Romania. The set-up consists of:

- target holders (several, to deposit multilayer composites and coatings);
- sample holder, with heating system (up to 1000 °C);

- vacuum chamber ($10^{-5} - 10^{-9}$ mbar);
- excimer laser KrF, $\lambda = 248$ nm;
- optical components for focusing and guiding the laser beam;
- *in situ* quality check of deposited layers (Reflection High Energy Electron Diffraction (RHEED)).

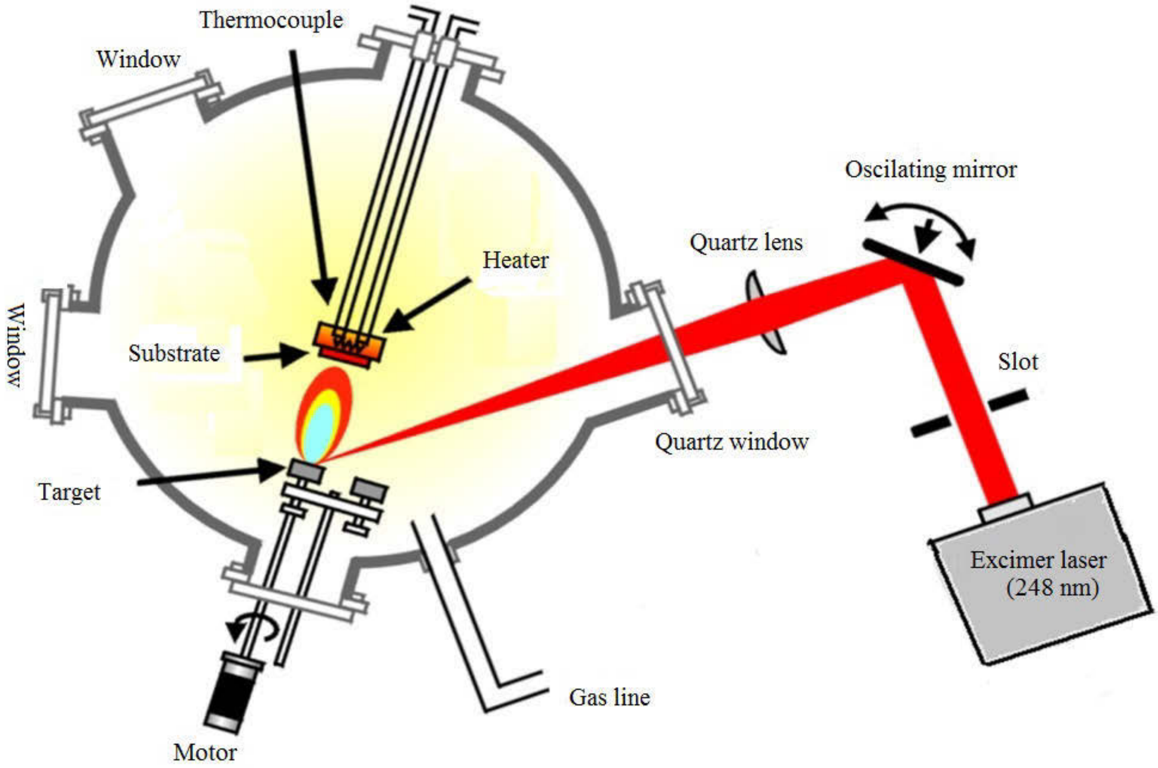

Figure 2.3: *Sketch of the PLD facility. Adapted from [7].*

Figure 2.4: *The PLD experimental set-up used for the growth of PZT thin layers*.

2.4 X-ray Photoelectron Spectroscopy (XPS)

X-ray Photoelectron Spectroscopy is a non-destructive analysis technique that is used to investigate the properties of surfaces, interfaces and thin layers. It is based on the interaction of photons with matter (photoelectric effect). The technique involves placing a sample in UHV, irradiating it with photons produced by a conventional anode based X-ray source or soft X-ray synchrotron radiation and analysing the kinetic energy of the photoemitted electrons.

The photoemission process [10] involves the absorption of a photon with energy $h\nu$ by an atom of the sample, leading to the emission of an electron with initial binding energy E_B, with final kinetic energy in vacuum E_K given by

$$E_K = h\nu - E_B - \Phi \tag{2.1}$$

where Φ is the work function of the system (2-7 eV [11]), i.e. the difference between the vacuum level and the Fermi energy, $\overline{E}_F$.

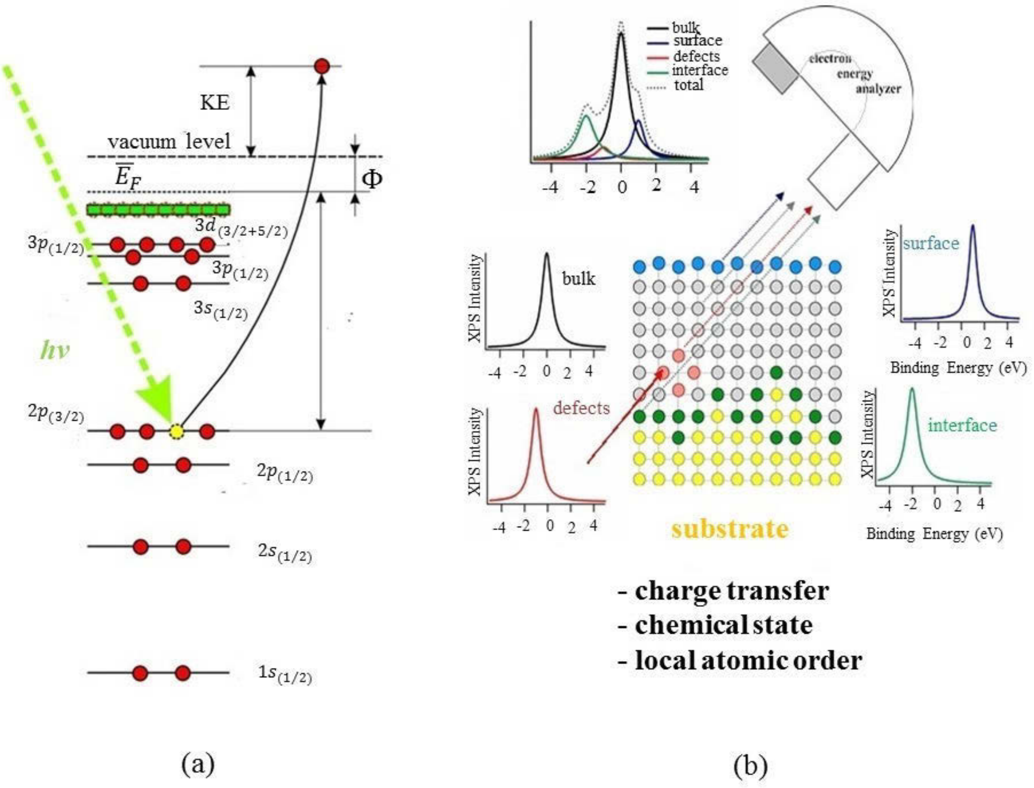

Figure 2.5: *(a) Principle of X-ray Photoelectron Spectroscopy; (b) Origin of XPS components with different binding energies for a thin film deposited on a substrate [12].*

In a photoemission experiment, the initial electron binding energy is calculated from the measured kinetic energy E_K^{meas}. The commonly accepted procedure is to refer the binding energy scale to the position of the Fermi level, which is common to the sample and the electron energy analyzer. The kinetic energy measured by the analyzer, E_K^{meas} is therefore given by

$$E_K^{meas} = h\nu - E_B - \Phi_{sample} + (\Phi_{sample} - \Phi_{analyzer}) = h\nu - E_B - \Phi_{analyzer} \tag{2.2}$$

Φ_{sample} and $\Phi_{analyzer}$ is the work function of the sample and analyzer, respectively.

Since core electrons in each element have a characteristic binding energy, photoemission spectroscopy is the ideal tool for the chemical analysis of materials. The deviation of the BE from the free atom case, because of formation of bonds, is called chemical shift [13]. In most cases, core level shifts (CLS) may be used to assert the nature of the compounds present in the sample. The binding energies depend also on other factors, such as the surface or bulk nature of the emitting atoms, the interaction of the emitting atoms with different species, or the occurence of some defects in the neighborhood of these atoms, as represented in Fig. 2.5(b). Therefore, an XPS spectrum for a given element is often the superposition of several components and the isolation of the components is usually achieved by a computational deconvolution procedure.

Another important property of photoelectron spectroscopy is related to its surface sensitivity. The emitted electrons have kinetic energies ranging typically from tens of eV to 1.5 keV. It is well known that, at these energies, electrons are subjected to inelastic scattering. If I_0 is the photoemission intensity in a solid material at depth d with respect to the surface, the scattering phenomena mentioned above imply that the detected photoemission intensity will be given by the Beer-Lambert law [10]:

$$I(E) = I_0 exp\left[-d/\lambda(E)\right] \tag{2.3}$$

where $\lambda(E)$ is called inelastic mean free path (IMFP) and its dependence on the kinetic energy E is a universal curve (Fig. 2.6) with a minimum of $4 - 5$ Å for kinetic energies of 50-100 eV. In the case of graphite, for example, the IMFP ranges between 4.57 Å and 31.5 Å for electron energy between 50 and 2000 eV as shown in Fig.

2.6. Usually, at the SuperESCA beamline we measure the C 1s core level of graphite ($E_B \sim 285$ eV) with 400 eV photon energy which results in a kinetic energy of ~ 115 eV, corresponding to a IMFP in the range of 4.73 Å - 4.92 Å [14]. Equation 2.3 implies that in the range of kinetic energies tipically used in XPS the electrons are coming from a depth of 1.5-6 nm from the sample surface. This also implies that the sample must present an advanced degree of cleanness of its surface, otherwise the electrons from the sample surface may be strongly attenuated by the contamination layer. For deeper layers investigation XPS may be combined with cycles of ion sputtering to remove the topmost layers from the sample surface. This procedure, however, must be applied with some care since, especially for compound samples such as oxides, preferential sputtering may occur and the first layer composition might be affected by the sputtering process.

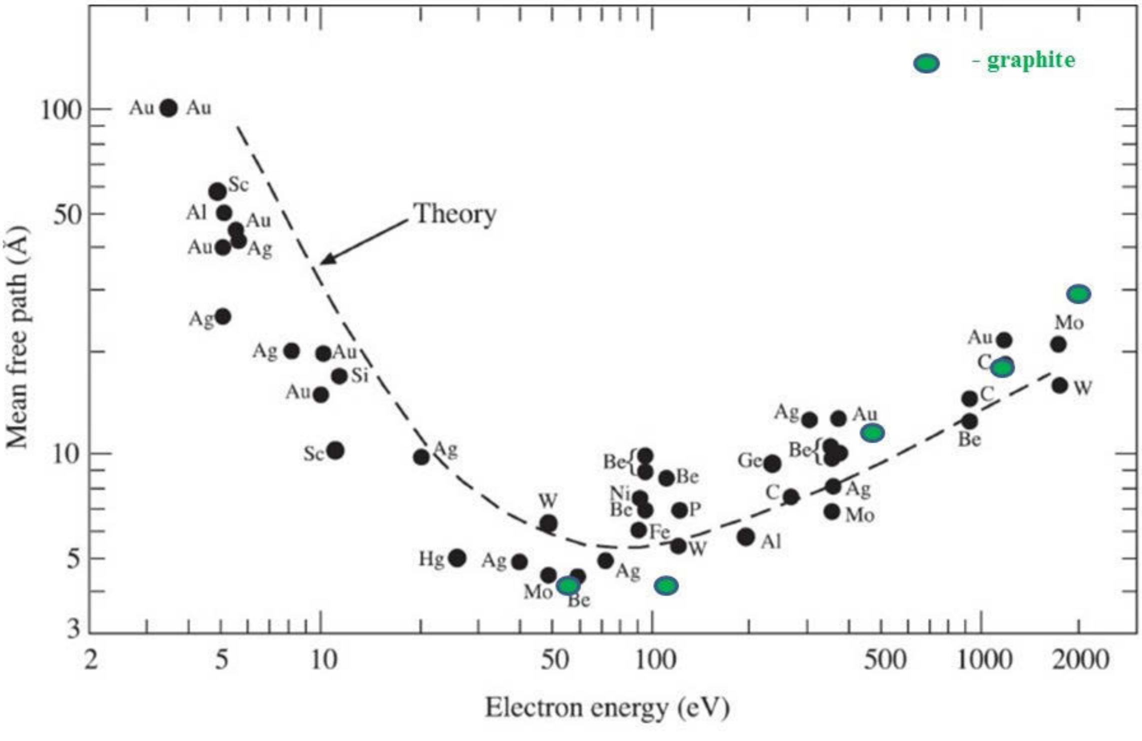

Figure 2.6: *Universal curve of electron inelastic mean free path. Adapted from [15], in which are included the values for graphite from [14].*

The photoemission signal intensity is proportional to the photoemission cross section which is the probability of exciting a system from an initial state to a final state with a flux of 1 photon x cm$^{-2}s^{-1}$ [16]. Figure 2.7 presents the variation of cross section for some of the core levels analyzed in this thesis, namely C 1s, Ir 4f, Ag

3d, Pb 4f and O 1s as a function of the incident photon energy. This figure brings out one of the main advantages of using synchrotron radiation, *i.e.* the photon energy tunability, which offers the possibility to change the sensitivity to a specific core level.

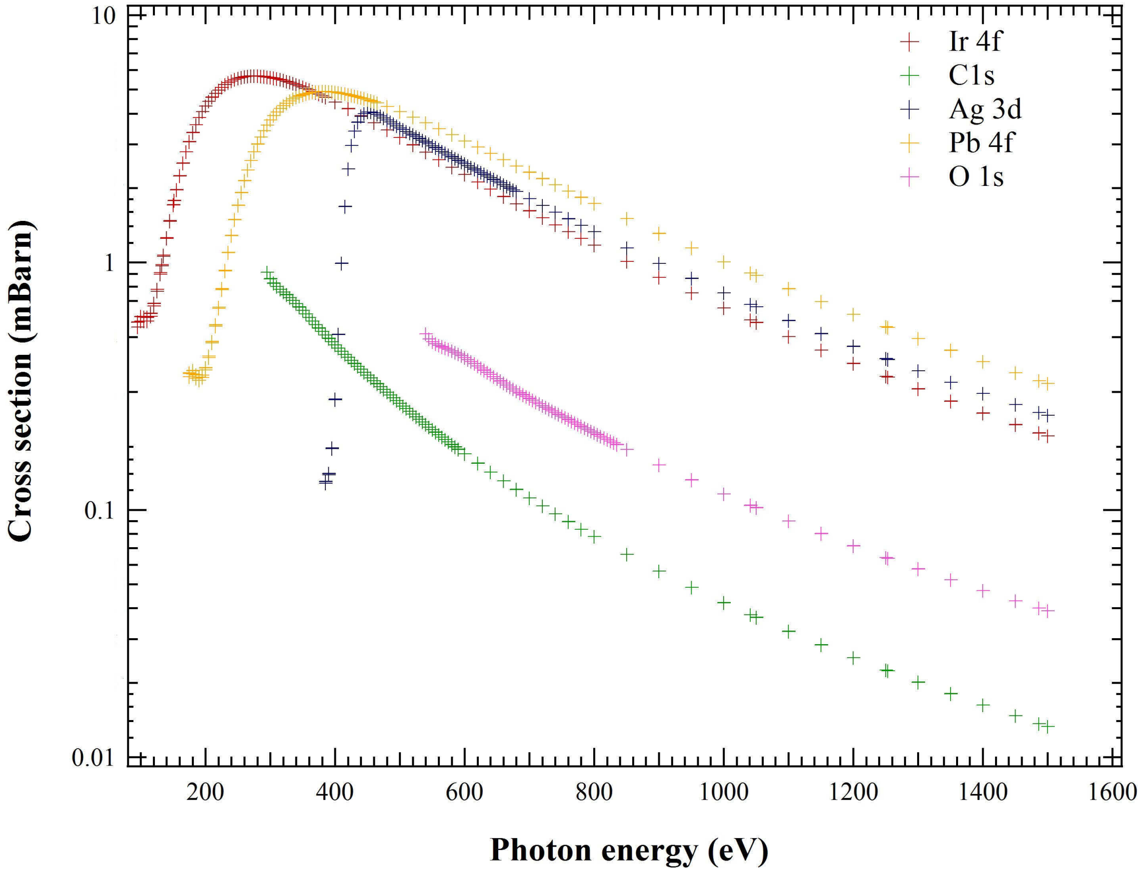

Figure 2.7: *Photoemission cross-section for the Ir 4f, C 1s, Ag 3d, Pb 4f and O 1s core levels as a function of incoming photon energy.*

2.4.1 Analysis of core level spectra

The analysis of core level spectra consists in reproducing the photoemission spectrum with a proper theoretical function, in order to extract quantitative information on the number, position and intensity of the individual components of the spectrum. One of the most frequently used formalisms is the semi-empirical model formulated by Doniach and Šunjić (D-S) [17]. To account for the core hole lifetime of the excited atoms and also to describe the asymmetric tail at lower kinetic energies in the photoemission spectra due to electron-hole pair excitations at the Fermi level, Doniach and Šunjić developed a modified Lorentzian lineshape, in which the asymmetry is introduced through the α parameter:

$$I_{DS}(E) = I_0 \frac{\Gamma_E\,(1-\alpha)}{\left[(E-E_b)^2 + \Gamma^2/4\right]^{(1-\alpha)/2}} \zeta(E) \tag{2.4}$$

where Γ is the Full Width Half Maximum (FWHM), Γ_E is the Euler gamma function and

$$\zeta(E) = cos\left[\frac{\pi\alpha}{2} + (1-\alpha)\, arctan\left(\frac{E-E_0}{\Gamma/2}\right)\right] \tag{2.5}$$

The width of photoemission spectra is also affected by the phonon broadening and by the experimental resolution which is due to the electron energy analyzer and the photon beam. These contributions are described by a Gaussian function:

$$I_G(E) = \frac{I_0}{\sigma\sqrt{2}} \exp\left(-\frac{(E-E_B)^2}{2\sigma^2}\right) \tag{2.6}$$

All XPS spectra presented in this thesis were analyzed using D-S functions convoluted with Gaussians. [18]. The BEs of the different components were always referenced to the Fermi level. The background is considered either Shirley type or linear depending on the specific spectra. The Shirley type background is calculated iteratively as follows [19]:

$$S_i(E) \propto \int_E^\infty dE'(I(E') - S_{i-1}(E')) \tag{2.7}$$

where $S_i(E)$ is the Shirley net intensity at the *i-th* iterations and I(E) is the photoemission intensity of experimental spectra.

2.5 The Near Edge X-ray Absorption Fine Structure Spectroscopy (NEXAFS)

The Near Edge X-ray Absorption Fine Structure Spectroscopy (NEXAFS) is derived from X-ray Absorption Spectroscopy and refers to the absorption fine structure close to an absorption edge, extending from zero to about 30-50 eV above the edge (see Fig. 2.8). This is the energy region showing the largest variations in the x-ray absorption coefficient. The other region, which extends from 50 eV up to a few hundreds of eV beyond the absorption edge is called Extended X-ray Absorption Fine Structure (EXAFS), but will not be the subject of this section.

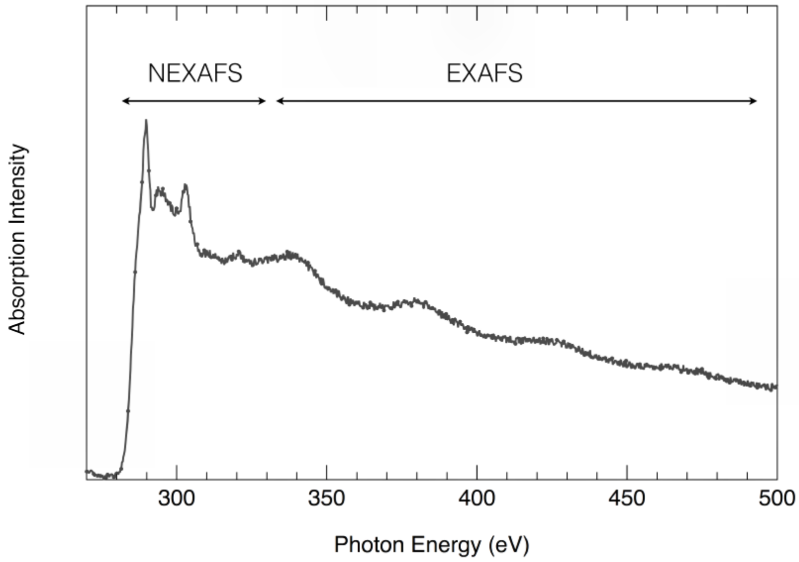

Figure 2.8: *Sketch of a typical absorption spectrum.*

NEXAFS was first devised in 1980s [21], mainly to investigate the structure and the orientation of adsorbed molecules on surfaces, by probing the intermolecular transitions from a deep core shell (i.e. K shell) into unoccupied molecular orbitals close to the vacuum level. The origin of the NEXAFS intermolecular transitions is illustrated in Fig. 2.9, where the case of a diatomic molecule is shown. In this model, the resonant transitions are superimposed in a step like shape around the ionization threshold. These transitions are permitted only if the energy of the incoming photons matches exactly the energy difference between the initial state and an unoccupied (molecular) state with angular momentum quantum number $\ell' = \ell \pm 1$, where ℓ belongs to the initial state wave function. Besides the electronic structure of molecules, NEXAFS can also provide information about their orientation on the surface. To this purpose, the polarization characteristics of synchrotron radiation are exploited. Assuming that the synchrotron radiation is almost linearly polarized in the plane of the storage ring, we can relate, in the dipole approximation, the initial state Ψ_i and the final state Ψ_f, to the absorption cross section σ_x (Fermi's golden Rule):

$$\sigma_x \propto |\varepsilon \cdot \langle \Psi_f | \nabla | \Psi_i \rangle|^2 \rho_f(E) \tag{2.8}$$

where ε is the polarization vector of the incoming radiation and $\rho_f(E)$ is the density of final states. For a 1s initial state and a directional final state orbital (which is of p-type) the matrix element $\langle \Psi_f | \nabla | \Psi_{1s} \rangle$ points in the direction Ω of the final state orbital [22], and the absorption cross section becomes:

$$\sigma \propto |\varepsilon \cdot \langle \Psi_f | \nabla | \Psi_{1s} \rangle|^2 \propto |\varepsilon \cdot \Omega|^2 \propto \cos^2 \alpha \tag{2.9}$$

where α is the angle between ε and Ω.

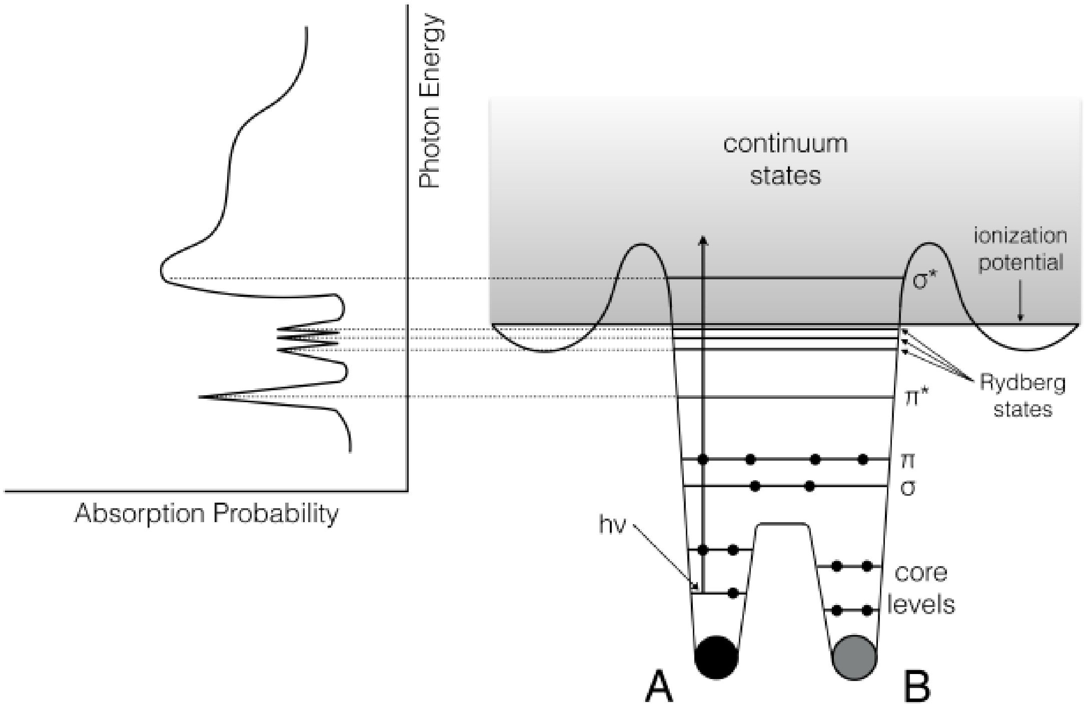

Figure 2.9: *Schematic of the K-edge absorption spectrum (left) and potential (right) for a diatomic (A,B) molecule. Besides the Rydberg states, π^* and σ^* resonances are allowed due the excitation of atomic 1s core electrons to empty molecular orbitals. Adapted from [22].*

In the case of graphene, there are in plane unoccupied σ^* bonds and, perpendicular to them, out of plane π^* bonds. Therefore, from the equation 2.9 it results that the modulation of the σ^* and π^* is opposite. In other words, when the impinging electric field polarization is perpendicular to the graphene plane, only the 1s $\rightarrow \pi^*$ resonance is measured, while, when the electric field polarization is parallel to the plane, only the 1s $\rightarrow \sigma^*$ resonance is at maximum intensity. In Figure 2.10 NEXAFS C K-edge spectra of graphene on Ni(111) are shown as an example to highlight the different behavior modulation of the σ^* and π^* resonances.

In a NEXAFS experiment, the sample is irradiated with monochromatic X-rays with energy close to the ionization edge, resulting in the excitation of a core electron to an empty level, leaving a core hole. The hole is subsequently filled by an electron of an outer level. The energy released in this process can be transferred to another electron which is emitted (Auger process) or it results in the emission of a photon (Fluorescence process). The NEXAFS spectra can be measured in Auger Electron Yield (AEY) or in fluorescence Yield (FY). The FY mode is more bulk sensitive because of the larger penetration depth of photons as compared to electrons, while with AEY the NEXAFS measurements are more surface sensitive. On the other hand, for the elements with low atomic number, such as carbon, the probability of Auger emission is much higher than that of fluorescence emission [23, 24]. In this work, the NEXAFS spectra are measured always in the AEY mode.

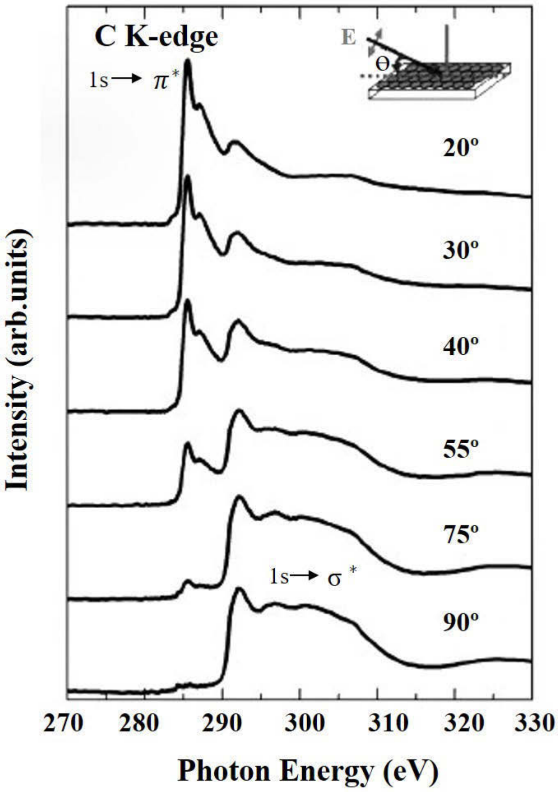

Figure 2.10: *A series of NEXAFS C K-edge spectra of graphene on Ni(111) recorded at different incident angles. Adapted from [20].*

2.6 Low Energy Electron Diffraction (LEED)

LEED is a widely used method to characterize the surface structure of crystalline materials [25, 26]. Since its discovery in 1927 by Davisson and Germer [27], LEED remains one of the most powerful tools used in the investigation of ordered surfaces due to its wide range of applicability, low cost and quite simple interpretation of the LEED patterns within the kinematic theory. The long-range order of the surface can be investigated through the analysis of the diffraction patterns produced by low energy electrons (20-400 eV). The surface sensitivity is achieved thanks to the inelastic mean free path, that is always less than 10 Å in this energy range.

According to the kinematic theory, we can consider the electron as a plane wave that, interacting with the surface, which can be considered as a two dimensional lattice, diffracted along particular directions that satisfy the Laue condition: $\Delta\mathbf{K}_{||} = \mathbf{G}$, where $\Delta\mathbf{K}_{||} = \mathbf{k}_{i||} - \mathbf{k}_{f||}$ is the scattering vector parallel to the surface and $\mathbf{G}$ is

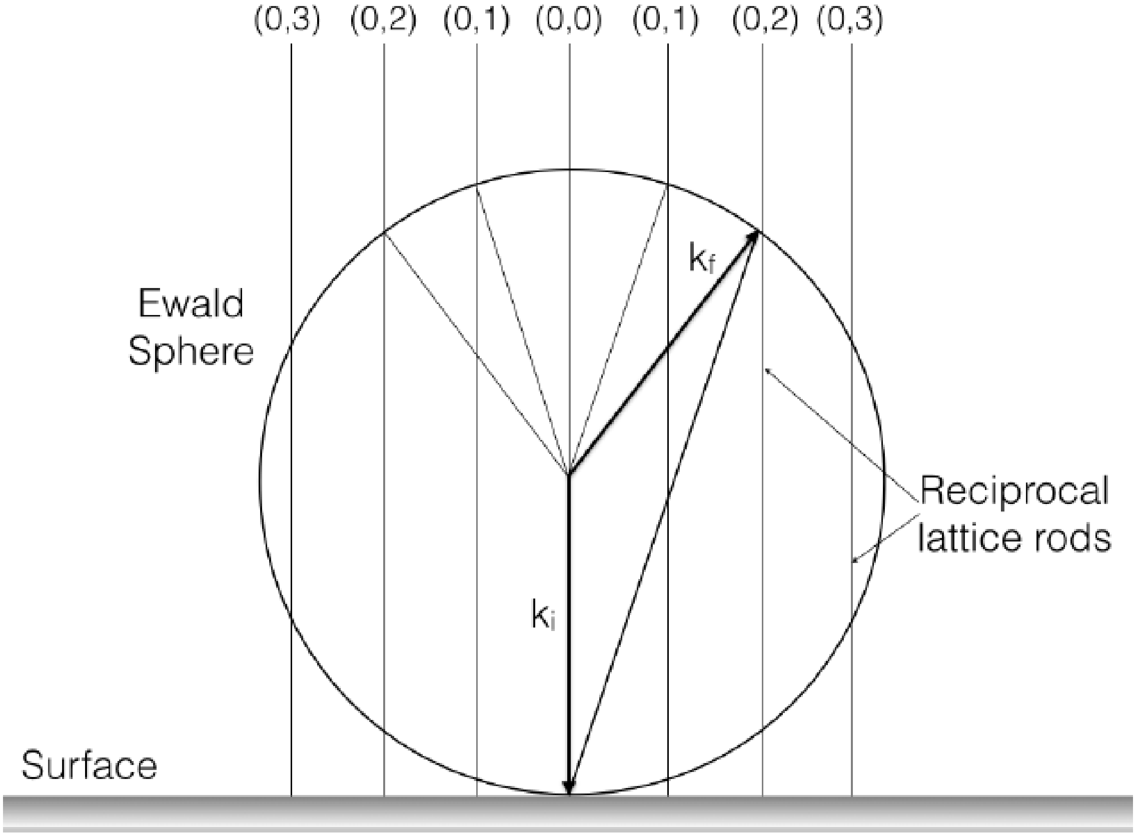

Figure 2.11: *Reciprocal lattice of the Ewald Sphere.* $\vec{k}_i$ *is the incidend electron wave vector, and* $\vec{k}_f$ *is the diffracted one.*

the reciprocal lattice vector of the surface.

The elastic scattering conditions imply that the energy is conserved, *i.e.* $|\mathbf{k}_f| = |\mathbf{k}_i|$. A LEED pattern can be considered as an immediate representation of the reciprocal space (or the 2D *k*-space) of the surface, which can be interpreted through geometric construction of the Ewald sphere (represented in Fig. 2.11). The vertical lines perpendicular to the crystal surface are designed in correspondence to the points of the reciprocal lattice. The directions of the scattered electrons can be therefore determined by intersecting the vertical lines with the Ewald sphere which correspond to the solutions of the Bragg equation that along one direction on the surface can be written as $n\lambda = dsin\theta$ with d the interatomic distance, λ the deBroglie wavelength of the electrons and θ the scattering angle.

A conventional LEED apparatus is presented in Fig. 2.12 (a). A collimated monochromatic electron beam hits the sample with the desired energy. Once the electrons reach the sample, they are backscattered from the surface and then collected.

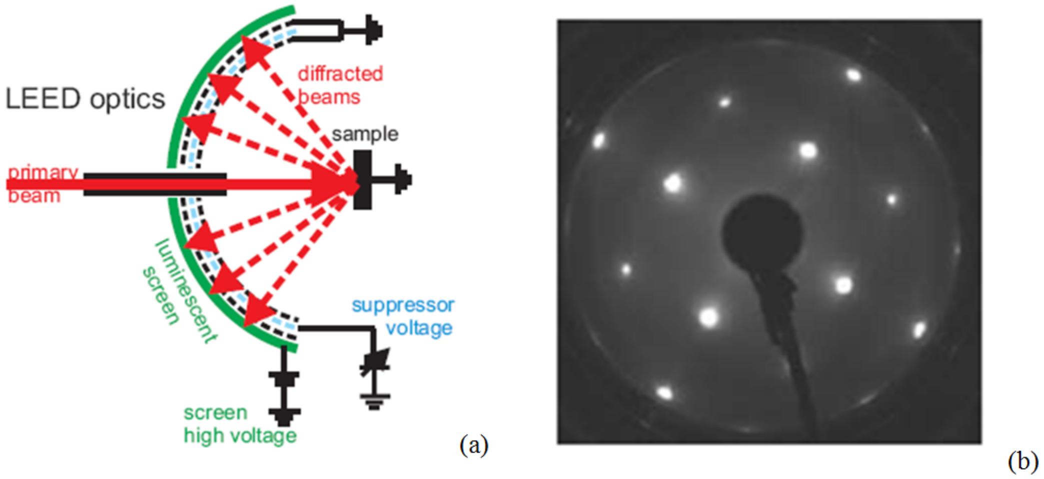

Figure 2.12: *(a) Schematic illustration of the LEED apparatus. (b) Example of a LEED pattern.*

The electrons from inelastic scattering are blocked by the supressor grids and only the elastically scattered electrons are accelerated to a fluorescent screen by a positive potential of a few kV. Then, the LEED patterns collected on the fluorescent screen are typically recorded with a CCD camera (Fig. 2.12 (b)).

2.7 The Elettra synchrotron

The synchrotron facility localized in Trieste (Italy), known also as Elettra, is a third generation storage ring and is operational since 1993. Synchrotron radiation is produced when electrons traveling at relativistic speed are forced by a magnetic field to follow a curved trajectory in the storage ring, thus resulting in a highly collimated photon beam in the tangential direction [28]. At Elettra, the electron bunches are generated by a thermoionic emission from a ceramic disc and first accelerated in a straight line through a linear accelerator (LINAC). Then the electrons are injected into a booster ring where they are accelerated to the operating energy (2 or 2.4 GeV) and finally are transferred in the storage ring. Different type of magnets are used in the ring: the bending magnets (to deflect the electron beam into a circular path), quadrupoles (for beam focusing), sextupoles (for compensating chromatic and non-linear effects) and steer magnets that perform small adjustments to the circular trajectory. The energy lost due to the emission of synchrotron radiation is reintegrated by four radio-frequency cavities. On the straight sections of the ring are usually inserted undulators consisting of two periodic arrays of magnetic poles forcing the circulating electrons to follow a wiggling trajectory, in such a way to irradiate. These devices are the primary sources of high brightness x-ray beams (see fig. 2.13). The strength points of synchrotron radiation are the high brilliance, tunability and the high degree of polarization of the photon beam.

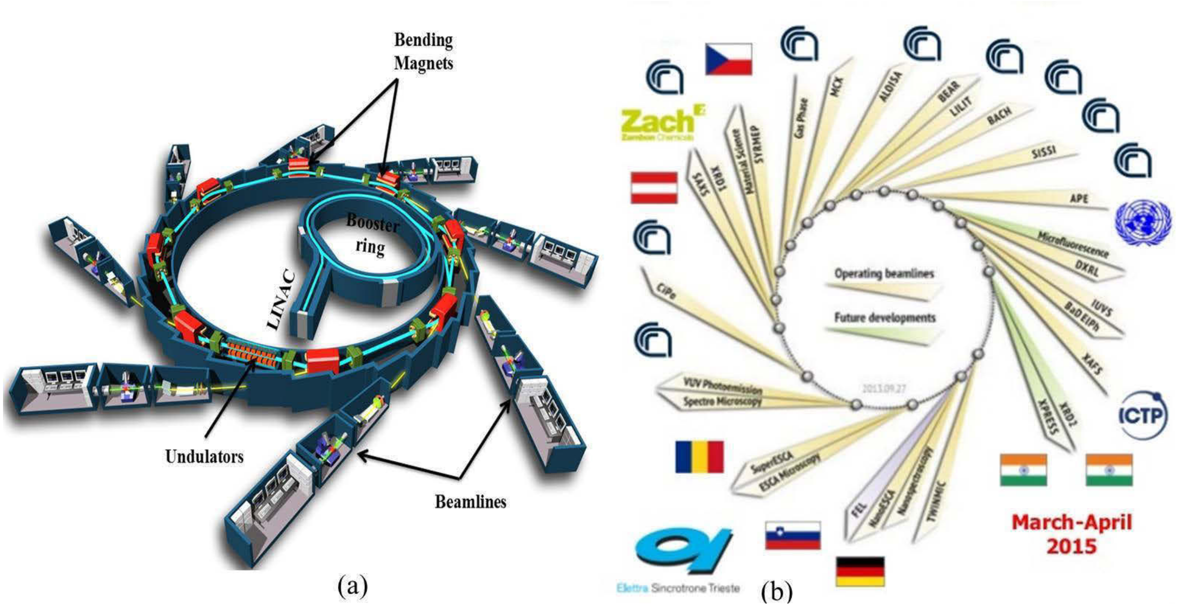

(a) (b)

Figure 2.13: *A sketch of the (a) synchrotron facility and (b) of the beamlines at Elettra Sincrotrone Trieste.*

2.8 The SuperESCA beamline

SuperESCA is the first operational beamline at Elettra (1993) and is optimized for photoelectron spectroscopy with soft X-rays [29]. The radiation source is a two-sections 46 mm-period high brilliance undulator with 98 periods, that produces linearly polarized photons in the energy range 90-1500 eV. The photon beam from the undulator is monochromatized with an SX 700 monochromator and focused by an ellipsoidal mirror into the center of the experimental main chamber. The resolving power of the monochromator ($E/\Delta E$) is in the order of 10^4 at 400 eV, with a photon flux of 10^{12} photons/s.

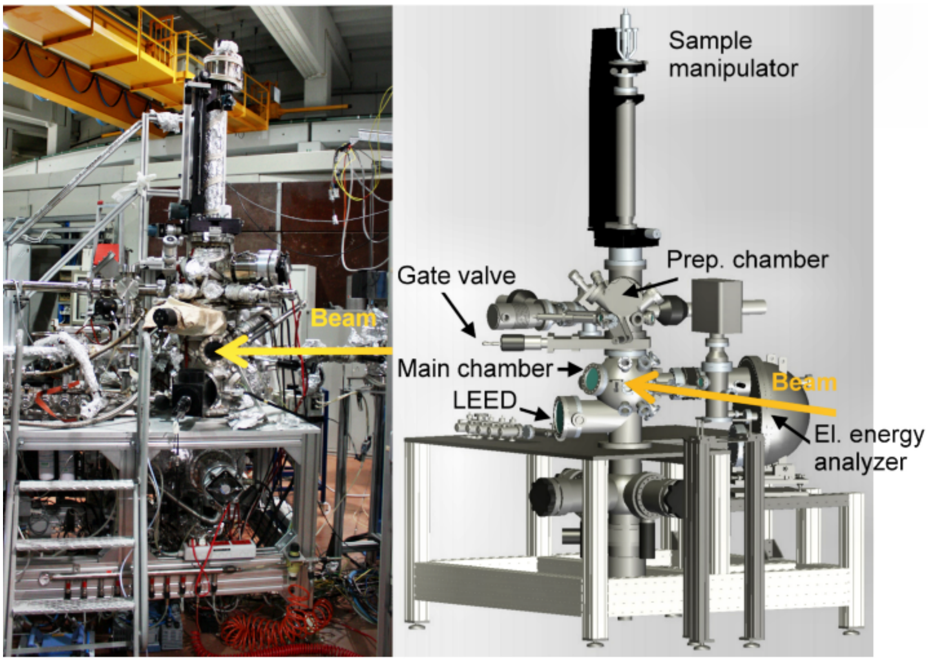

Figure 2.14: *The SuperESCA beamline at Elettra.*

The experimental station represented in Fig. 2.14 consists of two UHV chambers separated by a gate valve. The upper chamber is made of stainless steel and is designed for sample preparation. The bottom chamber is made of μ-metal in order to screen the external magnetic fields and is designed for measurements. Two manipulators can be mounted depending on the experiments to be performed. The first one is a modified version of the CTPO from VG instruments, with 5 degrees of freedom (3 on the x, y, z axes and 2 rotational fully automatized (Θ and Φ). The allowed sample temperature is in the range of 120-1500 K. The second one is a liquid He cryostat with xyz translations and only one rotational axes Θ, allowing to reach a sample temperature in the range 20-2000 K. The chamber is also equipped with a LEED system, a series of evaporators, a quadrupole mass spectrometer and a SPECS Phoibos electron energy analyzer with a mean radius of 150 mm, equipped with a custom made delay line detector [30].

In Fig. 2.15 is sketched the Phoibos hemispherical electron energy analyzer which consists of two concentric hemispheric electrodes of radius R_1 and R_2. The potential difference between the two hemispheres is given by

$$V_2 - V_1 = V_0 \left(\frac{R_2}{R_1} - \frac{R_1}{R_2} \right) \tag{2.10}$$

From this equation we can determine the potentials to be applied to the hemispheres in order to select the electrons with energy $E_0 = |e| V_0$, the so called pass energy. In fact, the electrons which are passing through the hemispherical analyzer are only those with kinetic energy E_0, following a curved trajectory of radius $R_0 = (R_2 + R_1)/2$ to the detector. The device resolution depends on few aspects like geometrical parameters of the analyzer, angular divergence of the electron beam and the selected pass energy:

$$\Delta E = E_0 \left(\frac{\omega}{2R_0} + \frac{\alpha^2}{4} \right) \tag{2.11}$$

where ω is the width of the entrance slit and α is the impinging angle of the electrons at the entrance slit. The luminosity of the analyzer is improved by the electrostatic lenses in front of the hemispheres which are collecting the electrons from a large solid angle, focus them into the entrance slit of the analyzer and slow them down to the selected kinetic energy E_0. A compromise is required between energy resolution and electron transmission in order to obtain a good signal-to-noise ratio. At the SuperESCA experimental chamber, a microchannel plate based detection system is used to measure the electrons reaching the detector of the analyzer. The experimental spectra are usually acquired in *sweep* (or scanning) mode in which the voltages of the two hemispheres V_1 and V_2 are held fixed, thus resulting in a fixed pass energy. At the same time the voltage applied on the electrostatic lenses is modified in such a way that each channel counts electrons with the selected kinetic energy for a given time window. In order to drastically reduce the data aquisition time, the so called *snapshot* (or fixed) mode is often applied. Basically, if the photoemission signal collected by the channel plate detector is sufficiently strong and also if the energy dispersion of the

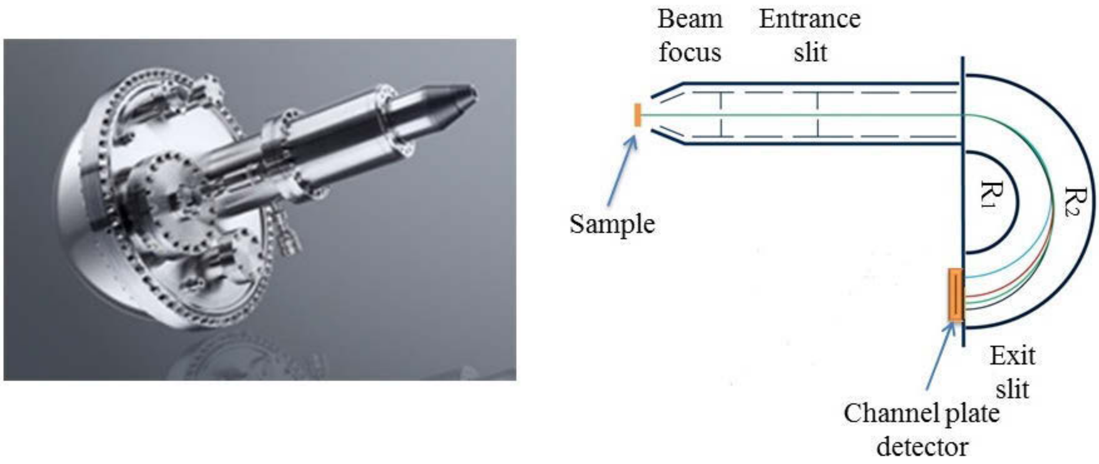

Figure 2.15: *The Phoibos hemispherical electron analyzer.*

electrons at the detector plane, which depends on the pass energy, is sufficiently large, it is possible to acquire the photoemission spectrum in one shot, with an acquisition time of about 100 ms per spectrum.

2.8.1 Combined Spectroscopy and Microscopy on Surfaces (CoSMoS) at Elettra

One of the activities carried out in this PhD project is the implementation of the surface science set-up CoSMoS (Combined Spectroscopy and Microscopy on Surfaces), which belongs to the National Institute of Material Physics (NIMP) in Romania, at the branchline of the SuperESCA beamline of Elettra. This installation was possible thanks to a long-term project on the growth and study of ferroelectric-graphene interfaces with XPS and NEXAFS. CoSMoS uses the same monochromatized beam of SuperESCA. Basically, the synchrotron radiation beam enters first into the main chamber of SuperESCA and then is refocused by a thoroidal mirror (Fig. 2.16) into the XPS chamber of CoSMoS. (Fig. 2.17)

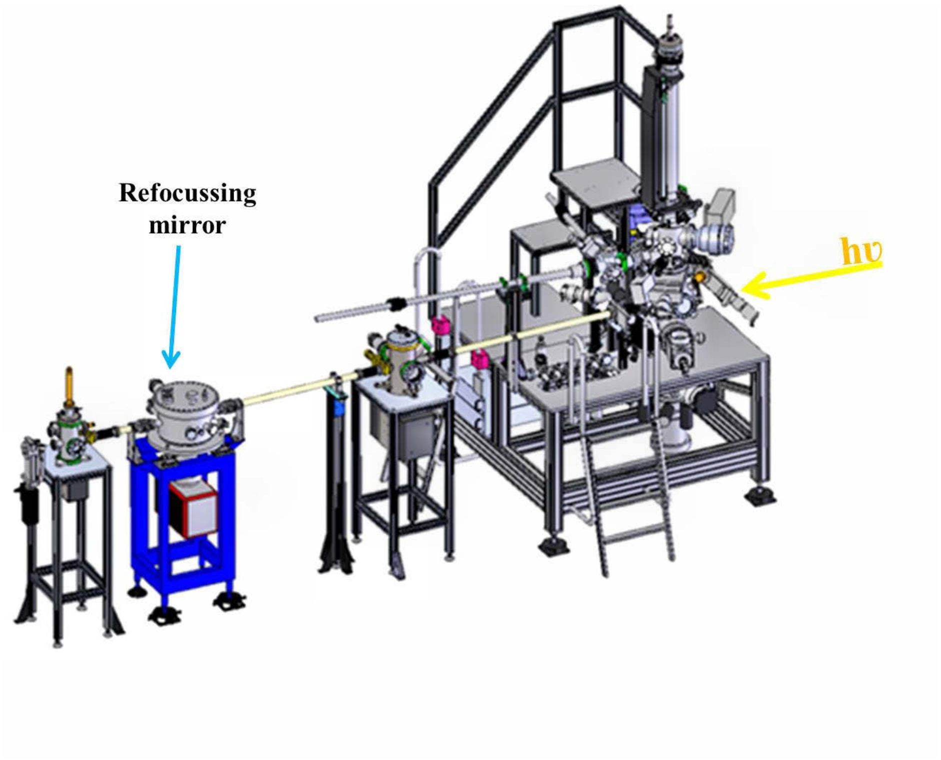

Figure 2.16: *Sketch of the SuperESCA branchline.*

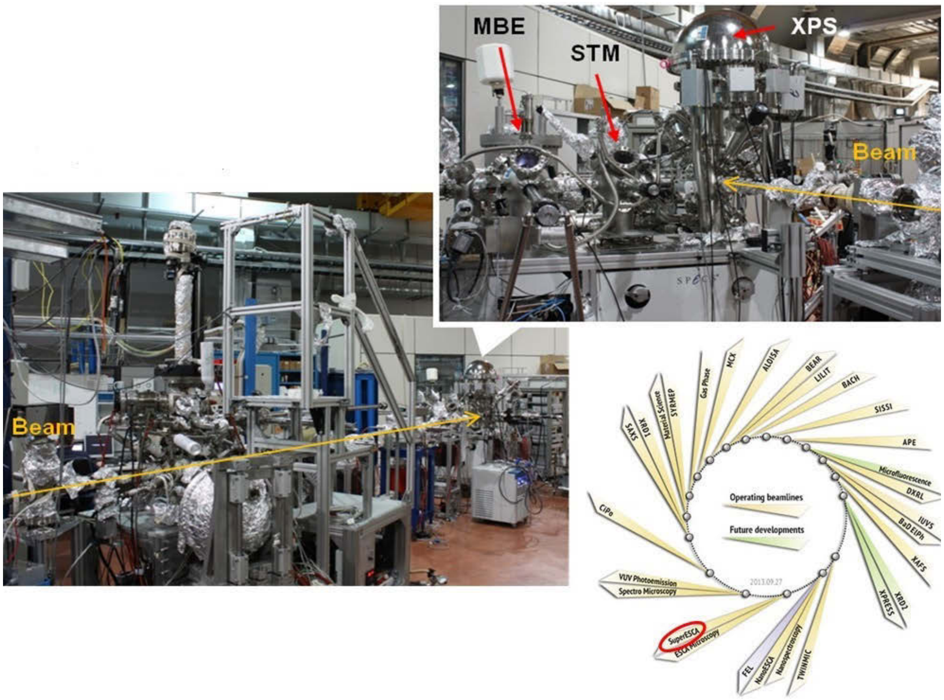

Figure 2.17: *SuperESCA beamline (in the bottom image) and CoSMoS cluster (in the top right corner of the image). The analyzer is standing up-right in the image.*

In Figure 2.18 it is shown a more detailed image of the CoSMoS facility. The system is a single set-up from SPECS which includes three main chambers where samples can be transferred from one to the other through a system of transfer bars. One is dedicated to the molecular beam epitaxy (MBE), the second for Scanning Tunneling Microscopy (STM) and the third one (where the synchrotron beam is connected) for photoemission experiments. The system can host 10-12 samples, accommodated on different storage facilities of the whole setup, which means that all these samples might be prepared and characterized well in advance and ready for synchrotron radiation measurements. Besides the load-lock chamber where the best pressure is 10^{-8} mbar all the others work in the range of $10^{-10} - 10^{-11}$ mbar.

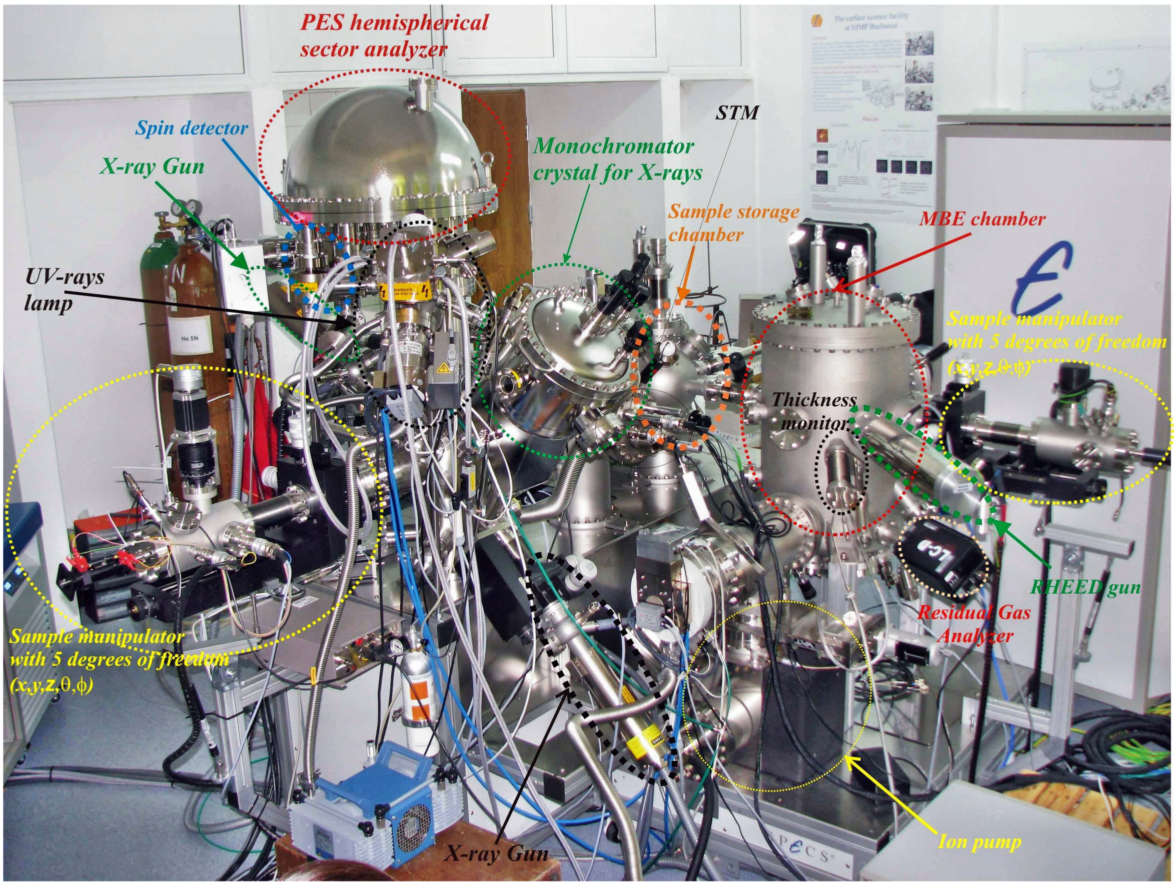

Figure 2.18: *Detailed image of CoSMoS at NIMP.*

In Fig. 2.19 is represented the scheme of the main devices in the MBE chamber. This system is equipped with two sample manipulators, one with 5 degrees of freedom (3 on the x, y, z axes and 2 rotational (Θ and Φ) with cooling capabilities down to 80 K and heating up to about 1300 K and another capable to reach high temperature (1800 K). In the bottom of the chamber are mounted five evaporators with Knudsen cells, one based on electron bombardment with 4 different targets and a RF discharge plasma source. In the MBE chamber are also present a quartz micro-balance (for the calibration of the evaporators fluence rate), a quadrupole mass spectrometer (for the residual gas analysis), a ion gun (for sample cleaning)) and a LEED, RHEED thickness monitor. Basically in the MBE chamber one may synthesize complex systems architectures (atomic clean samples, ultrathin layers, multi-layers or alloys), which can be characterized *in situ* by the following techniques: LEED, RHEED or thermal desorption analysis (by using quadrupole mass spectrometer).

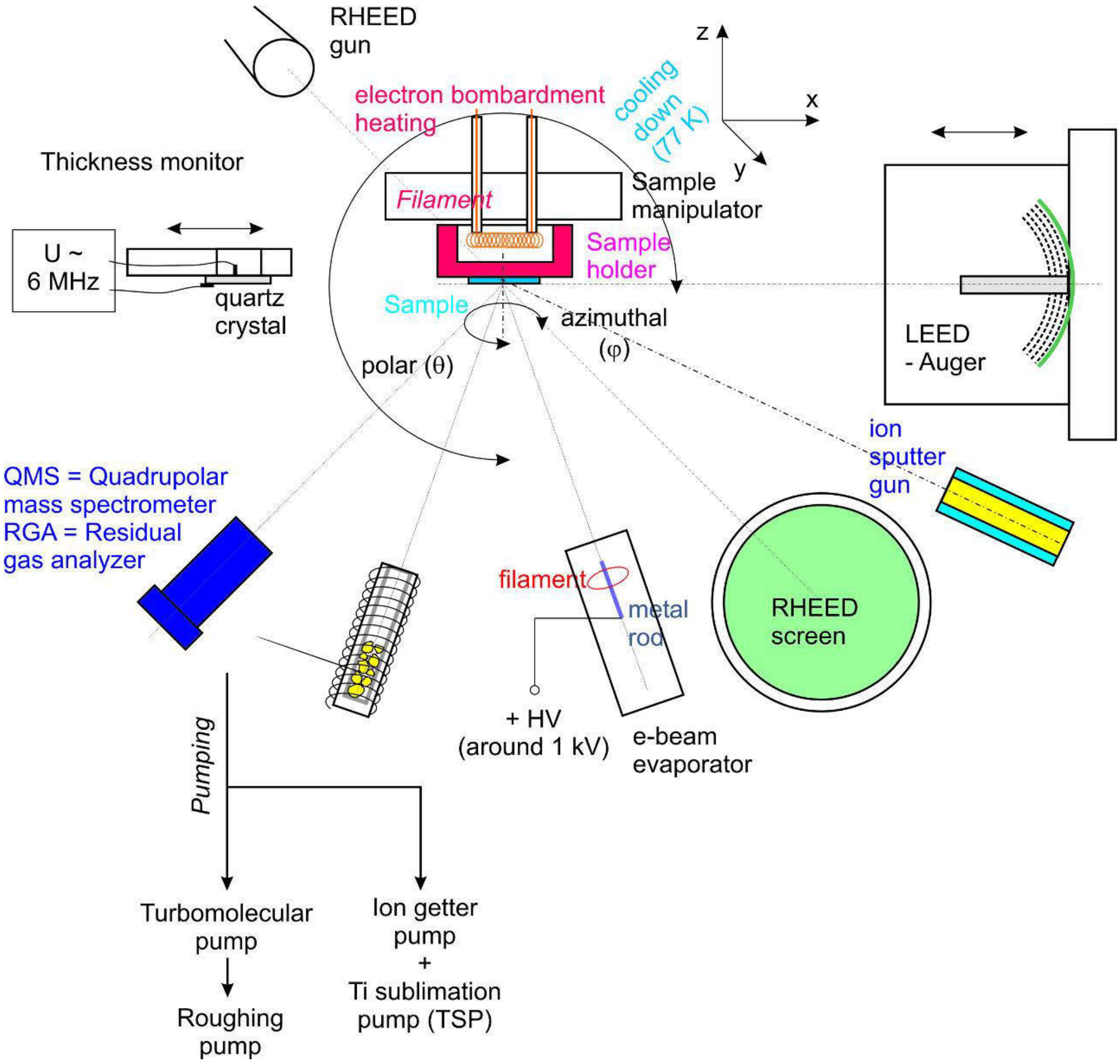

Figure 2.19: *Sketch of all devices present in the MBE chamber.*

The STM microscope, mounted in the second chamber permits scanning tunneling microscopy measurements at variable temperature (80-600 K, see fig. 2.20(a)). In fig. 2.20(b) and (c) are shown atomically resolved images of graphite acquired after the installation of CoSMoS at Elettra. The STM chamber hosts also a sample cartridge where samples can be stored or annealed before STM measurements.

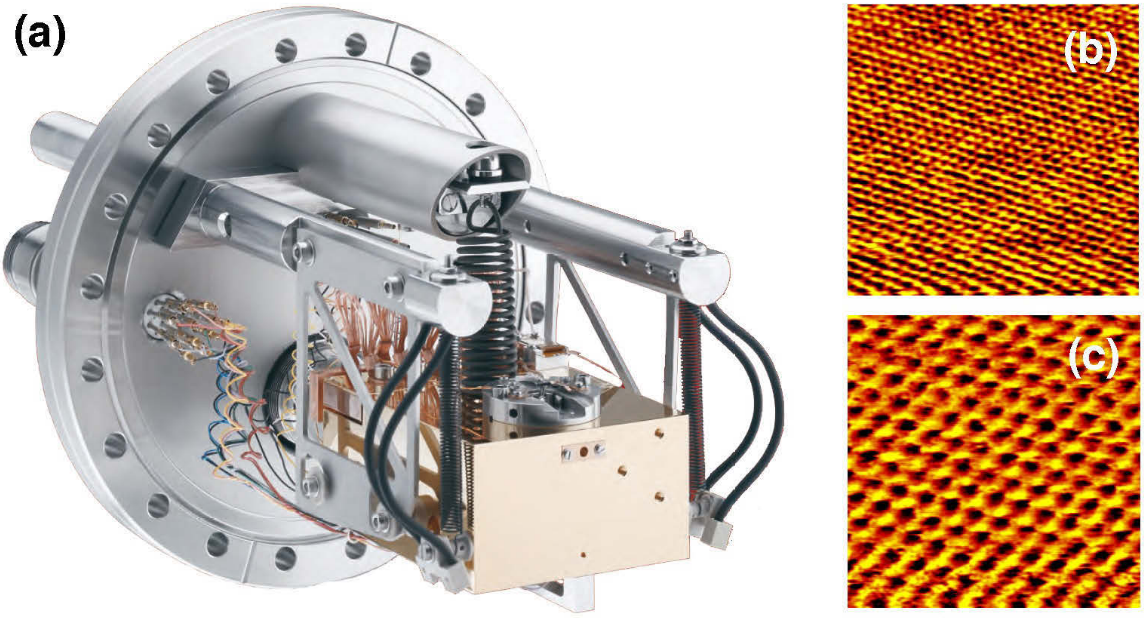

Figure 2.20: *(a) Scanning tunneling microscope with variable temperature (80-600 K (b) 5 x 5 nm*^{2} *and (c) 2 x 2 nm*^{2} *image of graphite.)*

The last chamber is dedicated mainly to the XPS measurements and is composed by:

- sample manipulator (the same as in MBE chamber);
- a conventional monochromatized anode based gun for soft X-rays (Al $K_{\alpha 1}$ 1486.3 eV, Ag $L_{\alpha 1}$ 2984.31 eV);
- a 150 mm Phoibos hemispherical electron energy analyzer (the same of SuperESCA) with a mini-mott spin detector and 6 channeltrons;
- a low energy flood gun (max 500 eV), used to neutralize samples charging effects;
- high energy electron gun (max. 5 keV) for Auger electron spectroscopy and electron energy loss spectroscopy (EELS);
- an ion gun with beam focusing and sample scanning for sample cleaning and compositional profiles investigations;

- a high intensity UV lamp (UVS 300).

One of the main issues for the integration of CoSMoS with the SuperESCA beamline was, besides the proper alignment of the center of the XPS main chamber with the synchrotron beam, to have also the adequate geometry for the measurement of all core levels, in particular of the s-levels. This implies that the analyzer had to be moved from the up-right position shown in Fig. 2.17 which was initially adapted for laboratory measurements with conventional sources at NIMP, to the horizontal position displayed in Fig. 2.21.

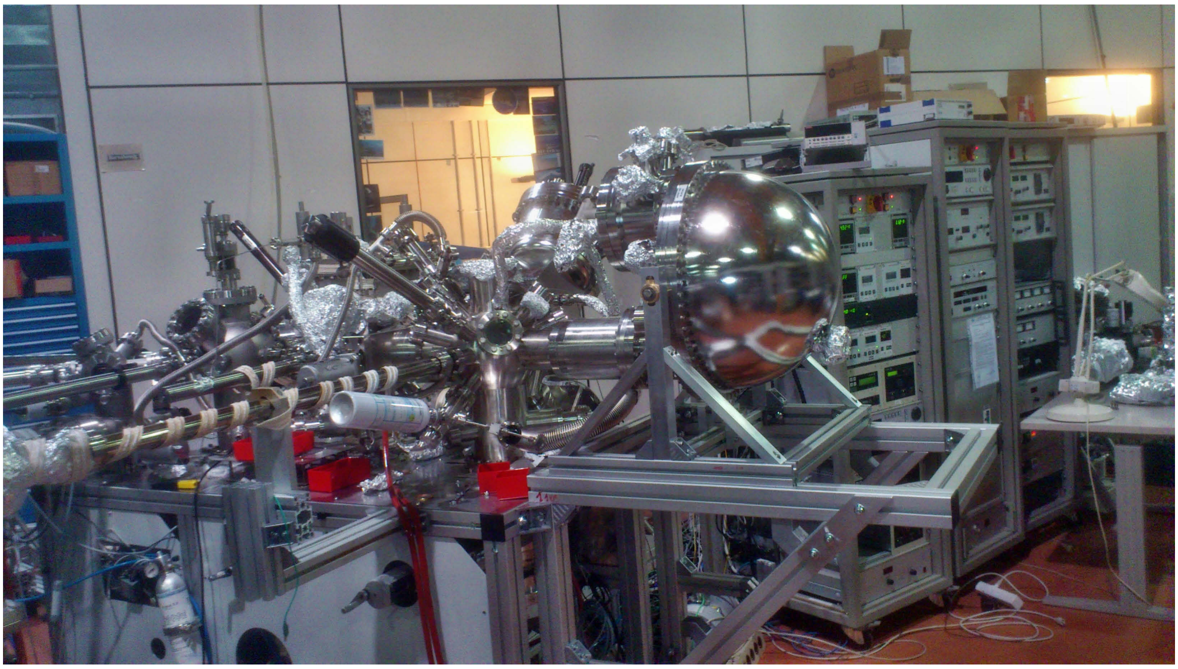

Figure 2.21: *The new position of the hemispherical electron energy analyzer.*

The CoSMoS facility features the rare requisite to combine synchrotron-based photoemission techniques with STM and an MBE deposition system, all the preparation and measurement operations being performed *in situ*.

2.9 The Surface Science Laboratory

The UHV chamber of the Surface Science Laboratory (Fig. 2.22) is optimized for X-ray photoelectron spectroscopy with conventional X-ray sources, electron diffraction and Temperature Desorption Spectroscopy (TDS) experiments. It has a flexible configuration, thanks to the automated flange rotation and positioning system, which allows to control the sample position in front of different instruments via a software interface.

The experimental chamber is equipped with two conventional X-ray sources, a Mg-K_α and Al-K_α (which produce photons with an energy of 1253.6 and 1486.3 eV, respectively) and a 150 mm mean radius hemispherical electron energy analyzer. LEED measurements can be performed with a VG rear-view electron optical system, while the diffraction patterns are collected with a CCD camera. On the other hand, Spot Profile Analysis LEED (SPA-LEED) measurements are performed with a Omicron system, with a custom written acquisition software. Besides photoemission and electron diffraction experiments, TDS can be performed due to the temperature control achievable with the particular sample mounting and to the quadrupole mass spectrometer. Several different evaporators and instruments can be installed on the different flanges of the chamber.

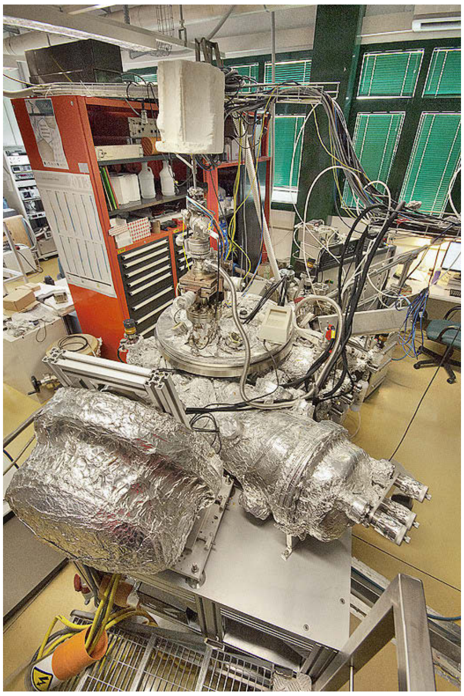

Figure 2.22: *UHV experimental chamber of the Surface Science Laboratory.*

Bibliography

[1] D.P. Woodruff and T.A. Delchar, editors, *Modern Techniques of Surface Science*, Cambridge University Press (1994).

[2] J.H. Park, W.C. Mitchel, L. Grazulis, H.E. Smith, K. Eyink, J.J. Boeckl, D. Tomich, S.D. Pacley, and J.E. Hoelscher, *Epitaxial Graphene Growth by Carbon Molecular Beam Epitaxy (CMBE)*, Adv. Mater. **22**, 4140-4145 (2010).

[3] M. Batzill, *The surface science of graphene: Metal interfaces, CVD synthesis, nanoribbons, chemical modifications, and defects*, Surf. Sci. Rep. **67**, 83-105 (2012).

[4] Y. Dedkov and E. Voloshina, *Graphene growth and properties on metal substrates* , J. Phys.: Condens. Matter. **27**, 303002 (2015).

[5] R. Balog, B. Yorgensen, L. Nilsson, M. Andersen, E. Rienks, M. Bianchi, M. Fannetti, E. Laegsgaard, A. Baraldi, S. Lizzit, Z. Sljivancanin, F. Besenbacher, B. Hammer, T.G. Pedersen, P. Hoffmann, and L. Hornekaer, *Bandgap opening in graphene induced by patterned hydrogen adsorption*, Nat. Mater. **9**, 315-319 (2010).

[6] A.Y. Cho, and J.R. Arthur, *Molecular beam epitaxy*, Sol. St. Chem. **10**, 157 (1975).

[7] N.G. Apostol, *Surface of elemental and oxide semiconductors and interfaces formed by these semiconductors with metals deposited by molecular beam epitaxy* , PhD Thesis,"I.G. Murgulescu" Institute of Physical Chemistry, Bucharest (2013).

[8] I.S. Grigoriev, and E.Z. Meilikhov, *Handbook of Physical Quantities* **11**, CRC Press, 324-337 (1997).

[9] B.D. Chrisey, G.K. Hubler, and J. Wiley, *Pulsed Laser Deposition of Thin Films*, Willey-Inters. **1** (1994).

[10] S. Hüffner, *Photoelectron Spectroscopy: Principles and Applications*, Ed. Springer, Berlin (2003).

[11] W.M. Haynes, *CRC Handbook of Chemistry and Physics*, 75th Ed., Boca Raton-Florida (1996).

[12] G. Binning, and H. Rohrer, *IBM journal of Research and Development*, **30**, 355 (1986).

[13] C.S. Fadley, S.B.M. Hagstrom, M.P. Klein, and D.A. Shirley, *Chemical Effects on Core-Electron Binding Energies in Iodine and Europium*, J. Chem. Phys., **48**, 3779-3794 (1968).

[14] S. Tanuma, C.J. Powell, and D.R. Penn, *Calculations of electron inelastic mean free paths. IX. Data for 41 elemental solids over the 50 eV to 30 keV range*, Surf. Interf. Anal. **43**, 689-713 (2011).

[15] A. Zangwill, *Physics at Surfaces*, Cambridge University Press, New York (1988).

[16] A. Nambu, J.M. Bussat, M. West, B.C. Sell, M Watanabe, A.W. Kay, N. Mannella, B.A. Ludewigt, M. Press, B. Turko, G Meddeler, G. Ziska, H Spieler, H van der Lippe, P. Denes, T.Ohta, Z. Hussein, and C.S Fadley, *An ultrahigh-speed one-dimensional detector for use in synchrotron radiation spectroscopy: first photoemission results*, J. Electr. Spectr. Relat. Phenom. **134-140**, 691-697 (2004).

[17] S. Doniach, and M. Šunjić, *Many-electron singularity in X-ray photoemission and X-ray line spectra from metals*, J. Phys. C: Solid State Phys. **48**, 3779-3794 (1968).

[18] J.J. Joice, M. Del Giudice, and J.H. Weaver, *Quantitative analysis of synchrotron radiation photoemission core level data*, J. Elect. Spectr. Relat. Phenom. **49**, 31-45 (1989).

[19] *János Végh*, *The Shirley Background revised*, J. Elec. Spect. **151**, 159-164 (1989).

[20] W. Zhang, A. Nefedov, M. Naboka, L. Cao, and C. Wöll, *Molecular orientation of terephtalic acid assembly on epitaxial graphene: NEXAFS and XPS study*, Phys. Chem. Chem. Phys. **14**, 10125-10131 (2012).

[21] J. Stöhr, *NEXAFS Spectroscopy*, Springer Science & Business Media (2013).

[22] G. Hähner, *Near edge X-ray absorption fine structure spectroscopy as a tool to probe electronic and structural properties of thin organic films and liquids*, Chem. Soc. Rev. **35**, 1244-1255 (2006).

[23] M.O. Krause, *Atomic radiative and radiationless yields for K and L shells*, Journal of Physical and Chemical Reference Data **8**, 307-327 (1979).

[24] H. Winick, and S. Doniach, *Synchrotron radiation research*, Springer Science & Business Media (2012).

[25] J.B. Pendry, *Low-Energy Electron Diffraction*, Academic Press, London (1974).

[26] J.C. Vickerman, I.S. Gilmore, *Surface Analysis, The Principal Techniques*, 2^{nd} Ed., Springer, Berlin (2003).

[27] C. Davisson and L.H. Germer, *Diffraction of Electrons by a Crystal of Nickel*, Phys. Review **30** (1927).

[28] A. Hoffmann, *The physics of synchrotron radiation*, Cambridge University Press, Volume **20** (2004).

[29] A. Abrami, M. Barnaba, L. Battistello, A. Bianco, B. Brena, G. Cautero, Q. H. Chen, D. Cocco, G. Comelli, S. Contrino, F. DeBona, S. Di Fonzo, C. Fava, P. Finetti, P. Furlan, A. Galimberti, A. Gambitta, D. Giuressi, R. Godnig, W. Jark, S. Lizzit, F. Mazzolini, P. Melpignano, L. Olivi, G. Paolucci, R. Pugliese, S.N. Qian, R. Rosei, G. Sandrin, A. Savoia, R. Sergo, G. Sostero, R. Tommasini, M. Tudor, D. Vivoda, F.Q. Wei, and F. Zanini. *SuperESCA, First beamline operating at Elettra*, Rev. Sci. Instr. **66**, 1618-1620 (1995).

[30] G. Cautero, R. Sergo, L. Stebel, P. Lacovig, P. Pittana, M. Predonzani, and S. Carrato, *Two-dimensional detector for pump-and-probe and time resolved experiments. Nuclear Instruments and Methods in Physics Research Section A: Accelerators, Spectrometers, Detectors and Associated Equipment* **595**, 447-459 (2008).

Chapter 3

Carbon Molecular Beam Epitaxy (MBE) of graphene on Ir (111)

3.1 Introduction

Among the transtion metal surfaces that can be used for the epitaxial growth of graphene, Ir(111) is the one presenting a weak C-substrate interaction [1, 2] which, however guarantees a very high quality graphene, with a low density of defects [3, 4]. For this reason, we choose Ir(111), a widely studied surface employed for the graphene synthesis by CVD, to monitor the growth and characterize the carbon layers obtained using molecular beam epitaxy.

This study was the starting point of our project aiming to demonstrate that this approach is a viable method to grow graphene also on substrates where dissociation of hydrocarbons is precluded. For example, carbon molecular beam epitaxy has been used recently to synthesize graphene on noble metals such as Pt (111), Au (111) [5] or Ag(111) [6] at low surface temperature.

The idea of using carbon MBE is not entirely new. This method was successfully implemented for the first time by Moreau and co-workers in 2009 when they used it to grow graphene on SiC [7]. Later it has been demonstrated that this method can provide the possibility, besides carbon segregation from the substrate [8], to grow a second layer of graphene. Actually, in 2011, Niu and co-workers succeeded to grow a second layer of graphene on a Ir(111) substrate using an elemental carbon source after the first layer was grown in advance using the CVD method [9].

The first section of this chapter is dedicated to the investigation of the different C species which are produced and deposited through the C sublimation process from the high purity graphite rod. The comparison of high-resolution XPS data with ab initio DFT calculations allowed us to find that different carbon clusters can be formed on Ir(111) upon low temperature carbon deposition. Besides carbon monomers, also dimers, trimers and larger clusters are detected through C 1s core level measurements. The signal of carbon monomers is then used as a fingerprint of the presence of carbon monomers during the early stages of graphene growth by ethylene chemical vapour deposition at high temperature. In the second part of the chapter are described the properties of the C layers produced at high temperature using carbon MBE. This method allows to prepare graphene multi-layers which were analyzed by means of high-resolution XPS and LEED.

3.2 Carbon monomers and dimers on Ir(111): a study at low temperature deposition

The interest of the materials science community in carbon monomers (C_1) and dimers (C_2) has grown considerably in the last years because of their role in the synthesis of high-quality graphene (Gr) monolayers on solid surfaces [10, 11, 12]. Carbon clusters, especially those formed by a small number of atoms, play an important role in determining the different atomistic mechanisms for the epitaxial growth of graphene by means of chemical vapour deposition (CVD). The carbon monomers concentration and the rate at which adatoms are generated from hydrocarbon feedstock are relevant quantities for explaining the non-linear growth kinetics observed on different surfaces [13]. The control of monomers supersaturation is an effective approach to modify not only the growth rate, but also the morphology and the orientation of the Gr islands [14]. In addition, monomers are essential for the growth of the graphene islands both through direct attachment to the Gr edges and through the formation and attachment of larger C clusters [15].

As for monomers, also dimers play an important role in the formation of high-quality Gr monolayers characterized by a low density of defects such as mono- and di-vacancies, disclinations, dislocations and domain boundaries [16]. For example, in the case of copper surfaces, where they represent the dominant feeding species for Gr growth [17, 18], dimers have either a diffusion- or an attachment-limited aggregation behavior depending on the crystallographic surface orientation [19, 20]. More specifically, while the rate determining step for Gr growth on Cu(111) is the energy barrier for their surface diffusion, in the case of Cu(100) the limit is given by the energy barrier for the attachment of C_2 to zig-zag and arm-chair terminated Gr edges. On the other hand, the formation of dimers on transition metal surfaces showing a large C-metal bond strength (such as Ir and Ru) is energetically unfavorable [15]. The important role played by dimers in Gr growth has been established also in the case of Ru(0001) [21, 22], Co(0001) [23, 24], Ni(111) [25, 26] and even for CuNi surface alloys [27]. Besides their relevance for graphene epitaxial growth, C_2 species are extremely important for the formation of all carbon-based three-dimensional materials [28], for the synthesis of carbon quantum dots and as building blocks for metal-alkynide and alkynide complexes [29, 30].

The energetics for monomers and dimers attachment to step edges, which represent the preferred Gr nucleation sites, have been investigated by means of density functional theory on different metal surfaces [21]. While the step edges on Ir(111) surface cannot serve as efficient trapping centres for single C_1 adatoms, they can readily facilitate the formation of C_2 dimers. The opposite was found in the case of Cu(111). Chen *et al.* explained this contrasting behavior as due to the interplay between C-C and C-metal interaction strength.

The detection of C_1 monomers using a spectroscopic approach is not an easy task and for this reason their presence on solid surfaces has often been revealed by exploiting changes in low energy electron reflectivity [14]. In fact, the diffusion barrier of monomers and dimers is quite low [21], so that they can rapidly diffuse and attach to step edges at the temperatures at which high-quality graphene is typically grown on transition metals and their surface density is therefore low.

In order to overcome these problems and produce a high density of C monomers and dimers in a stable configuration on the Ir(111) surface, we have employed carbon MBE from a graphite target and low temperature deposition. As discussed below this method allowed us to produce several C species which we could reveal and characterise by means of high energy-resolution XPS supported by

DFT calculations. The results of this characterisation have been then applied for a spectroscopic study of the high temperature CVD growth of graphene with ethylene where the C 1s core electron binding energy of C monomers was used as fingerprint for the detection of carbon adatoms forming the lattice gas which constitutes the C feedstock of the graphene growth [14].

All the theoretical calculations presented in the next sections were performed by the group of Prof. Lev Kontorovich from the King's College in London.

3.3 Experimental methods

All the measurements were performed at the SuperESCA beamline of Elettra. The Ir(111) single crystal was cleaned by Ar^{+} sputtering at room temperature (E=1.5 keV), annealing to 1400 K, oxygen cycles to remove residual carbon (in the range 570-1070 K at P=5 x 10^{-8} mbar) and final hydrogen treatments to remove residual oxygen traces (P=5 x 10^{-8} mbar, T=300-770 K). Surface cleanliness was checked by inspecting C 1s, S 2p and O 1s signals and by measuring the Ir $4f_{7/2}$ signal, which is known to show a surface core level shift (CLS) of -550 meV when the surface is clean [31]. Prior to the photoemission measurements, we acquired LEED images of the clean surface, which show intense and narrow integer order diffraction spots with a low background.

Carbon deposition was carried out at T=80 K by employing the carbon source described in Chapter 2. During deposition, the pressure was always kept below 1 x 10^{-9} mbar to prevent surface contamination. The Ir surface was placed at a distance of 80 mm from the carbon evaporator, resulting in a carbon flux of $\sim$ 1.8 x 10^{-3} ML/s. The carbon coverage was calibrated by comparing the C 1s photoemission intensity with the one measured for a single layer of graphene on Ir(111)(3.87 x 10^{15} $atoms/cm^{2}$=2.47 ML, where 1 ML corresponds to one C atom per each Ir substrate atom). The C 1s core level spectra acquired after C deposition by means of MBE were measured at $h\nu = 400$ eV and at normal emission, with an overall energy resolution of 50 meV, that was determined by measuring the broadening of the Fermi edge on a silver crystal. Core level spectra binding energies were always calibrated with respect to the Fermi level. The high-resolution spectra presented in this work were measured at T=80 K in order to reduce the vibrational broadening and enhance the possibility to better distinguish different components, as well as to ensure that the C species were stable during the whole experiment, being their thermal energy low with respect to their diffusion and reaction barriers. In the case of graphene synthesis by ethylene, the uptake was instead performed at 820 K by using a supersonic molecular beam [32], with a local C_2H_4 pressure of 5 x 10^{-8} mbar. The fast-XPS data acquired during this uptake were measured in real time in snap-shot mode. The short acquisition time for a single C 1s spectrum (500 ms), permits to probe *in-situ* the evolution of the different carbon species during the ethylene uptake. Besides the increased number of spectra available over the whole uptake experiment, this operation mode allows more efficient sampling of the low coverage limit, when we expect, according to previous LEEM investigation, to detect the presence of C monomers.

The data analysis was performed by fitting all the C 1s and Ir $4f_{7/2}$ spectra with Doniach -Šunjić (DS) functions [33]- characterized by the singularity index α and the Lorentzian width L convoluted with a Gaussian G. The inelastic contribution to the photoemission spectra was described with a linear background. The procedure for the determination of the DS lineshape parameters is discussed in detail in a following section.

3.4 Theoretical methods

The geometry optimisation calculations for the carbon clusters were performed using the CP2K code [34]. The Ir(111) surface was represented with an 8 x 8 cell of four layers, and the vacuum gap was greater than 15 Å. Two bottom layers were fixed to the Ir bulk geometry while the upper layers were allowed to relax. For the geometry relaxation calculations the generalised gradient approximation (GGA) was used, along with the PBE exchange-correlation functional [35], Goedecker-Teter-Hutter (GTH) pseudopotentials [36], and the optimised m-DZVP basis set [37] (with a plane wave cutoff energy of 300 Ry). The DFT-D3 method was used for van der Waals forces [38]. The geometries were relaxed until the force on the atoms was less than 0.038 eV/Å. The CLS calculations were performed using the Vienna ab-initio software package (VASP) [39, 40, 41]. The Ir(111) surface consisted of a 4 x 4 cell, again with four layers of which the bottom two layers were fixed. The CLS for a particular C atom in a cluster was calculated [42] as the energy difference between the system with a core electron promoted to the valance band $E(n_c - 1)$, and the energy of the unexcited system $E(n_c)$:

$$E_{CLS} = E(n_c - 1) - E(n_c) \tag{3.1}$$

3.5 Results and discussion

3.5.1 Experimental results

In Fig. 3.1 are represented the sequences of C 1s core level spectra measured after each deposition (thick blue lines) of 0.11 (a), 0.32 (b) and 0.74 ML (c) of carbon and after subsequent annealing to increasing temperatures (thin lines). The two spectra measured at T=80 K for both the low (Fig. 3.1 (a)) and medium (Fig. 3.1 (b)) coverage show two major components at about 283.4 (M) and 283.9 (D) eV. From this first inspection it appears that at least two non-equivalent species are present on the surface already at low coverage. Besides the M and D components, the highest coverage spectrum measured after deposition at low temperature (Fig. 3.1(c)) shows an additional shoulder (C) at 284.7 eV. It is worth to underline that while the D component is quite broad with a full width half maximum of about 0.6 eV, the M peak, though narrower, displays a shoulder at lower binding energy. This suggests that, for the highest coverage, at least four non-equivalent carbon species, *i.e* in a slightly different local environment, have been produced after deposition.

The annealing process induces clear modifications in the C 1s core level lineshape, the major effects being (i) a reduction of the M component and (ii) an increase and a shift to lower binding energies of the D and C components. The reasons of the C 1s spectral changes can be searched in the modification of both, the adsorption configurations and the density of the different surface species, as well as in the formation of different carbon clusters as will be discussed below.

For the high coverage deposition the spectrum obtained after annealing to 1270 K, is included which is known to produce large graphene islands [43]. The binding energy of the main peak at 284.1 eV is in agreement with previous findings

[44, 45, 46], while the shoulder at 284.6 eV could be assigned to carbon atoms in defective configurations [47].

In order to obtain further information about the local carbon atoms configuration, along with the variations of the electronic structure of substrate Ir atoms, Ir $4f_{7/2}$ core level spectra were measured together with the C 1s ones. They are displayed in Fig. 3.2, which shows a series of spectra corresponding to different carbon coverage, from the clean surface (bottom), to the highest C structure (top). As already reported [31] the spectrum corresponding to the clean Ir(111) surface can be described by two peaks: the higher binding energy component at 60.85 eV, originates from subsurface and deeper layers, while the lower BE peak S_0, shifted by -550 $\pm$10 meV with respect to the bulk peak, originates from the topmost Ir atoms. A two component analysis gives best fit values for the Γ, α and G parameters respectively of 0.25 eV, 0.10, and 0.10 eV for the bulk, and 0.25 eV, 0.17, and 0.12 eV for the surface component.

All the spectra can be properly fitted by adding in sequence new surface components, as revealed by the low fitting residual and by the chi-square analysis. In order to evaluate the intensity and CLSs of the different surface components induced by the proximity of C atoms, the Ir $4f_{7/2}$ spectra were fitted, for each of the C doses. The fit was performed by fixing the lineshape parameters of the bulk peak, while all the surface components were constrained to be equal to those found for the clean surface.

The low carbon coverage of 0.11 ML leads to the appearance of two additional core level shifted components, S_1 and S_2, shifted by -430$\pm$20 and -220$\pm$20 meV with respect to the bulk one, while the original S_0 surface peak intensity decreases. Upon increasing the C coverage (0.32 ML spectrum), a further decrease of S_0 is observed, accompanied by the growth of a third carbon-induced surface component, S_3, at a binding energy close to the BE of the bulk component (-120$\pm$ 20 meV). Finally, in order to properly fit the 0.77 ML spectrum (Fig. 3.2 top), a new component, with a positive surface CLS (+180$\pm$20 meV), had to be included. Although the different components cannot be unambiguously assigned to specific cluster configurations, the trend observed can be explained as due to a progressive increase in the coordination of the first-layer Ir atoms with C atoms: according to what was measured before for several atomic adsorbates on a variety of transition metal surfaces [48, 49, 50, 51, 52, 53, 54, 55], surface core level shifted components are linked to surface atoms forming a single, double and even larger number of bonds with adsorbates. However this model is over simplified in the present case, as it only considers the number of C atoms coordinated with Ir atoms, while possible differences in the local geometry are not taken into account. For example, within this approach the adsorption of two C monomers results in the production of the same surface CLS as for a single carbon dimer. Nevertheless, from a qualitative point of view, the results of the Ir $4f_{7/2}$ core level analysis suggest that the surface gets increasingly occupied by C species in such a way that at a coverage of 0.77 ML, the density of pristine first-layer Ir atoms not coordinated with adsorbates is negligible. This indicates that at the highest coverage the system is formed by a large number of different and contiguous C clusters placed in non-equivalent configurations. On the basis of these results the C 1s core level analysis was carried out only for the two low coverage systems, namely 0.11 and 0.32 ML.

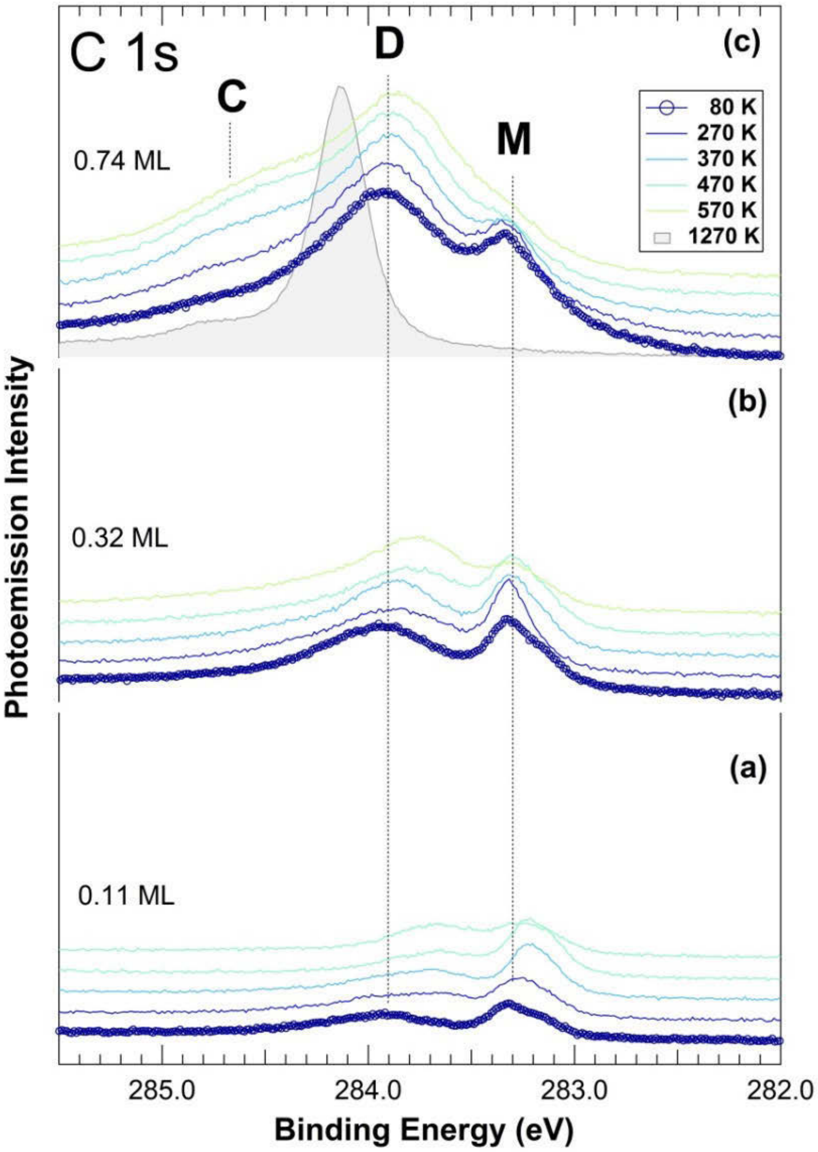

Figure 3.1: *C 1s spectra after deposition (T=80 K) of (a) 0.11 ML, (b) 0.32 ML and (c) 0.74 ML carbon coverage (dotted blue lines), and after subsequent annealing to increasing temperature (thin lines). Spectra are measured at hν=400 eV and normal emission. The gray filled spectrum corresponds to graphene island formation. The binding energy positions of carbon monomers (M), and dimers (D) and larger clusters (C) are indicated.*

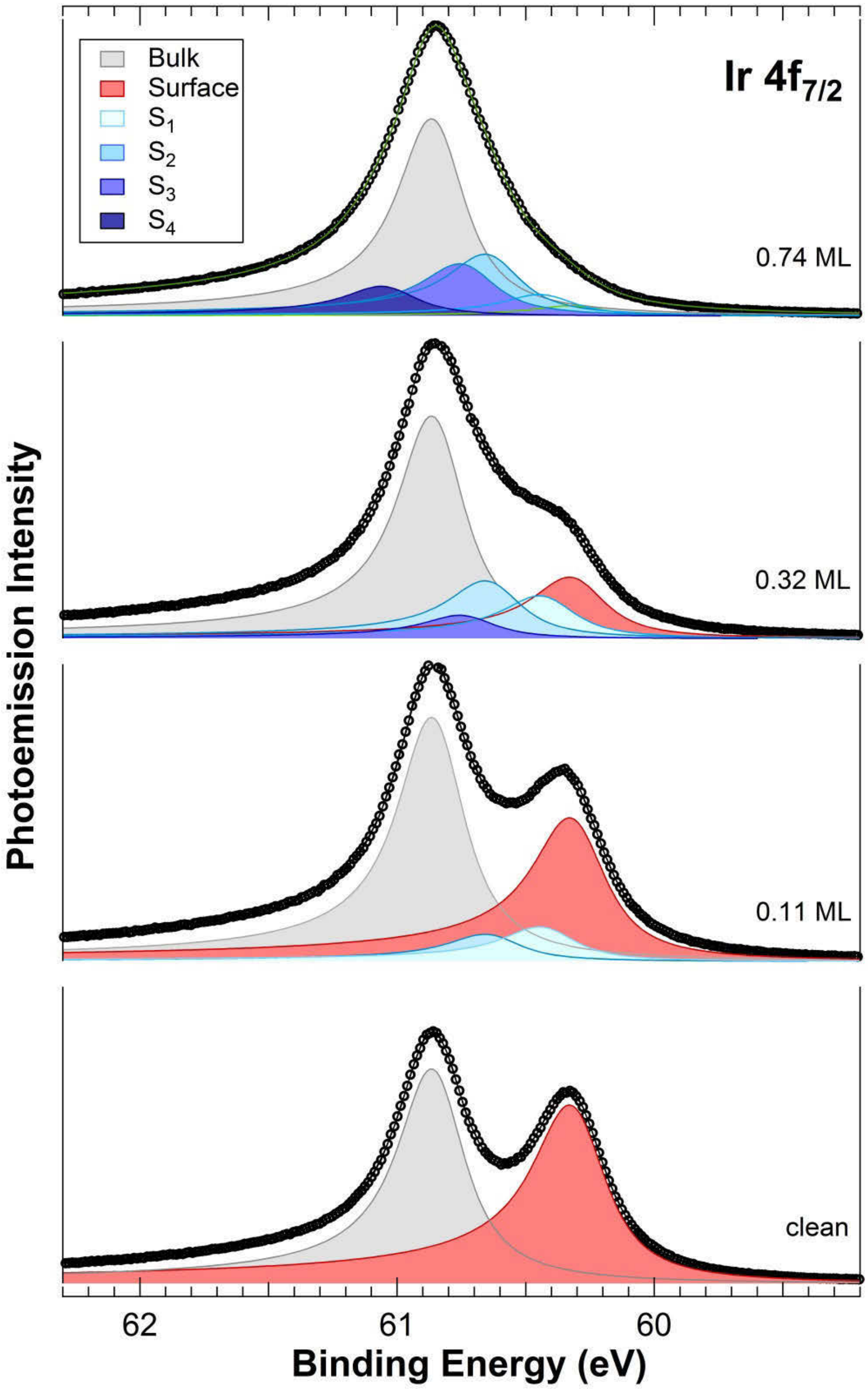

Figure 3.2: *Ir $4f_{7/2}$ core level spectra corresponding to the Ir (111) surface after cleaning (bottom) and after deposition on different carbon coverages. Deconvoluted bulk (grey) and surface (red) components are shown together with carbon-induced surface core level shifted peaks (S_1-S_4). Spectra are measured at hv=200 eV.*

3.5.2 Theoretical results: cluster configurations and core levels

To explain the origin of the different components in the C 1s photoemission spectra, DFT calculations were performed in order to investigate the preferred adsorption sites, adsorption configuration and formation energies of carbon clusters with different sizes, ranging from monomers (C_1) to pentamers (C_5). In Fig. 3.3 are presented the DFT results. For all these clusters (C_1-C_5) the C 1s CLS of each of their atomic constituents was calculated, as reported in Table 3.1. In particular, carbon adatoms (C_1) can adsorb in three configurations, i.e. TOP, three-fold hollow-either FCC or HCP-, while the bridge adsorption site is energetically unstable and relaxes to the hollow site. The favoured adsorption is HCP, with an energy gain of 0.15 eV with repect to the FCC, while the TOP site is considerably less stable. By setting the zero of the binding energy scale to the value of the calculated C 1s core electron binding energy for the C monomers in HCP ($C_{1,A}$) shifts of -0.12 ($C_{1,B}$) and +0.11 ($C_{1,C}$) eV for monomers in FCC and TOP sites, respectively, were found. Carbon dimers (C_2) are stable only when the two C atoms (C-C bond length of 1.38 Å) are placed in FCC and HCP adsorption sites: being the two carbon atoms non-equivalent, the C 1s BE is shifted by +0.51 and +0.65 eV respectively for the C atoms that locally occupy the FCC ($C_{2,A}$) and HCP ($C_{2,B}$) configurations.

Finally, the most stable adsorption sites for C trimers (C_3) are those with an almost linear atomic arrangement whose central atoms are placed close to either FCC ($C_{3,B}$) or HCP ($C_{3,E}$) sites, but slightly out of axis, being displaced towards the nearest-neighbour first layer Ir atoms. The two C atoms placed at the edges in each trimer are instead both in HCP ($C_{3,A}$ and $C_{3,C}$) or FCC sites ($C_{3,D}$ and $C_{3,F}$), respectively. The two adsorption configurations are energetically degenerate. The corresponding CLS for both types are positive (see Table 3.1) with a negligible difference between the values calculated for the side atoms of each configuration: these values are a further indication of the high-symmetry configurations of the C_3 clusters.

It is clear that C_1 monomers in FCC and HCP sites are energetically favorable with respect to dimers and trimers, in agreement with previous experimental and theoretical findings [21]. This is also valid for the formation energies of clusters made of 4 (C_4) and 5 carbon (C_5) atoms, which are positive, as shown in Fig. 3.3 (right side). As a consequence it is expected that the density of monomers on Ir(111) terraces during high-temperature ethylene molecular dissociation, which is known to produce only C adatoms [56], is much larger than the density of C_2-C_5.

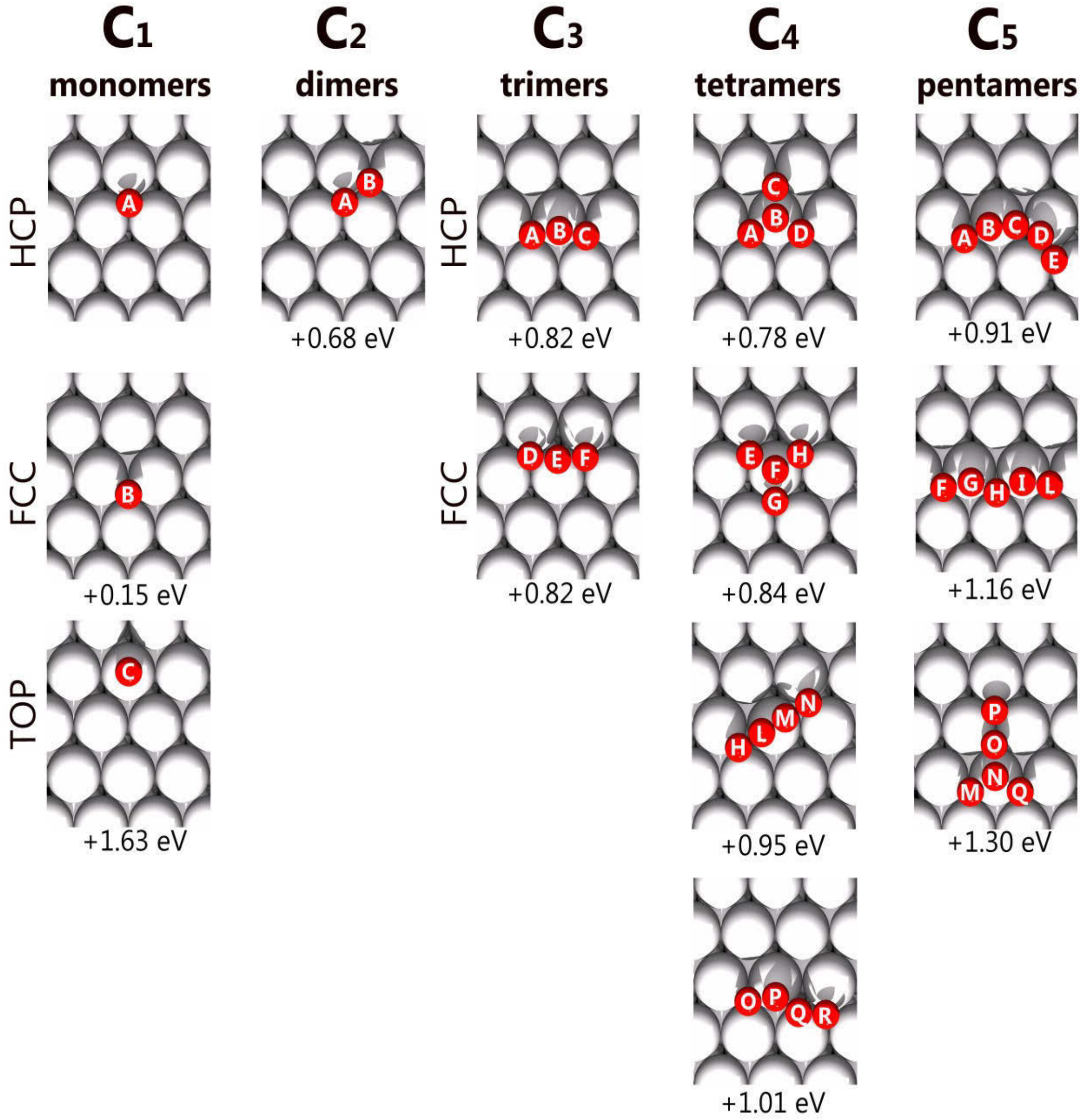

Figure 3.3: *Stable configurations of the carbon species adsorbed onto the Ir(111) surface. The formation energies of each species are also included. Non-equivalent carbon atoms are labelled with different letters.*

	Monomers	**Dimers**	**Trimers**	**Tetramers**	**Pentamers**
A	0	+0.650	+0.920	+0.727	+0.745
B	-0.120	+0.510	+0.370	+0.152	+0.351
C	+0.110		+0.920	+1.022	+1.486
D			+0.780	+0.543	+0.310
E			+0.190	+0.609	+0.559
F			+0.780	+1.514	+0.680
G				+0.614	+1.908
H				+0.614	+1.270
I				+0.773	+0.675
L				+1.488	+0.688
M				+0.773	+0.828
N				+0.773	+0.366
O				+0.890	+0.343
P				+0.679	+0.164
Q				+0.651	+0.797
R				+0.972	

Table 3.1: *Calculated C 1s CLS of different cluster atoms.*

3.5.3 Analysis of low temperature C 1s core level spectra

The analysis of the C 1s spectra (Fig. 3.4) was performed on the basis of the aforementioned theoretical results. The search for the optimal parameters in terms of C 1s lineshape and CLSs was performed in their multi-dimensional space by adopting an efficient strategy to understand correlation effects between parameters, which has already been successfully used in previous works [57]. In particular, the χ^2 contour plots were analysed, in which the evolution of the χ^2 is mapped while two fitting coefficients are simultaneously varied, and the presence of deep and localized minima in the phase space diagram was evaluated. The values obtained for the other free fitting parameters were plotted in parallel, as a function of the same coordinates. This procedure allowed us to estimate the error bar affecting the fitting parameters:

for each contour plot, the region where the χ^2 lays within 10% from its minimum was selected and the corresponding variation in the fitting coefficients was calculated.

The analysis started from the data acquired for the lowest coverage (see Fig. 3.4 (bottom)), where it is expected that only a few C species are present on the surface, namely single C_1 adatoms or very small clusters, such as C_2 dimers and C_3 trimers. The calculated C 1s CLSs suggest that the C monomers are the surface species with the lowest C 1s BE, and therefore could originate the narrow spectral components in the range between 283.5 and 283 eV.

The calculated and the experimental binding energy scale were aligned in such a way that the highest intensity component at about 283.35 eV corresponds to the most favorable configuration, *i.e.* the C_1 species in HCP sites ($C_{1,A}$), and the BE of all other components is expressed in terms of their separation from this one.

The lineshape of the components originating the M double peak was firstly determined. This was done by analyzing the region of minimum χ^2 of the fit while ranging step by step the Gaussian parameter G_1 around an initial guess and the CLS around the theoretically calculated value. This procedure was repeated twice, allowing the Lorentzian L and the asymmetry parameter α, one at a time, to relax for each point in the parameter space explored. Using this procedure, we found a CLS of -170 meV between monomers adsorbed in HCP and FCC (see Fig. 3.5 (a)), in good agreement with the theoretically calculated value of -0.12 eV.

This procedure was then adopted to determine the lineshape and CLS for the highest binding energy photoemission components where, according to the theoretical CLSs, the spectral intensity is most probably originated by the presence of dimers and trimers. Their DS lineshape parameters (L and α) were fixed to the values already found for the low binding energy component. A further constraint was used for the intensities I of the different carbon species, by keeping I($C_{2,a}$)= I($C_{2,b}$), I($C_{3,a}$)= I($C_{3,b}$)= I($C_{3,c}$) and I($C_{3,d}$)= I($C_{3,e}$)= I($C_{3,f}$). Moreover, since the deconvolution of these components cannot be easily performed due to their small CLSs (as pointed out in the calculations), we decided to fix their relative shifts to the theoretically calculated values, refining the BE shift between all of them and the reference (the monomers in HCP sites), and the lineshape was kept equal for all these components – *i.e.* a single parameter for the Gaussian $G_{2,3}$ of all C_2 and C_3 clusters photoemission components was used. We then monitored the evolution of the χ^2 as a function of this Gaussian G and of their CLS from the HCP monomer. The image plot of the minimum χ^2, reported in Fig. 3.5 (b), reveals that the CLS experimental results are consistent with the theoretically calculated values to within 70 meV. The best lineshape parameters are L=120 meV, α=0.117, while the Gaussian values are G_1=120 and $G_{2,3}$=316 meV, for monomers and dimers/trimers respectively.

	C_1- **HCP**	C_1- **FCC**	C_2	C_3- **HCP**	C_3- **FCC**	**others**	**Total**
Experiment	0.037 (32.5%)	0.021 (18.5%)	0.040 (35%)	0.016 (14%)	0	0	**0.114**
Random Deposition Model	0.0478 (42%)	0.0478 (42%)	0.0154 (13.5%)	0.0012 (1%)	0.0012 (1%)	0.006 (0.5%)	**0.114**

Table 3.2: *Coverage of different components calculated from experimental data and from a random distribution model.*

The fitting residual, which shows no appreciable modulations, suggests that the system is composed by clusters formed by at most three atoms. The intensity of the different components (see Table 3.2) provides the coverage and concentration of monomers (in HCP and FCC adsorption sites), dimers and trimers.

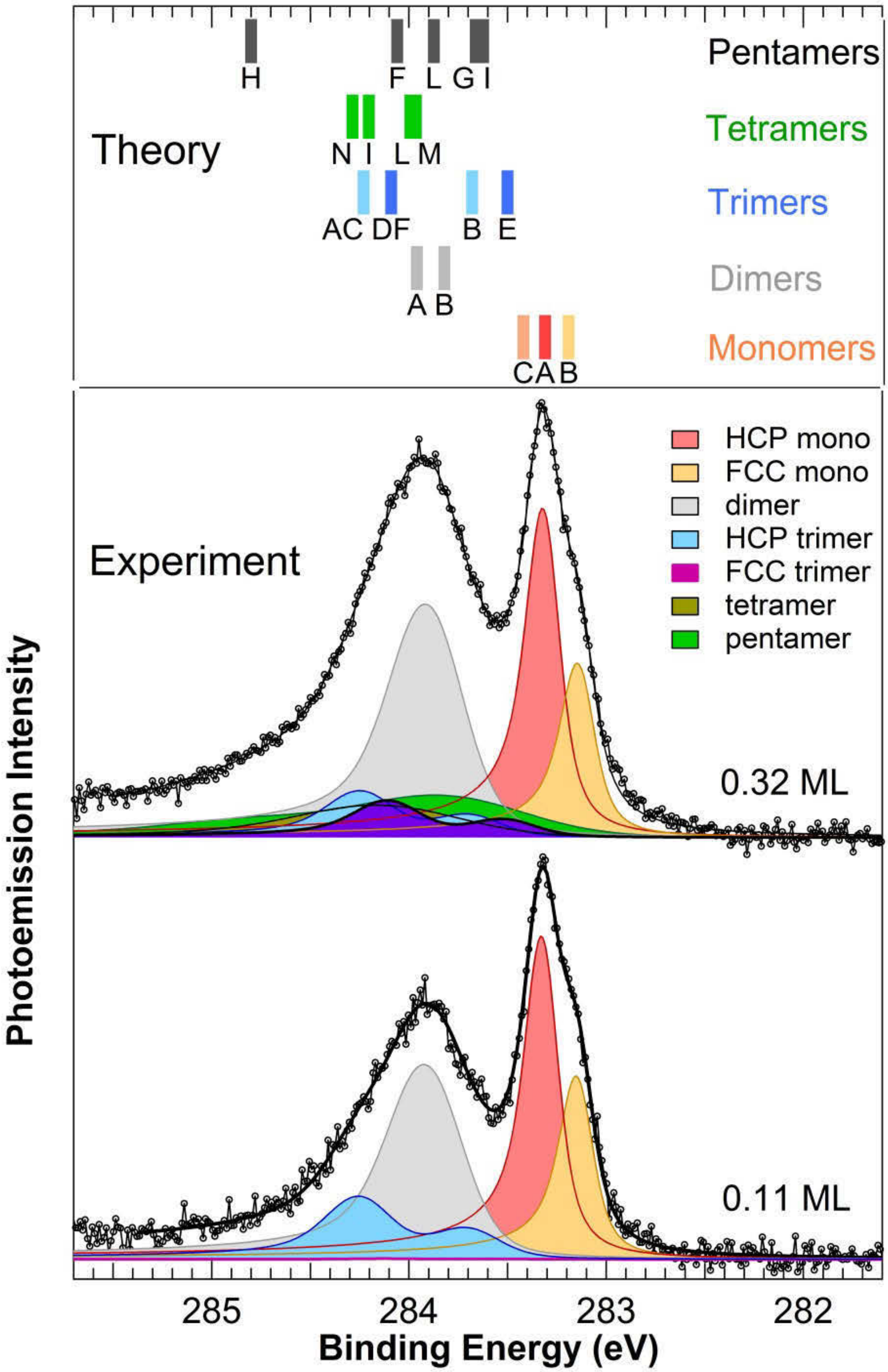

Figure 3.4: *Calculated C 1s core level binding energies (top) and C 1s spectra after deposition of 0.11 ML (bottom) and 0.32 ML (middle) carbon coverage (T= 80 K) together with the deconvoluted components of each carbon species. Spectra are measured at hν=400 eV and in normal emission.*

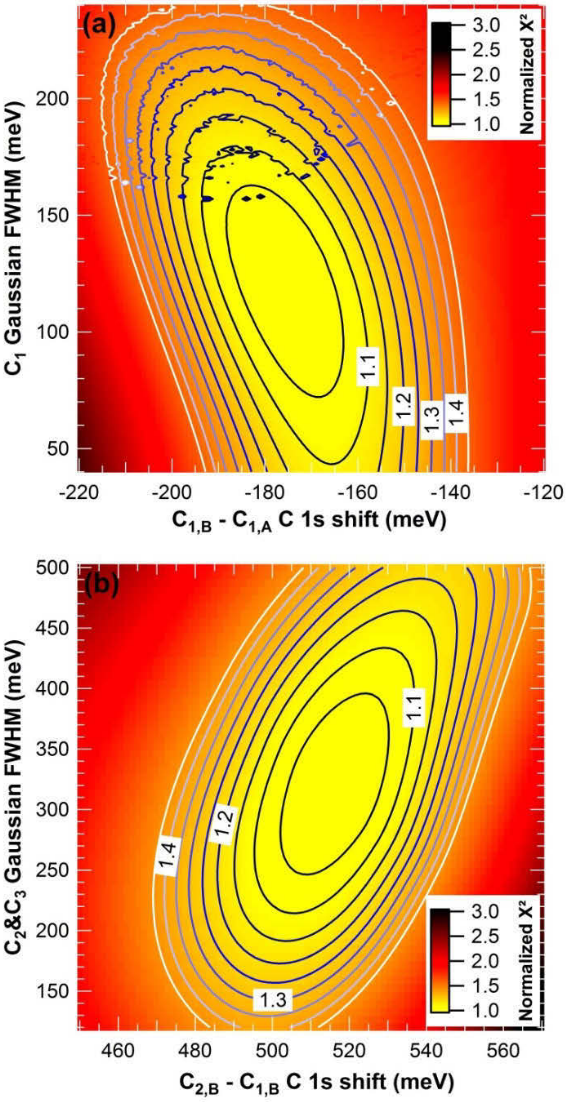

Figure 3.5: *Two-dimensional contour plots referred to the fit of C 1s core-level spectrum (0.11 ML carbon coverage) measured at hν=400 eV and in normal emission. The plots show the normalized chi square* χ^2 / χ^2_{MIN} *as a function of (a) Gaussian FWHM of monomers* C_1 *versus C 1s core level shift between monomers adsorbed in FCC and HCP three-fold sites and (b) Gaussian FWHM of dimers* C_2 *and trimers* C_3 *versus core level shift between dimers* C_2 *and monomers adsorbed in HCP three-fold sites.*

The same procedure was applied for the analysis of the C 1s spectrum acquired at higher coverage (0.32 ML), shown in Fig. 3.4. However in this case it was necessary to take into account also larger clusters, namely tetramers and pentamers, to correctly describe the experimental data. This was particularly important for the high binding energy shoulder at about 284.7 eV, that according to the DFT calculations can only be justified by assuming that the C_4 and C_5 species are present on the surface. The first step in the analysis of this spectrum was to introduce only one type of tetramer or pentamer at a time with a free Gaussian $G_{4,5}$ component, still keeping L and α at the value found for the lower coverage spectrum. The best agreement was achieved by including tetramers formed by $C_{4,H}$, $C_{4,L}$, $C_{4,M}$, $C_{4,N}$. Only in the final step a new species was added in order to minimize the χ^2: pentamers with C atoms arranged in linear fashion (top structure in Fig. 3.3-Pentamers) were those providing the lowest χ^2. While it is not possible to draw a clear cut picture about the concentration of the different C_4 and C_5 species, these results unambiguosly show that the 0.32 ML coverage structure cannot be described by including just monomers, dimers and trimers, as was the case for the lowest coverage spectrum. Owing to this behaviour and to the results of the Ir $4f_{7/2}$ analysis described above, we did not fit the 0.77 ML spectrum, shown in Fig. 3.1. Nevertheless this spectrum is consistent with the theoretical findings, as it displays an increased spectral intensity towards high BEs, were it is expected to have, besides the C dimers at 284.8 eV, also larger C clusters.

3.5.4 Origin of carbon monomers and dimers

The analysis of the coverage of the different species obtained after low temperature deposition gives interesting information about the growth of graphene. As reported in Table 3.2 the deposition of 0.11 ML at T=80 K results in the formation of 0.037, 0.021 and 0.040 ML of monomers HCP, monomers FCC and dimers, with 0.016 ML of trimers. We compared these results with those obtained using a random deposition model, in which C atoms are randomly distributed on the (111) surface, with the possibility to occupy with equal probability HCP and FCC three-fold sites and with the assumption that, when sitting in nearest-neighbour three-fold sites, they form a dimer. Besides the strong preference for the occupation of HCP sites if compared with FCC sites, in agreement with the theoretical findings, the main difference between experimental and theoretical results is found in the relative populations of dimers and monomers. In fact the experimental occupation of C atoms in dimer configuration (35 %) is much larger than the value obtained with the random deposition model calculation (13.5 %). This discrepancy can be explained as due to (i) diffusion of energetic C adatoms on the surface (effect not included in the random deposition model) and formation of dimers already at low temperature or (ii) deposition of C dimers on the surface directly originating from the graphite rod in the sublimation process. The first hypothesis can be disregarded since the barrier for the formation of dimers from monomers is large (1.29 eV) and, most of all, because C dimers are energetically unfavored with respect to C monomers by 0.68 eV. In order to support the second hypothesis about the sublimation of different C species, Nudged Elastic Band (NEB) theoretical calculations were performed to determine the minimum energy paths for carbon sublimation on graphite with different initial state geometries. In particular a graphite surface showing both zig-zag (Fig. 3.6(a)) and armchair monoatomic step edges (Fig. 3.6(b)), was considered in the calculation. These step edges have been experimentally found in scanning tunneling microscopy measurements on highly oriented pyrolytic graphite [58]. In these defective sites the C atoms have to break a smaller number of bonds with respect to the sp^2 configuration. For both configurations a monomer and a dimer was removed and the energy barrier of the process was calculated. It is clear that the detachment mechanism showing the lowest barrier ($E_{barrier}$= 8.36 eV) is the removal of a dimer from a zig-zag edge. These results are in agreement with what was observed experimentally, for instance in high temperature transmission electron microscopy measurements [59]. While it is possible that several other local defective configurations are present on the graphite rod surface, these results suggest that dimers can be directly deposited by means of sublimation from graphite, which represents therefore the ideal source for the study of their properties.

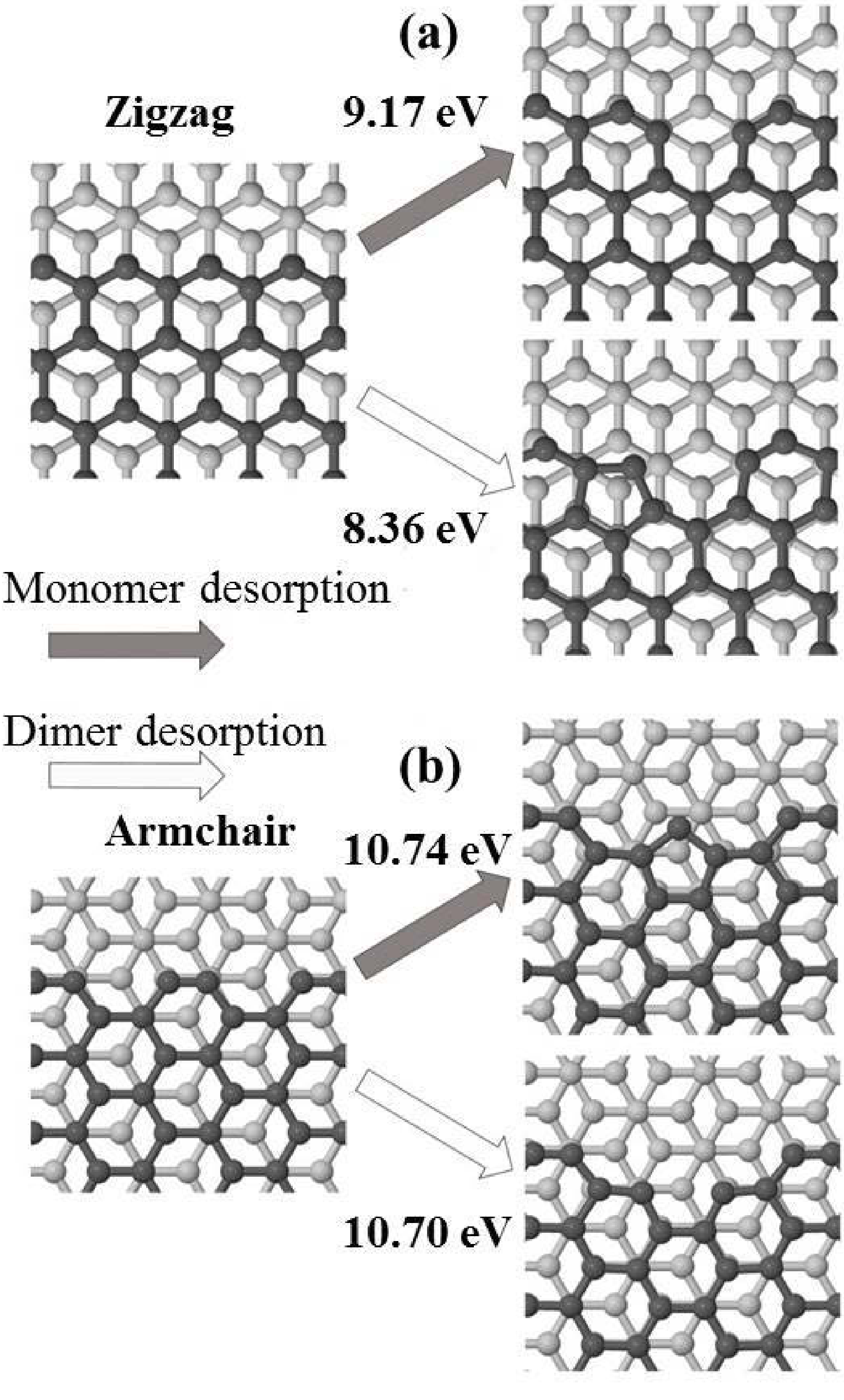

Figure 3.6: *Initial (left) and final (right) geometrical configurations in NEB calculations for the sublimation of carbon monomers (dark arrow) and dimers (white arrow) from zigzag (a) and armchair (b) graphite edges. Corresponding energy barriers are also reported.*

3.5.5 Graphene growth at high-temperature by means of chemical vapour deposition

In order to obtain information about the different C species which are present during the CVD growth, we exploited the snap-shot fast-XPS operation mode, in which the evolution of the C 1s core level is monitored in real time while dosing ethylene on Ir(111) at T=820 K, by using a supersonic beam of C_2H_4 molecules.

Figure 3.7(a) shows a two-dimensional plot of the time-lapsed C 1s spectra, with the photoemission intensity being represented as a density plot in gray-scale, ranging from low (black) to high (white). As previously found with temperature programmed growth experiments [44] the C 1s intensity is centered at around 284.1 eV and can be ascribed to C atoms forming small graphene islands growing with a very high surface density . The variation of the BE is due to the modified coupling of the C layers from the Ir substrate with increasing size of the nucleating graphene islands. The most interesting feature which dominates at the beginning of the growth process is a low binding energy C 1s component centered at 283.35 eV. Indeed (as shown by the selected uptake spectra in Fig. 3.7 (b)), while for large exposure the C 1s spectrum can be fitted with just three components - one due to the atoms at the center of the clusters, the others either to atoms at the periphery of the Gr clusters bound to 2 C atoms (BE=283.7 eV), or to C atoms bound to 3 C atoms and directly bound to the periphery (BE=284.4 eV) - in the very low coverage range a small component has to be included at the same BE found for the monomer species to obtain a proper fit of the experimental data. This peak, growing in intensity up to a maximum coverage of 0.08 ML, slowly disappears with increasing the ethylene exposure. This coverage can be compared with the C adatoms concentration needed to nucleate graphene on Ru(0001) at 940 K as reported in electron reflectivity measurements [13]. Besides the use of C 1s BE as a fingerprint of the presence of monomers on the surface, a further proof of the assignment of the low binding energy component in Fig. 3.7 (b) to monomers comes from the plot of the monomers coverage as a function of the carbon coverage in the graphene clusters (see Fig. 3.8), which can be simply calculated by summing the intensity of three components which are assigned to the different C species forming the small graphene flakes. The plot clearly shows that above a critical coverage the monomers coverage diminishes with a linear behavior, which is consistent with the density of monomers depending on the free surface area, *i.e.* the portion of the Ir surface which is not covered by graphene clusters. It is therefore the portion of clean Ir(111) surface which determines the density of monomers diffusing on the surface before attaching to the edges of the C clusters. These results suggest therefore that a C lattice gas is present also in the early stage of graphene growth on Ir(111) by means of C_2H_4 CVD.

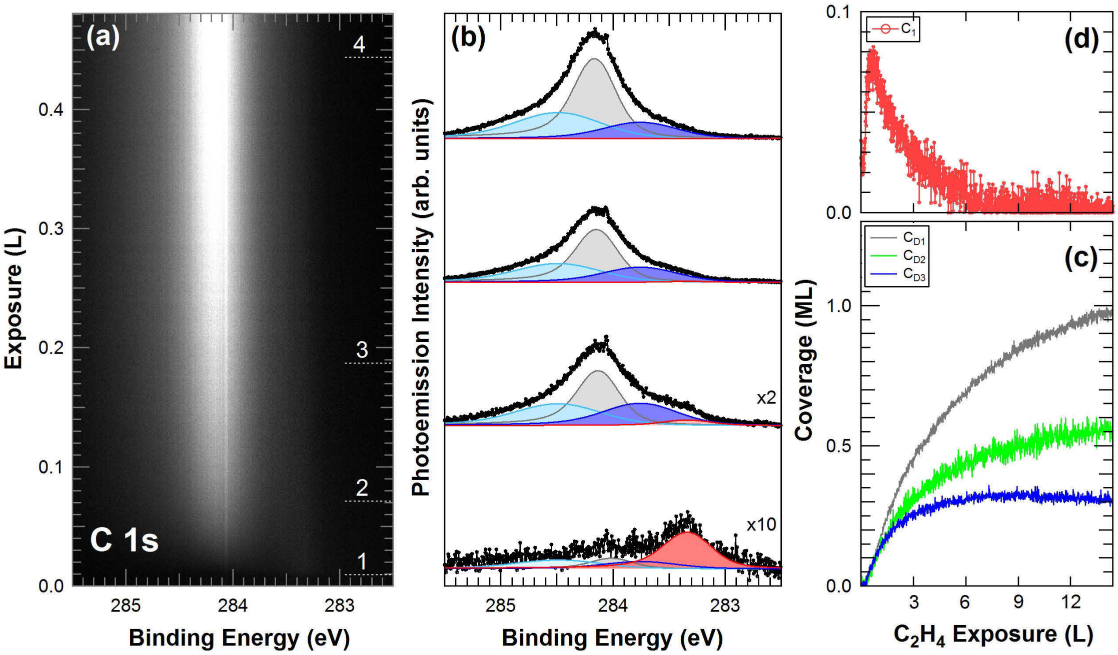

Figure 3.7: *Evolution of C 1s spectra during ethylene uptake at T= 820 K (hv=400 eV). (a) Coverage-dependent C 1s core-level spectra (about 1250 spectra) shown as a two-dimensional intensity plot. (b) Deconvoluted C 1s components from selected spectra of the uptake (numbered from 1 to 4 in (a)). (c) Evolution of the C coverage of the different species: C atoms at the center of the graphene clusters* C_{D1} *(gray), atoms at the periphery of the clusters bound to 2 C atoms* C_{D2} *(green), and* sp^2 *C atoms directly bound to the periphery of the clusters* C_{D3} *(blue). (d) Evolution of the intensity of* C_1 *(red) components representing monomers coverage.*

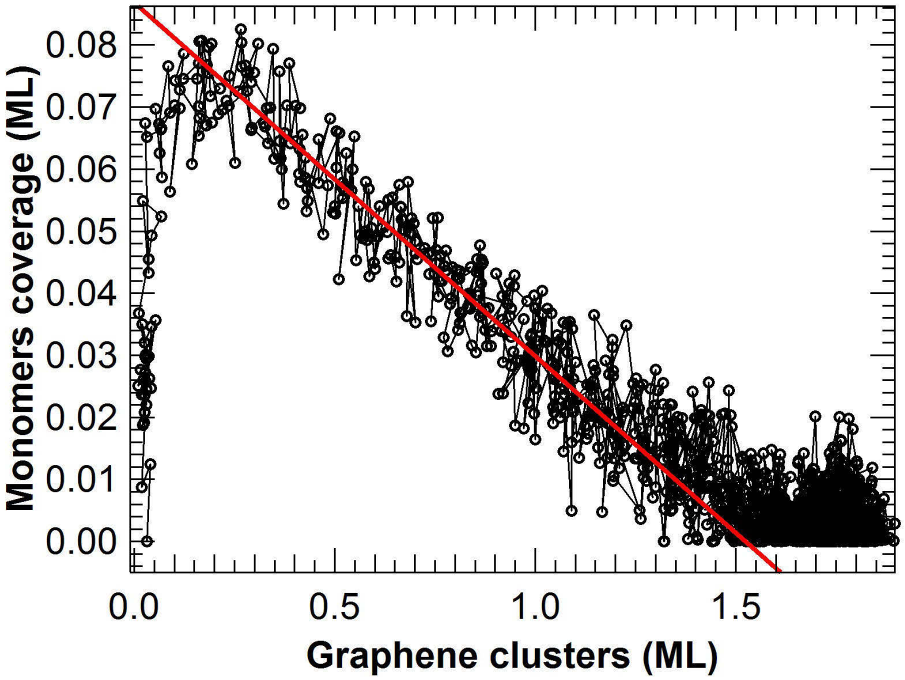

Figure 3.8: *Evolution of the population of C monomers as a function of the C coverage corresponding to graphene clusters during ethylene uptake at T=820 K. The coverage was calculated by summing the intensity of the three components* C_{D1}*,* C_{D2} *and* C_{D3} *in Fig. 3.7 (b).*

3.6 Carbon deposition at high temperature

The knowledge acquired in the low temperature deposition experiments was used to understand the process of mono and multi-layer graphene formation at high temperature. One of the main goals of this project is indeed the understanding of the growth mechanism of graphene layers produced using carbon molecular beam epitaxy and the comparison with other well established methods, such as chemical vapour deposition. The solid state carbon source was then used to deposit C atoms and dimers on Ir(111) at a temperature of 1200 K which is known, from previous CVD experiments, to result in the formation of a high-quality graphene layer.

Figure 3.9 (a) shows the sequence of high resolution C 1s core level spectra measured *in situ* during C deposition. At the beginning of the uptake a single component A at 284.15 eV binding energy is detected. With increasing C coverage a second component B appears at higher binding energy (284.35 eV), while the spectral weight of the low BE component (A) decreases. This spectral series can be compared with the one measured in graphene CVD growth at the same temperature, which is shown in Fig. 3.9 (b). As previously reported, in the latter case only a single component can be detected throughout the whole experiment, at the same binding energy of the A peak revealed in (a). This trend suggests that, while in the first stages of the growth the two methods produce similar C species, another non-equivalent C species appears at higher coverages when depositing carbon using molecular beam deposition.

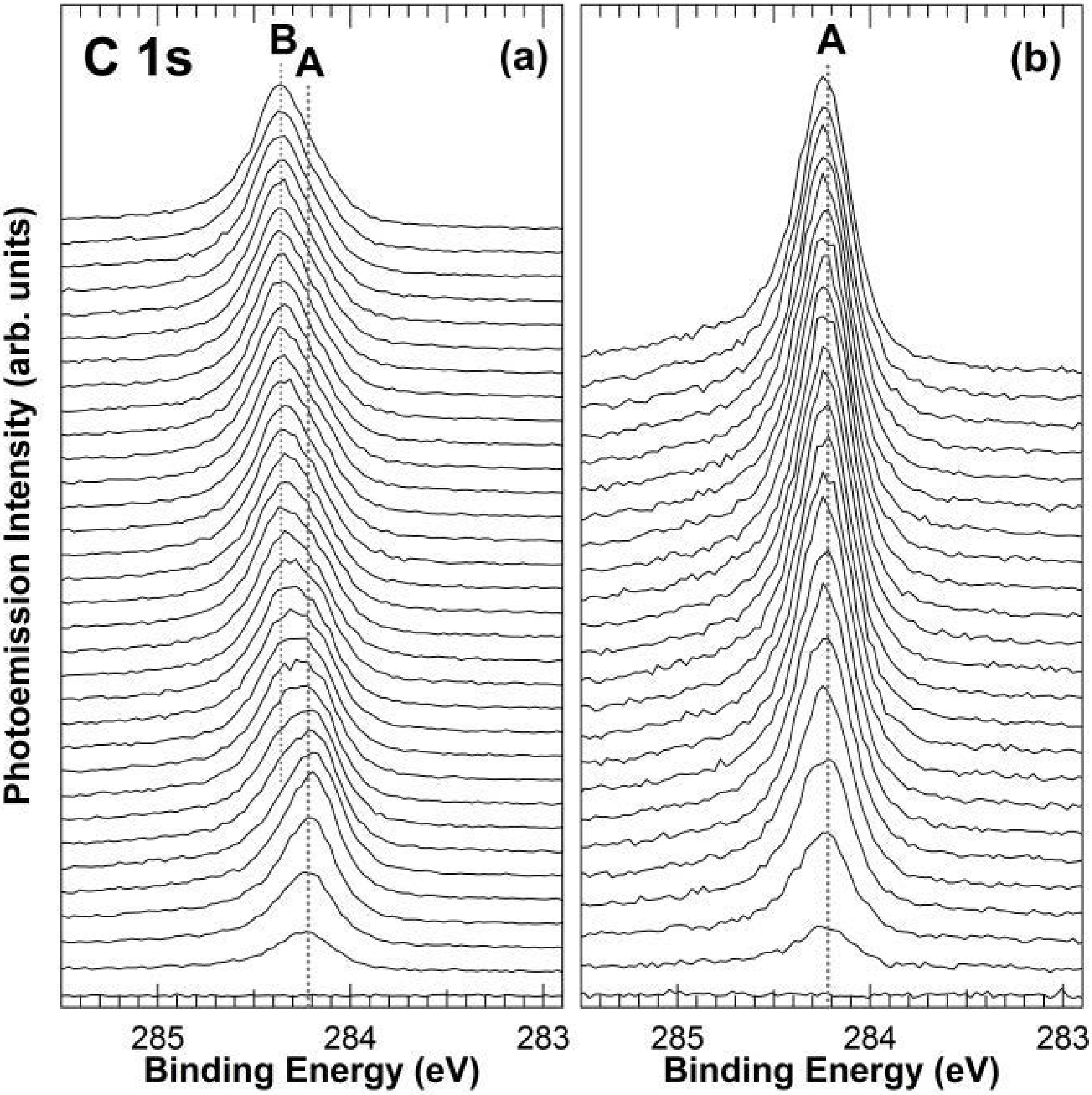

Figure 3.9: *The sequence of high resolution C 1s core level spectra measured in situ during (a) C deposition and (b) CVD growth at T= 1200 K.*

The modification in the C 1s spectral lineshape can be also appreciated in Fig. 3.10 (a) where the two-dimensional plot of the time-lapsed C 1s spectra is reported, with the photoemission intensity being represented as a density plot in grayscale, ranging from low (black) to high (white). In order to quantitatively determine the evolution of the different species at different C coverages the C 1s spectra was fitted in two steps. The low-coverage spectra were analysed first, using a single component (orange peak-Fig. 3.10 (b)): a good fit was obtained using a DS lineshape similar to the one used to fit the spectrum acquired at room temperature corresponding to a complete graphene layer on Ir(111), as discussed in Section 3.5.1 (L=200 meV, G=180 meV, α=0.155). The main difference is a larger Gaussian width, that can be explained as due to phonon-induced broadening effects because of the high temperature. This single component was sufficient to properly describe the spectrum (as demonstrated by low fitting residuals without an appreciable modulation) up to a coverage of 2.4 ML, corresponding to a full ML of graphene on the Ir(111) surface.

A new component B (red peak) was included at higher binding energy for fitting the high-coverage part of the uptake in order to properly describe the C 1s spectrum. This peak has a Lorentzian width of 213 meV, a Gaussian width of 150 meV and an asymmetry parameter of 0.046. The evolution of the two different components as a function of the deposition time can be appreciated in Fig. 3.10 (b), where the deconvoluted components are reported together with selected C 1s spectra. The reduction of the intensity of the A component clearly appears in Fig. 3.10 (c), where the intensities of the A and B components are plotted as a function C exposure. It is interesting to note that the growth of the B peak starts exactly after the A component has reached its maximum. The evolution of the two components suggests that the new B species could originate from second- and multi-layer graphene formed on top of the first monolayer graphene: the photoemission intensity decrease of the A components is indeed explained as due to the increased screening of the photoemission signal from the first carbon layer exerted by the additional layers of carbon atoms which are formed above it.

To achieve a quantitative assessment of the total Carbon coverage deposited using the carbon source one has to consider the screening effect both for the Ir $4f_{7/2}$ and C 1s levels by each layer of graphene due to the limited mean free path of the photoelectrons at the kinetic energy considered (115 eV). For the case of the C 1s, it is important to consider that not only the A component is screened by the 2^{nd} and

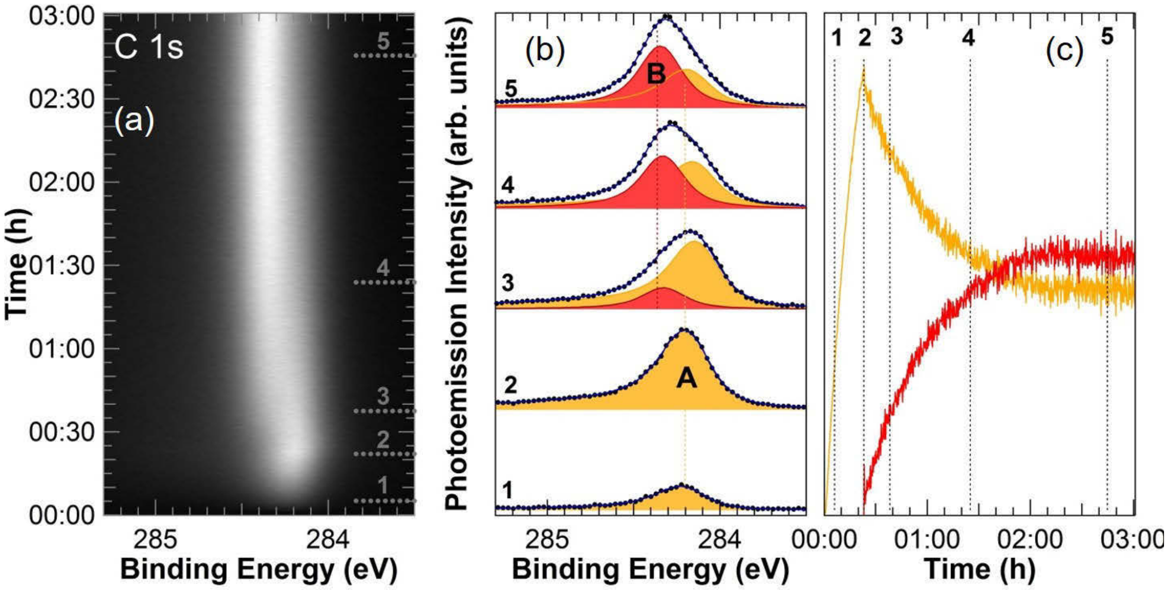

Figure 3.10: *(a) The two-dimensional plot of the time-lapsed C 1s spectra. (b) Plot of HR spectra at different deposition time (dotted-lines)* together with the evolution of the two different components (in color). (c) The intensity evolution of A and B components plotted versus carbon source exposure.

further layers (producing the B component), but also the total intensity of component B is given by the sum of the contributions of each additional layer (if more than one), each one screened by the layers lying above it. This contribution, however, cannot be simply modelled since it requires the knowledge of the growth method of the extra layers and the average size of these islands. For this reason, the number m of the further layers was calculated by evaluating their attenuation on the first layer, which can be modelled as:

$$\frac{I_A}{I_{A,MAX}} = \alpha^m \tag{3.2}$$

where α is the attenuation by a single C layer and

$$m = \frac{\theta_B}{2.47} \tag{3.3}$$

is the number of layers not in contact with the metallic surface (2^{nd} and further).

In order to quantify α and m, we measured the effect of the screening by a full monolayer of graphene on the Ir $4f_{7/2}$ core level in an experiment where the photon energy was tuned in such a way that the photoelectron kinetic energy was the same as in the excitation of the C 1s core electrons. In fact, the mean free path of electrons depends on its kinetic energy through the universal IMFP curve as explained in chapter 2.

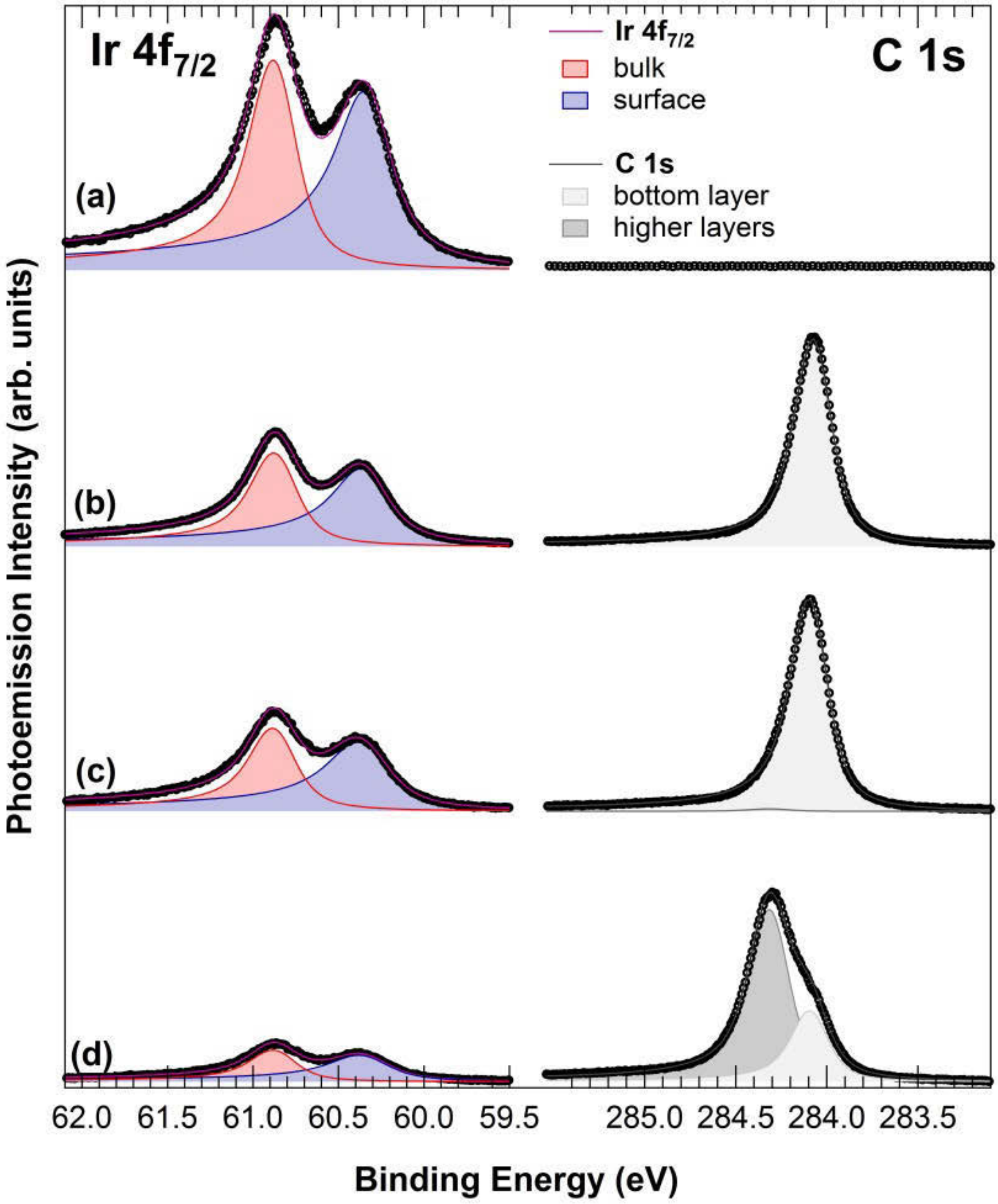

Figure 3.11: *Ir 4$f_{7/2}$ and C 1s intensity signal : (a) of clean sample; (b) after deposition of 1 ML graphene by CVD; (c) after deposition of 1 ML graphene by C source; (d)after deposition of multi layers graphene by C source. The spectra were shifted in the vertical scale for clarity.*

In particular, we evaluated the attenuation of the Ir $4f_7/2$ signal by single and multi-layer graphene, as shown in the left panel of Fig. 3.11. The signal after the growth of a full ML of graphene via CVD (b) is attenuated with respect to the signal of the clean surface (a) by a factor 0.43, which therefore corresponds to the value of α:

$$\frac{I_{Ir}}{I_{Ir,0}} = \alpha^n \tag{3.4}$$

where $n = m+1$ is the total number of GR layers, that in this case is 1.

It is interesting to notice that this is the same attenuation that is obtained from the growth using the C source, when the second component starts to appear (Fig. 3.11 (c) and point 2 of the uptake in Fig. 3.10 (b). Finally, the attenuation of the Ir $4f_{7/2}$ signal at the end of the experiment is 0.16: by applying the same formula, this yields n=2.23, corresponding to a total C coverage of 5.50 ML.

The right part of Fig. 3.11 shows instead the photoemission intensities of the A and B C 1s components in the same systems. At (c), component A has the same intensity as the one obtained in the CVD experiment (b), whereas component B is just 0.01 times as intense, whereas at (d) component A has decreased to 0.35 times its original intensity, while the intensity of B is 0.86 times that of the full monolayer graphene at (b).

An important observation is that the ratio between A and B components in the C 1s spectra taken at high temperature (as seen in Fig. 3.10) does not correspond to the one obtained from measurements at room temperature (fig. 3.11). This can be explained in terms of a reduced mean free path which could be attributed to enhanced electron-phonon scattering at high temperature. Therefore, in order to calculate the correct C coverage for the uptake experiment presented in Fig. 3.10, the following procedure has been applied. As long as a single component was present, the coverage was considered proportional to the photoemission intensity. For the part of the experiment where the second component was present, the coverage of the first component was fixed to the maximum value it had reached. The value of α_{1200K} at T=1200 K was obtained from the ratio of the A component of the C 1s spectrum between the last points and its maximum value, by employing the value m=n-1=1.23 obtained from the room temperature measurements. Finally, the ratio of the intensity of A with respect to its real coverage was used to quantify the number m of C layers covering it.

Figure 3.12 compares the evolution of the C coverage in the uptakes performed at the same temperature using the carbon MBE and CVD with ethylene (see

Fig. 3.12 (a)). In order to be able to compare these two different methods, it was necessary first of all to correctly align the reaction coordinate for the two experiments, namely the C flux on the sample and the exposure of the surface to the gas precursor, respectively. This was achieved by calculating an effective exposure coordinate for the carbon deposition experiment, obtained by multiplying the time coordinate of the experiment by a factor in order to obtain the overlap of the C 1s photoemission signals in the two uptakes at the early stage of the graphene growth, by matching the first derivatives of the intensities. This strategy is based on the approximation that at the early stage of graphene nucleation (*i.e.* in the very low coverage regime, <0.1 ML) the change in the coverage depends mainly on the C supply rate (either from C_2H_4 molecules or from monomers/dimers originated by the source) and not by the specific structures present on the surface. The two curves corresponding to the A peak, shown in Fig. 3.12 (a) (blue-for ethylene uptake, orange for C deposition), reach the same maximum intensity, which corresponds to 2.47 ML. The main differences in the coverage evolution can be appreciated starting from 1 Langmuir, where the slope of the curve corresponding to the CVD growth experiment is clearly decreasing with respect to the carbon MBE experiment, as highlighted in the zoom shown in Fig. 3.12(b). This suggests that the adsorption rate with the carbon source is larger than in the case of CVD when large graphene island are already formed on the surface, and becomes even larger when the saturation is approached.

Finally, Fig. 3.12(c) displays the C coverage of each component and the total coverage evolution during the experiment. As can be seen in the graph, this value reaches saturation after about 30 L effective dose. This fact can be explained by the fact that the extra C layers are growing not on the top of the first GR layer, but on the substrate below, as already observed in previous LEEM experiments [60]: as further layers grow, it becomes increasingly difficult for the C atoms to intercalate and reach the surface, which is required to continue the growth.

Another interesting result obtained in the carbon MBE experiment can be appreciated in Fig. 3.13 (a), where the core level binding energies of the A and B components measured during the high temperature uptake (T=1200 K). At the end of the uptake, when 2.23 layers (*i.e.* 5.50 MLs of C atoms) are present, the binding energy difference results to be about 150 meV, as shown in the top spectrum of Fig. 3.13(b).

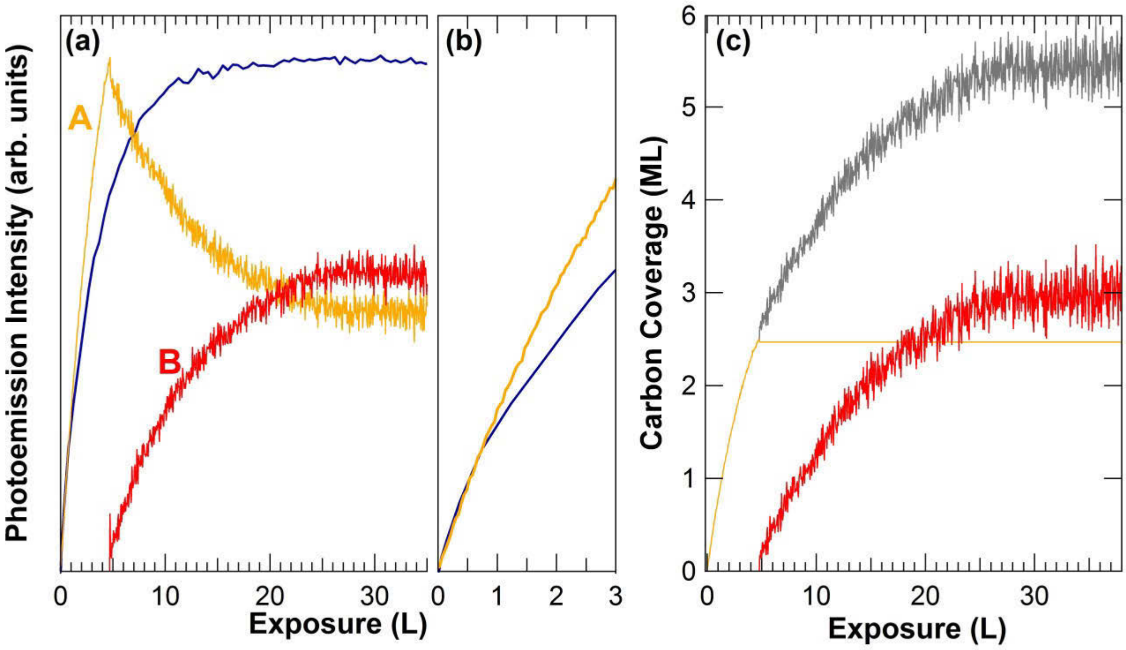

Figure 3.12: *(a) Evolution of C coverage using the carbon source (orange and red colors) and CVD with ethylene (blue color). (b) A zoom-in to highlight the difference of the growth rate between the two sources. (c) C coverage evolution of each component and of the total intensity (grey color) as a function of exposure.*

However, when the Ir(111) crystal is at room temperature, the two components, while keeping a similar spectral weight ratio, are characterized by a quite different core level shift, which amounts to 210 meV. This change can be explained as due to the different thermal expansion of monolayer and free-standing graphene. Because of the weak van der Waals coupling between different C layers the topmost graphene layers can be considered as free-standing, while the first C layer is directly interacting with the graphene substrate. Therefore its thermal expansion is driven by the positive thermal expansion of the Ir substrate underneath, while for the upper and decoupled layers the thermal expansion is expected to be negative, as for free-standing graphene. For a quantitative evaluation we compared our experimental findings with the expected C 1s core level shift for epitaxial and freestanding graphene, calculated by means of DFT and molecular dynamics simulations and reported in Ref. [61]. By increasing the temperature from 300 K to 1000 K the differences in the calculated C 1s core levels shift amounts to 90 meV, which is in quite good agreement with our measured changes of +150 meV. Small discrepancy can be explained as due to the coupling of graphene first layer and the new carbon layers above it.

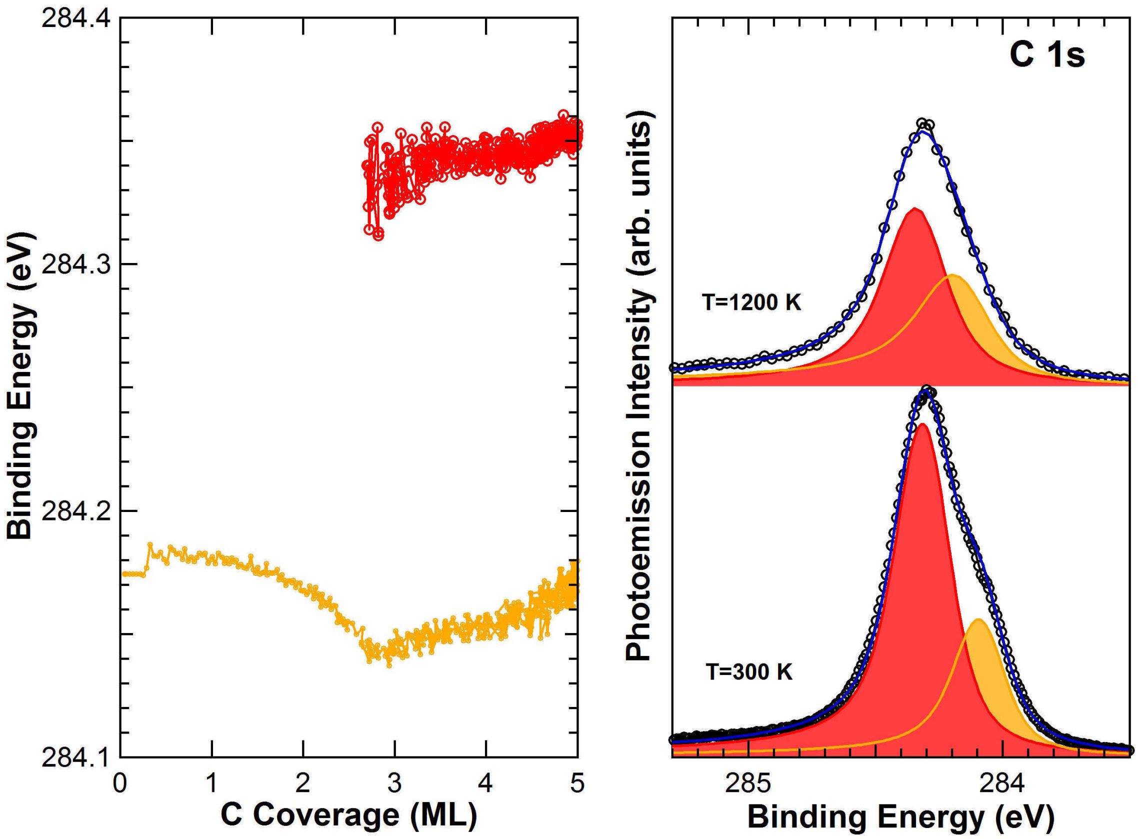

Figure 3.13: *(a) Evolution of the core level BE of A and B components from Fig.3.12 measured at 1200 K. (b) HR spectra to highlight the CLS difference of the same components at 1200 K and 300 K.*

The system was further characterized by acquiring low energy diffraction images corresponding to the different systems, as reported in Fig. 3.14. The Gr monolayer prepared by CVD shows the typical diffraction pattern with the presence of several spots aligned with those of the Ir(111) surface (Fig. 3.14 (a)) due to the formation of the long-range order periodicity of the moiré superlattice. Interestingly, the image corresponding to the multilayer formation (Fig. 3.14 (b)) still shows the same moiré spots, even though the background intensity has increased. This is a further proof that the growth of the new C layers takes place by migration of C monomers/dimers at the interface between the monolayer graphene and the Ir substrate, and not above graphene. In the latter case one would expect the formation of rotational domains and the appearance of ring-like diffraction features as in the case of highly oriented pyrolytic graphite.

The information obtained by the high-energy resolution XPS and LEED experiments allows us to make important comparison between the process of graphene

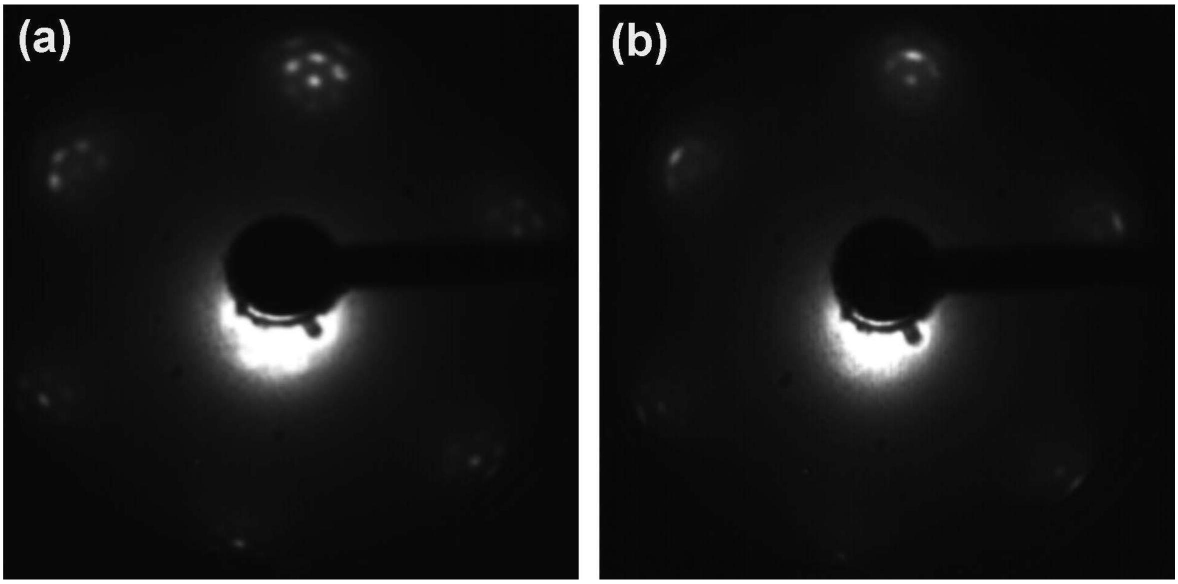

Figure 3.14: *LEED image of graphene to show the moiré pattern after (a) 1 ML graphene prepared by CVD and (b) after multi layer of graphene prepared with the C source.*

growth on Ir(111) using CVD and MBE. While in the first case the growth is limited by the amount of Ir clean surface area, which acts as the catalyst for the dissociation of hydrocarbon molecules, in the second approach we demonstrated that it is possible to grow more than one C graphitic layers. The difference in the uptake behavior, in particular the higher C rate of adsorption achieved with the C source is interpreted as due to the possibility of C monomers and dimers to stick not only on the bare Ir surface, but also on the already formed graphene monolayer. In this case, because of the low energetic barriers, monomers and dimers can rapidly diffuse on the Gr surface until they reach the periphery of a Gr island, where they attach to the edges and contribute to the island growth. It is important to note that the slope of the sub-monolayer uptake curve in the MBE experiment (A component in Fig. 3.12 (a) and (b)) does not show a linear behavior. This implies that, besides the surface diffusion, part of the C monomers and dimers can also desorb from the Gr layer. In order to prove this, further DFT calculations by the group led by Prof. L. Kantorovich at King's College London, UK are at the moment under progress. The possibility to reach almost a saturation stage using the carbon source can be explained also by considering the desorption probability of monomers and dimers. As soon as the Gr defects (mono- and di-vacancies, grain boundaries, etc) are filled by the C atoms, the process of intercalation of C atoms at the graphene-Ir(111) interface is inhibited and the growth of further layer is therefore blocked. Infact at the high growth temperature the probability of C spieces to go back into the gas phase via a desorption mechanism become larger and larger with decreasing the density of graphene areas where the C atoms could penetrate at the interface.

3.7 Conclusions

By combining high resolution XPS data with theoretical calculations we have shown that the C 1s core level BE can be used as a fingerprint for C monomers in two systems where either small C clusters (dimers, trimers, etc) or graphene nanoislands are present together.

In particular, we have shown that the low temperature deposition of carbon atoms using a solid carbon source results in a distribution of C clusters whose sizes depend on the surface density of carbon atoms and that high resolution core level spectroscopy can provide quantitative results on the relative concentration of the different species and, for the case of monomers, even on their adsorption sites. These measurements allowed us to conclude that the species which are present on the surface depend not only on the way they interact on the surface, but strongly depend on the dynamics by which they are generated by the C source. Based on the interpretation of the low temperature data, the presence of a carbon lattice gas during ethylene uptake performed at 820 K was demonstrated, in particular in the early stages of the graphene growth, when a significant density of monomers (C 1s component at 283.35 eV) was detected already before the nucleation process started. We believe therefore that C 1s high resolution core level spectroscopy can provide very useful information about the role of monomers and dimers during the growth of graphene on different metal surfaces.

Bibliography

[1] A.B. Preobajenski, M.L. Ng, A.S. Vinogradov and N. Mårtensson, *Controlling graphene corrugation on lattice-mismatched substrates*, Phys. Rev. B **78**, 073401 (2008).

[2] I. Pletikosič, M. Kralj, R. Brako, J. Coraux, A.T. N'Diaye, C. Busse, and T. Michely, *Dirac Cones and Minigaps for Graphene on Ir(111)*, Phys. Rev. Lett. **102**, 056808 (2009).

[3] A.T. N'Diaye, J. Coraux, T.N. Plasa and T. Michely, *Structure of epitaxial graphene on Ir(111)*, New J. Phys. **10**, 043033 (2008).

[4] J. Coraux, A.T. N'Diaye, C. Busse and T. Michely, *Structural Coherency of Graphene on Ir(111)*, Nano Lett. **8**, 565-570 (2008).

[5] I. Hernández-Rodríguez, J.M. García, J.A. Martín-Gago, P.L. de Andrés, and J. Méndez, *Graphene growth on Pt(111) and Au(111) using a MBE carbon solid-source*, Diam. and Rel. Mat. **57**, 58-62 (2015).

[6] B. Kiraly, E.V. Iski, A.J. Mannix, B.L. Fisher, M.C. Hersam, and N.P. Guisinger, *Solid-source growth and atomic-scale characterization of graphene on Ag(111)*, Nat. Commun. **4**, 2804 (2013).

[7] E. Moreau, F.J. Ferrer, D. Vignaud, S. Godey and X. Wallart, *Graphene growth by molecular beam epitaxy using a solid carbon source*, Phys. Stat. Solidi A **207**, 300-303 (2010).

[8] J.C. Shelton, H.R. Patil, J.M. Blakely, *Equilibrium Segregation of Carbon to a Nickel (111) Surface-Surface Phase-Transition*, Surf. Sci. **43**, 493–520 (1974).

[9] S. Nie, A.L. Walter, N.C. Bartelt, E. Starodub, A. Bostwick, E. Rotenberg, and K.F. McCarty, *Growth from Below: Grahene Bilayers on Ir(111)*, ACS Nano **5**, 2298-2306 (2011).

[10] P. Wu, W. Zhang, Z. Li, and J. Yang, *Mechanism of Graphene Growth on Metal Surfaces: Theoretical Perspectives*, Small **10**, 2136-2150 (2014).

[11] H. Tetlow, A.J. Posthuma de Boer, I.J. Ford, D.D. Vvdensky, J. Coraux, L. Kantarovich, *Growth of epitaxial graphene: Theory and experiment*, Phys. Rep. **542**, 195-295 (2014).

[12] C.M. Seah, S.P. Chai, A.R. Mohamed, *Mechanisms of graphene growth by chemical vapour deposition on transition metals*, Carbon **70**, 1 (2014).

[13] E. Loginova, N.C. Bartelt, P.J. Feibelman, and K.F. McCarty, *Factors influencing graphene growth on metals surfaces*, New J. Phys. **11**, 063046 (2009).

[14] E. Loginova, N.C. Bartelt, P.J. Feibelman, and K.F. McCarty, *Evidence for graphene growth by C cluster attachment*, New J. Phys. **10**, 093026 (2008).

[15] P. Wu, H. Jiang, W. Zhang, Z. Li, Z. Hou, and J. Yang, *Lattice Mismatch Induced Nonlinear Growth of Graphene*, J. Am. Chem. Soc. **134**, 6045 (2012).

[16] O.V. Yazyev, Y.P. Chen, *Polycrystalline graphene and other two dimensional materials*, Nat. Nanotech. **9**, 755-767 (2014).

[17] S. Riikonen, A.V. Krasheninnikov, L. Halonen, and R.M. Nieminen, *Role of Stable and Mobile Carbon Adspecies in Copper-Promoted Graphene Growth*, J. Phys. Chem. C **116**, 5802-5809 (2012).

[18] T. Niu, M. Zhou, J. Zhang, Y. Feng, and W. Chen, *Growth Intermediates for CVD Graphene on Cu(111): Carbon Clusters and Defective Graphene*, J. Am. Chem. Soc. **135**, 8409 (2013).

[19] P. Wu, Y. Zhang, P. Cui, Z. Li, J. Yang, and Z. Zhang, *Carbon Dimers as the Dominant Feeding Species in Epitaxial Growth and Morphological Phase Transition of Graphene on Different Cu Substrates*, Phys. Rev. Lett. **114**, 216102 (2015).

[20] L. Zhong, J. Li, Y. Li, H. Lu, H. Du, L. Gan, C. Xu, S.W. Chiang, and F. Kang, *Unraveling the Influence of Metal Substrates on Graphene Nucleation from First-Principles Study*, J. Phys. Chem. C **120**, 23239-23245 (2016).

[21] H. Chen, W. Zhou, and Z. Zhang, *Contrasting Behaviour of Carbon Nucleation in the Initial Stages of Graphene Epitaxial Growth on Stepped Metal Surfaces*, Phys. Rev. Lett. **104**, 186101 (2010).

[22] M. Gao, Y.-F. Zhang, Z. Yang, *Growth mechanism and controllable synthesis of graphene on Cu-Ni alloy surface in the initial growth stages*, Phys. Lett. A **379**, 1361 (2015).

[23] L. Xu, Y. Jin, Z. Wu, Q. Yuan, Z. Jiang, Y. Ma, and W. Huang, *Transformation of Carbon Monomers and Dimers to Graphene Islands on Co(0001): Thermodynamics and Kinetics*, J. Phys. Chem. C **117**, 2952 (2013).

[24] L. Xu, Y. Ma, Z. Wu, B. Chen, Q. Yuan, and W. Huang, *A Photoemission Study of Ethylene Decomposition on a Co(0001) surface: Formation of Different Types of Carbon Species*, J. Phys. Chem. C **116**, 4167-4174 (2012).

[25] J. Li, E. Croiset, and L. Ricardez-Sandova, *Carbon clusters on the Ni(111) surface: a density functional theory study*, Phys. Chem. Chem. Phys. **16**, 2954 (2014).

[26] J. Gao, Q. Yuan, H. Hu, J. Zhao, and F. Ding, *Formation of Carbon Clusters in the Initial Stage of Chemical Vapor Deposition Graphene Growth on Ni(111) Surface*, J. Phys. Chem. C **115**, 17695-17703 (2011).

[27] F. Zhaoming, Y. Zhang, Z. Yang, *Growth mechanism and controllable synthesis of graphene on Cu-Ni alloy surface in the initial growth stages*, Phys. Lett. A **379**, 1361 (2015).

[28] A.J. Page, F. Ding, S. Irle, and K. Morokuma, *Insights into carbon nanotube and graphene formation mechanisms from molecular simulations: a review*, Rep. Prog. Phys. **78**, 036501 (2015).

[29] N.J. Long, C.K. Williams, *Metal Akynyl σ Complexes: Synthesis and Materials*, Angew. Chem. Int. Ed. **42**, 2586 (2003).

[30] V.W.-W. Yam, *Molecular Design of Transition Metal Alkynyl Complexes as Building Blocks for Luminescent Metal-Based Materials: Structural and Photophysical Aspects*, Accounts. Chem. Res. **35**, 555 (2002).

[31] M. Bianchi, D. Cassese, A. Cavallin, R. Comin, F. Orlando, L. Postregna, E. Golfetto, S. Lizzit, and A. Baraldi, *Clean and oxygen induced surface core level shift on Ir(111)*, New J. Phys. **11**, 063002 (2009).

[32] A. Baraldi, L. Rumiz, M. Moretuzzo, M. Barnaba, G. Comelli, S. Lizzit, G. Paolucci, R. Rosei, F. Buatier de Mongeot, and U. Valbusa, *A supersonic molecular beam for gas-surface interaction studies with synchrotron radiation*, J. Vac. Sci. Technol. B **20**, 683 (2002).

[33] S. Doniach, M.J. Šunjić, J. Phys. C: Solid State Phys. **3**, 285 (1970).

[34] J. Hutter, M. Iannuzzi, F. Schiffmann, and J. Vande Vondele, *CP2K: atomistic simulations of condensed matter system*, Wiley Interdisc. Rev.: Comput. Mol. Sci. **4**, 1759 (2014).

[35] J.P. Perdew, K. Burke, M. Ernzerhof, *Generalized Gradient Approximation Made Simple*, Phys. Rev. Lett. **77**, 3865 (1996).

[36] S. Goedecker, M. Teter, J. Hutter, *Separable Dual-Space Gaussian Pseudopotentials*, Phys. Rev. B **54**, 1703 (1996).

[37] J. Vande Vondele and J. Hutter, *Gaussian basis Sets for Accurate Calculations on Molecular Systems in Gas and Condensed Phases*, J. Chem. Phys. **127**, 114105 (2007).

[38] S. Grimme, J. Antony, S. Ehrlich, and H. Krieg, *A consistent and accurate ab initio parametrization of density functional dispersion correction (DFT-D) for the 94 elements H-Pu*, J. Chem. Phys. **132**, 154104 (2010).

[39] G. Kresse, and J. Furtmüller, *Efficiency of ab-initio total energy calculations for metals and semiconductors using a plane-wave basis set*, Comp. Mat. Sci. **6**, 15 (1996).

[40] G. Kresse, and J. Furtmüller, *Efficient iterative schemes for ab-initio total-energy calculations using a plane-wave basis set*, Phys. Rev. B **54**, 11169 (1996).

[41] G. Kresse, and J. Hafner, *Ab initio molecular-dynamics for liquid-metals*, Phys. Rev. B **47**, 558 (1993).

[42] L. Köhler, and G. Kresse, *Density functional study of CO on Rh(111)*, Phys. Rev. B **70**, 165405 (2004).

[43] J. Coraux, A.T. N'Diaye, M. Engler, C. Busse, D. Wall, N. Buckanie, F.-J. Meyer zu Heringdorf, R. van Gastel, B. Poelsema, and T. Michely, *Growth of graphene on Ir(111)*, New J. Phys. **11**, 023006 (2009).

[44] P. Lacovig, M. Pozzo, D. Alfè, P. Vilmercati, A. Baraldi, and S. Lizzit, *Growth of Dome-Shaped Carbon Nanoislands on Ir(111): The intermediate between Carbidic Clusters and Quasi-Free-Standing Graphene*, Phys. Rev. Lett. **103**, 166101 (2009).

[45] A.B. Preobrajenski, M.L. Ng, A.S. Vinogradov, and N. Mårtensson, *Controlling graphene corrugation on lattice mismatch substrate*, Phys. Rev. B **78**, 073401 (2008).

[46] F. Presel, N. Jabeen, M. Pozzo, D. Curcio, L. Omiciuolo, P. Lacovig, S. Lizit, D. Alfè, A. Baraldi, *Unravelling the roles of chemical composition and geometry for the graphene-metal interaction through C 1s core level spectroscopy*, Carbon **93**, 187 (2015).

[47] T. Susi, M. Kaukonen, P. Havu, M.P. Ljungberg, P. Ayala, and E.I. Kauppinen, *Core level binding energies of functionalized and defective graphene*, Beilstein, J. Nanotech. **5**, 121-132 (2014).

[48] A. Baraldi, *Structure and chemical reactivity of transition metal surfaces as probed by synchrotron radiation core level photoelectron spectroscopy*, J. Phys.: Condens. Matt. **20**, 093001 (2009).

[49] A. Baraldi, J. Cerdá, J.A. Martin-Gago, G. Commeli, S. Lizzit, G. Paolucci, R. Rosei, *Oxygen Induced Reconstruction of the Rh(100) Surface: General Tendency Towards Threefold Oxygen Adsorption Site on Rh Surfaces*, Phys. Rev. Lett. **82**, 4874 (1999).

[50] M.V. Ganduglia-Pirovano, M. Scheffler, A. Baraldi, S. Lizzit, G. Comelli, G. Paolucci, R. Rosei, *Oxygen-induced Rh 3d$_{5/2}$ surface core-level shifts on Rh(111)*, Phys. Rev. B **63**, 205415 (2001).

[51] S. Lizzit, A. Baraldi, A. Groso, K. Reuter, M.V. Ganduglia-Pirovano, C. Stampfl, M. Scheffler, M. Stichler, C. Keller, W. Wurth, D. Menzel, *Surface core-level shifts of clean and oxygen-covered Ru(0001)*, Phys. Rev. B **63**, 205419 (2001).

[52] A. Baraldi, S. Lizzit, G. Comelli, G. Paolucci, *Oxygen adsorption and ordering on Ru(10$\bar{1}$0)*, Phys. Rev. B **63**, 115410 (2001).

[53] L. Bianchettin, A. Baraldi, S. de Gironcoli, S. Lizzit, L. Petaccia, E. Vesselli, G. Comelli, R. Rosei, *Geometric and electronic structure of the N / Rh(100) system by core-level photoelectron spectroscopy: Experiment and theory*, Phys. Rev. B **74**, 045430 (2006).

[54] L. Bianchettin, A. Baraldi, E. Vesselli, S. de Gironcoli, S. Lizzit, L. Petaccia, G. Comelli, R. Rosei, *Experimental and theoretical surface core level shift study of the S-Rh (100) local environment*, J. Phys. Chem. C **111**, 4002 (2007).

[55] C.J. Weststrate, A. Baraldi, L. Rumiz, S. Lizzit , G. Comelli, R. Rosei, *A surface core-level shift study of hydrogen interaction with Rh(111)*, Surf. Sci. **486**, 566–568 (2004).

[56] H. Tetlow, J. Posthuma de Boer, I.J. Ford, D.D. Vvedensky, D. Curcio, L. Omiciuolo, S. Lizzit, A. Baraldi, and L. Kantorovitch, *Ethylene decomposition on Ir(111): Initial path to graphene formation*, Phys. Chem. Chem. Phys. **18**, 27897 (2016).

[57] E. Ferrari, L. Galli, E. Miniussi, M. Morri, M. Panighel, M. Ricci, P. Lacovig, S. Lizzit, and A. Baraldi, *Layer-dependent Debye temperature and thermal expansion of Ru(0001) by means of high-energy resolution core level photoelectron spectroscopy*, Phys. Rev. B **82**, 195420 (2010).

[58] Y. Niimi, T. Matsui, H. Kambara, K. Tagami, M. Tsukada, and H. Fukuyama, *Scanning tunneling microscopy and spectroscopy of the electronic local density of states of graphite surfaces near monoatomic step edges*, Phys. Rev. B **73**, 085421 (2006).

[59] J.Y. Huang, F. Ding, B.I. Yakobson, P Lu, L. Qi, and J. Li, *In situ observation of graphene sublimation and multi-layer edge reconstructions*, Proc. Natl. Acad. Sci. **106**, 10103–10108 (2009).

[60] S. Nie, A.L. Walter, N.C. Bartelt, E. Starodub, A. Bostwick, E. Rotenberg, and K.F. McCarty, *Growth from below: Graphene Bilayers on Ir(111)*, ACS Nano **5**, 2298-2306 (2011).

[61] M. Pozzo, D. Alfè, P. Lacovig, P. Hoffmann, S. Lizzit, and A. Baraldi, *Thermal Expansion of Supported and Freestanding Graphene: Lattice constant versus Interatomic Distance*, Phys. Rev. Lett. **106**, 135501 (2011).

Chapter 4

Temperature-driven graphene growth on Ag(111) using the solid carbon source

4.1 Introduction

The growth of graphene on metallic substrates has driven a huge research effort in the last years, aiming to unveil and describe the properties of these technologically relevant interfaces. Chemical Vapour Deposition (CVD) has been proved to be the most reliable and potentially scalable way to grow large graphene flakes on many metallic substrates. Such process exploits the capacity of some metal surfaces to catalyse the dissociation of hydrocarbon molecules and the formation of a graphene lattice [1, 2, 3].

However, this approach is not successful on noble metals, gold and silver, where no catalytic decomposition of hydrocarbons was ever detected. Some alternative solutions have been then developed, aiming to deposit graphene layers and graphene-based nanostructures on these metals such as irradiation of the metal surface with a high energy beam of hydrocarbon molecules [4], sputtering of carbon films [5] or evaporation and polymerisation of a tailored molecular precursor [6, 7, 8].

A promising approach to grow graphene on non-reactive metals is based on the dose of atomic carbon directly on the surface through an atomic carbon source. Such system has been employed to grow graphene layers on several substrates and it appears to work efficiently also on noble metal surfaces [9, 10, 11].

In this chapter are discussed the results obtained on the growth of graphene on a Ag(111) single crystal by evaporating carbon from the solid carbon source. Two different methods of growth were employed. First, we evaporated carbon on Ag while keeping the sample at high temperature (High Temperature Growth, HTG). In a second moment we tried to grow graphene by exposing the metal at RT to the C flux and then annealing at high temperature (Temperature Programmed Growth, TPG). In both cases high-resolution and fast XPS and NEXAFS provided information on the nature of the carbon bonds at the surface and on their orientation. Structural properties were investigated by means of LEED.

4.2 Experimental methods

The experiments were performed at the SuperESCA beamline of Elettra. The Ag(111) single crystal was cleaned in UHV by several cycles of Ar^+ sputtering (E_K =1 keV), followed by annealing to 820 K. The sample temperature was measured by means of two thermocouples spot-welded in close contact with it. The base pressure in the UHV chamber during the experiments was better than 10^{-10} mbar.

High-resolution XPS data and NEXAFS spectra were acquired by means of a Phoibos hemispherical electron energy analyzer, integrated with an in-house developed delay-line detector. The spectra of the C 1s and Ag 3d core levels were acquired by using a photon energy of $h\nu = 400$ eV and $h\nu = 480$ eV, respectively with overall energy resolution of the order of 50 meV and in normal emission conditions. Carbon deposition was performed in conditions similar to the ones used for the growth of graphene on Ir(111) with MBE described in chapter 3, with a carbon flux of $\sim 2 \times 10^{-3}$ ML/s with the ML now reffered to the Ag(111) surface atomic density. As usual, all the XPS spectra have been normalised by the number of scans and beam current and the binding energy scale was referred to the Fermi level of the Ag sample. The experimental data were fitted with a Doniach-Šunjić function [12] convoluted with a Gaussian distribution and a Shirley background. The C K-edge NEXAFS spectra were recorded in the Auger yield mode by revealing the photoelectrons at kinetic energy of 260 eV corresponding to the C-KLL transition. Angular dependent spectra were taken as a function of the angle θ between the photon beam (which was horizontally polarized) and the substrate plane. The angle θ was varied between 20° (grazing incidence) and 90° (normal incidence) by rotating the sample.

4.3 Results and discussion

4.3.1 High Temperature Growth (HTG)

The first deposition experiment was carried out by exposing the Ag(111) sample to the carbon source output while keeping it at 1000 K. This growth protocol was intended to reproduce the outcomes observed in earlier literature [10]. The evolution of the C 1s core level during the growth (Fig. 4.1) showed only a single component growing almost linearly during the whole exposure without reaching saturation.

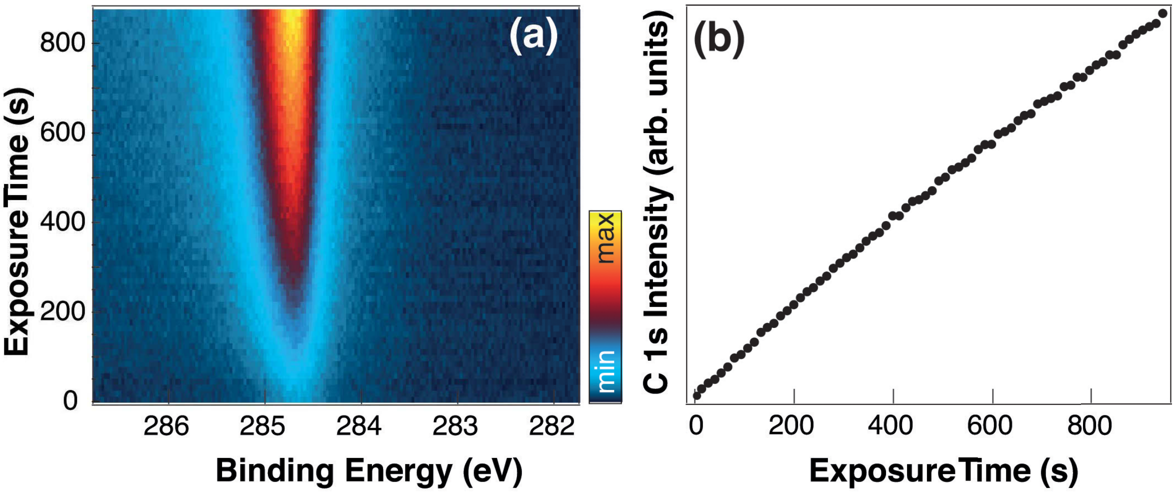

Figure 4.1: *(a) Time evolution during carbon uptake on Ag(111), with sample kept at 1000 K. (b) Intensity evolution of the C 1s peak during the uptake extracted from peak-fit analysis.*

The high-resolution C 1s core level spectrum (Fig. 4.2(a) acquired at RT after carbon deposition showed only a single component centered at 284.70 eV binding energy (BE) with best fit parameters of: L=0.3 eV, α=0.1, G=0.22 eV, resulting in a FWHM of the C 1s peak of $\sim$ 0.52 eV. This single peak can be associated to the growth of graphene on the metallic substrate. The relatively large shift of the position of the C 1s peak (ca. 600 meV when compared to the C 1s binding energy for the almost self-standing graphene/Ir(111) case [13] where a slight graphene p-doping is present [14]) could result from a charge transfer process from the metal to the graphene overlayer, similarly to what observed for other graphene/metal interfaces [3]. By considering that for weakly-interacting metals [15] a negative shift in the BE of the C 1s level is the footprint of a comparable shift of the Dirac cone, we infer that graphene on Ag(111) is relatively strongly n-doped. In panel 4.2(b) we show the Ag 3d core level acquired before and after the carbon deposition. The intensity of the signal after the carbon dose is attenuated by ca. 20% with respect to the clean surface.

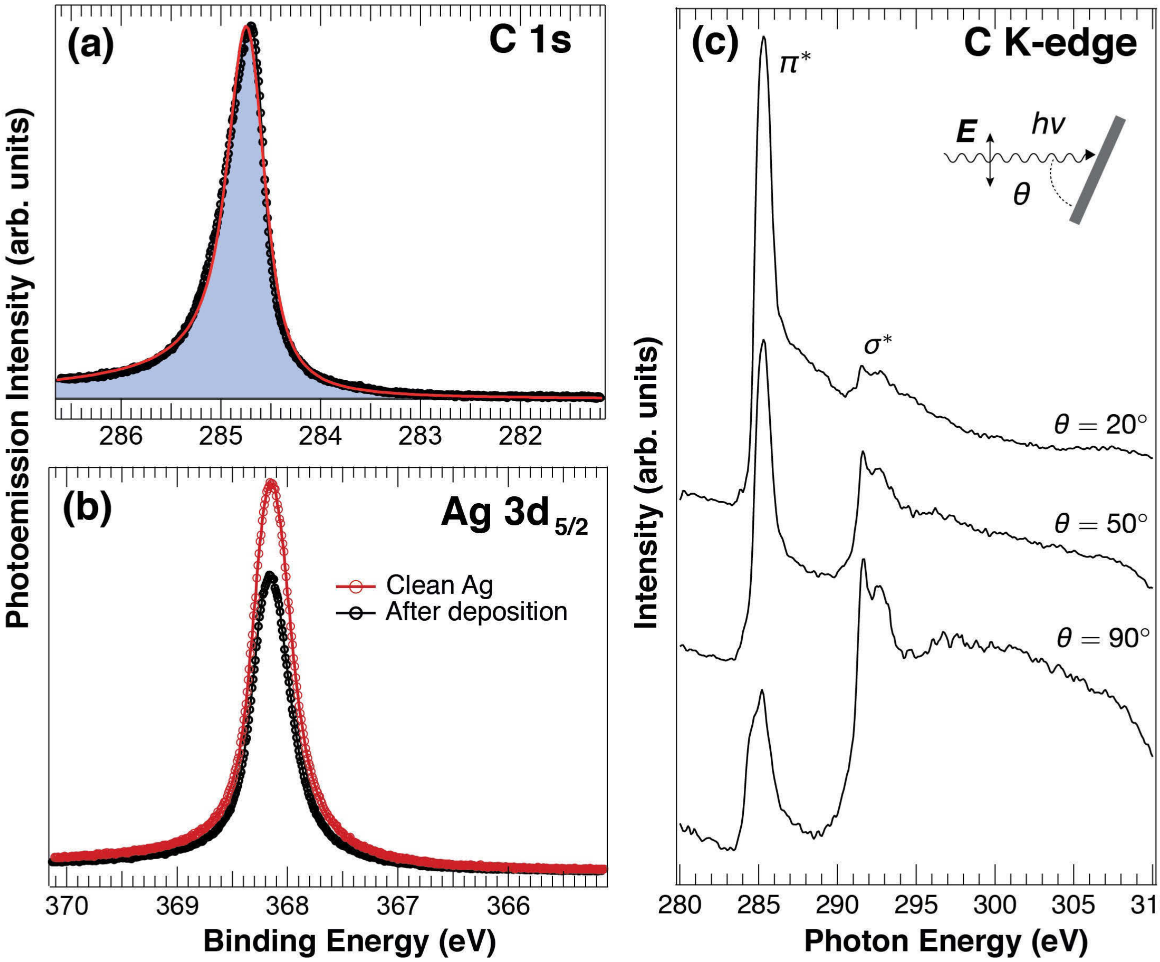

Figure 4.2: *(a) HR XPS spectrum of the C 1s core level acquired on the HTG sample.* $h\nu = 400\,eV$. *(b) Ag 3d core level of the clean and graphene-covered sample. (c) NEXAFS spectrum of the HTG sample acquired at different incidence angles of the photon beam. The geometry of the experiment is sketched in the panel.*

It is worth mentioning that no oxygen contamination was observed on the sample, unlike what shown in earlier literature for the growth of graphene on Ag (111) [10]. This ensures a very precise of the graphene growth on the surface and it allows a detailed assessment of the graphene-Ag interaction.

In order to confirm that graphene has formed on the surface, NEXAFS spectra at the carbon K-edge have been acquired to detect and monitor the direction of the carbon bonds. The outcomes of the experiment are shown in Fig. 4.2(c). Three spectra acquired at different angles of incidence of the photon beam with respect to the sample surface are plotted. The geometry of the experiment is sketched in the same panel. Two important features are evident in the absorption spectrum at 285.3 and 291.6 eV photon energy, with their intensity depending on the incidence angle. In order to establish a link and validate our hypothesis, we can compare these NEXAFS spectra with those reported in literature for graphene on various substrates [15, 16, 17, 18].

The structure at 285.3 eV can be associated with the transition of C 1s electrons towards conduction π^* states around the M and L points of the Brillouin zone (BZ), while the structure observed at 291.5 eV originates from the promotion of core electrons into σ^* states in the centre of the Brillouin zone. A difference can be seen in the NEXAFS signal for the π^* and σ^* structures acquired at different photon incidence angles. An enhancement of the π^* resonance was observed in grazing incidence conditions (i.e. $\theta = 20°$), indicating that the orientation of the π orbital is perpendicular to the sample plane. Likewise, the enhancement of the σ^* structure with the polarisation vector of the light parallel to the surface indicates that the σ orbital lies in the plane of the sample. However, the dichroism observed is not complete, when compared to other graphene samples [15, 18], since the contributions of the π^* and σ^* resonances are always visible. This outcome hints at the presence of C sp^2 bonds which are tilted with respect to the sample plane and therefore are indicative of disordered structures. Since the dichroic signal is quite significant, we can infer that the Ag surface is mostly covered by a graphene lattice, but also some disordered carbon structures are present.

Low-energy electron diffraction (LEED) patterns acquired on the sample, as shown in fig. 4.3, provided important information on the structure features of the deposited layer. Besides the $(1, 0)$ spot of the Ag(111) substrate, a ring-like structure with an even distribution of the intensity is visible, which corresponds to a lattice parameter smaller than that of the Ag substrate. By assuming that $\mathbf{a}_{\mathrm{Ag}} = 2.88\text{Å}$, we could extract the value of the lattice parameter corresponding to the ring, which results to be $\mathbf{a}_{\text{gr}} = 2.46 \pm 0.02$Å, well in agreement with the values reported for graphene. The even intensity of the ring-like structure indicates that the graphene layer does not display azimuthal order and it is likely to be formed by several graphene domains oriented in any azimuthal direction. Interestingly, a ring-like structure was present in LEED patterns acquired on graphene samples grown on Au(111) and Pt(111) with a similar deposition technique [11], whereas the intensity of the ring structure was not evenly distributed as for our growth on Ag(111), showing instead marked maxima. These maxima are indicative of preferential orientation of the graphene layer and therefore pinpoint to an active role of the substrate interaction in orienting the graphene flakes. In our case, since no clear intensity maxima were observed, we infer that the interaction of graphene on Ag(111) is weak and it is not acting as a template to orient the graphene layers, producing a distribution of random azimuthally rotated graphene domains.

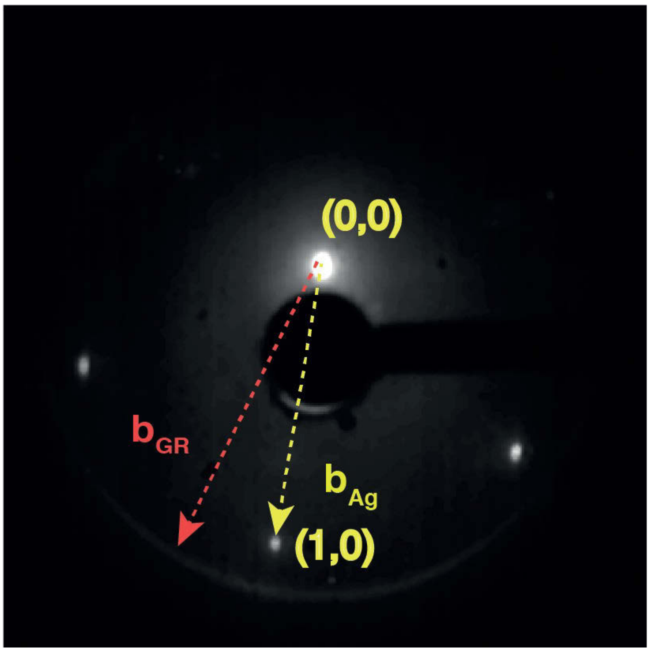

Figure 4.3: *LEED pattern acquired on the HTG sample,* $E_p = 76$ *eV. The reciprocal lattice vectors for Ag and graphene are highlighted.*

The stability of this structure has been tested by annealing the freshly prepared sample while monitoring the evolution of the C 1s core level with fast XPS, as shown in Fig. 4.4. The HTG graphene sample was initially annealed with a ramp of 2 K/s up to 1100 K and subsequently kept at this temperature for 1 hr. During this interval, we observed a slow but constant decrease of the C 1s signal until its almost complete disappearance. Such behavior indicates that the graphene layer is not stable at high temperature on the silver surface because the C layer dissolves into the Ag bulk.

We then conclude that the structure grown by exposing the Ag(111) surface to carbon, while keeping the substrate at 1000 K, has graphene character and it is comparable with what produced in similar conditions in earlier reports [10, 11]. The azimuthal disorder observed in LEED and the consequent presence of several domain boundaries in graphene can result in a broadening of the C 1s core level (FWHM = 520 meV), when compared with graphene grown by CVD on weakly interacting metals, such as Ir(111). This outcome is consistent with what observed in XPS spectra for a defect-rich graphene layer [19], where the broadening of the C 1s peak is a sign of the presence of vacancies defects and domain boundaries. Moreover, we point out that the C 1s lineshape is also determined by the interaction of graphene with the underlying substrate in case of strongly interacting systems, as already observed for Re(0001) [20] and Ru(0001) [21], due to the coexistence of carbon atoms differently interacting with the metal underneath, thus having slightly different binding energy. However, in our case the first hypothesis of defects causing the broadening of the C 1s peak is more likely because graphene/Ag(111) is a weakly interacting system [10].

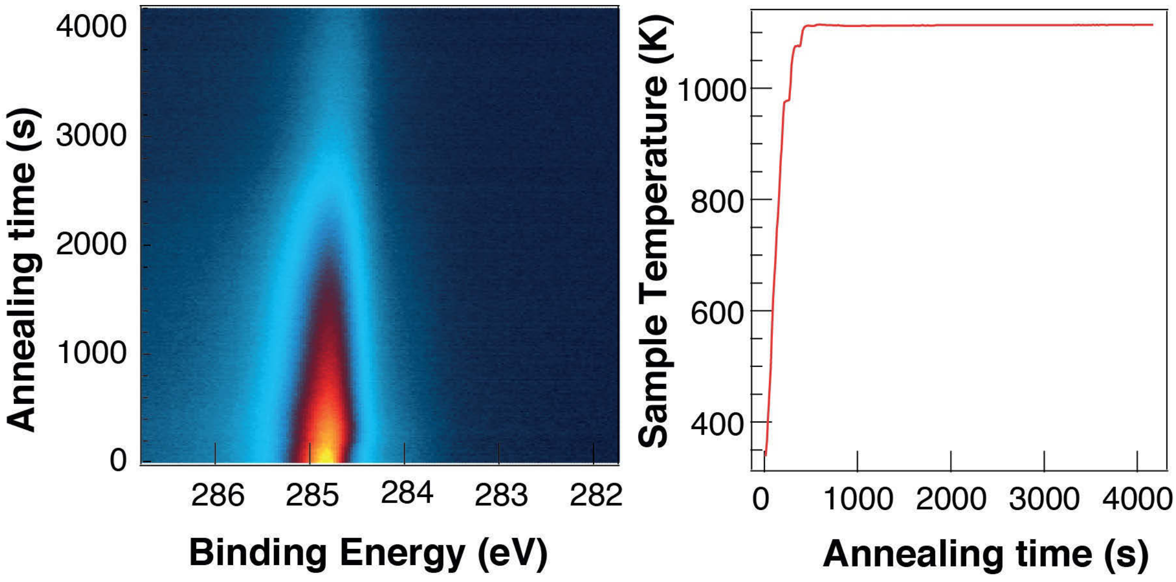

Figure 4.4: *Time-evolution of the C 1s core level as resulting from fast XPS acquisition during an annealing ramp. The trend of the sample temperature vs time is shown in the right panel.*

4.3.2 Temperature Programmed Growth (TPG)

A different strategy can be devised in order to grow graphene with the C source. Such protocol is usually labelled as Temperature Programmed Growth (TPG) and it consists of two steps: the initial deposition of a carbon precursor on the metal surface at RT followed by annealing at high temperature, which transforms the deposited material into an ordered graphene layer. This approach was successfully exploited to grow graphene on Ir(111) by CVD [13] or to grow layers of other 2D materials, such as hBN [22] or MoS_2 [23]. In this section the feasibility of this approach to grow an ordered graphene layer by employing the atomic C source is assessed.

In Fig. 4.5 (a) it is shown the evolution of the C 1s core level during carbon uptake, while keeping the sample at RT. A broad peak is detected in a few minutes and it appears to be very different from what observed for the HTG. An intense peak centered at ca. 283.7 eV BE was observed, sided by two other peaks as evidenced in the high resolution C 1s spectrum acquired after the deposition and shown in Fig. 4.5-(b). These broad components are located at 282.85 (C_1), 283.79 (C_2) and 284.31 eV (C_3) BE. As evidenced in Fig. 4.5-(c) the components C_1 and C_2 grew simultaneously during exposure, while C_3 kept a smaller growth rate. After ca. 150 s of exposure, we noticed that the trend of growth of C_1 significantly changed and decreased with

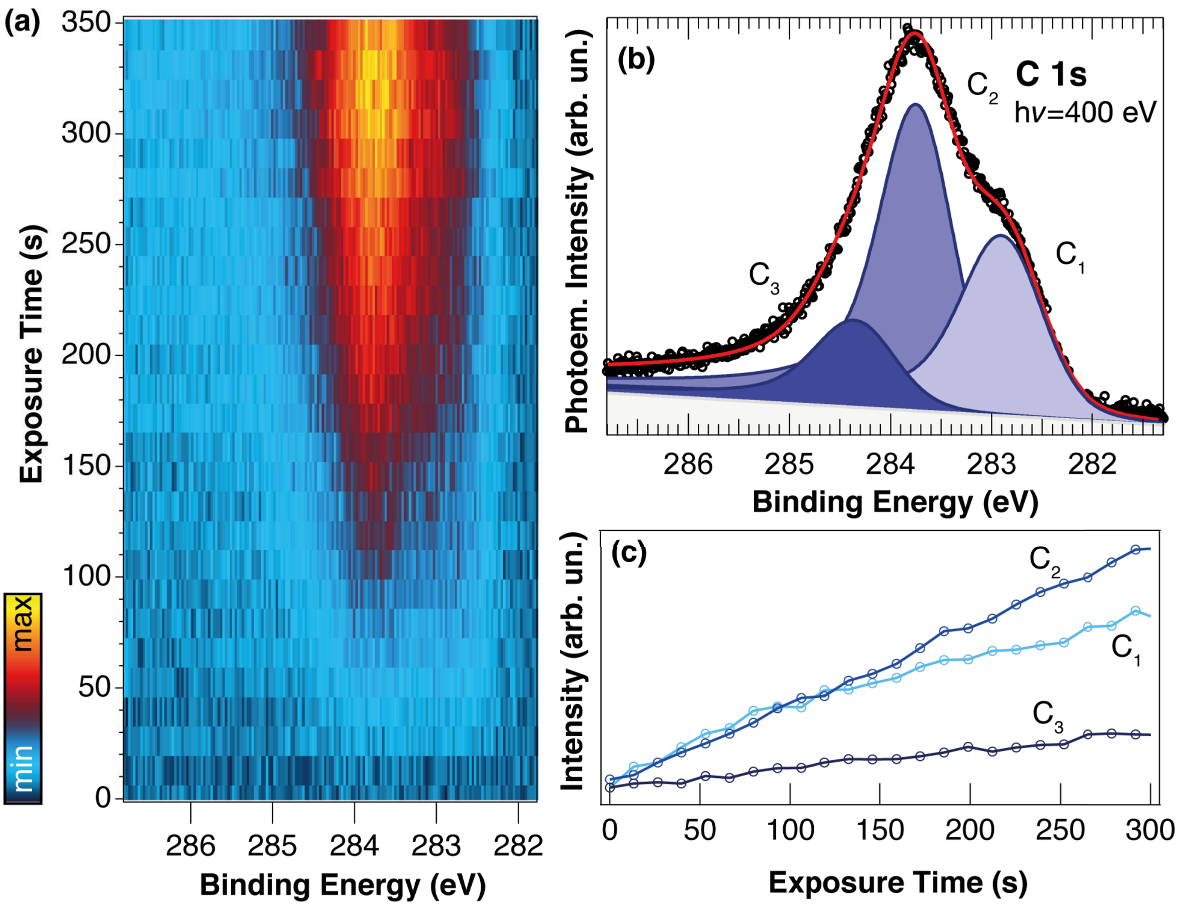

Figure 4.5: *(a) C 1s core level during the uptake of C from carbon source on Ag(111) at RT. $h\nu = 400$ eV. (b) C 1s core level after the growth, together with peak fit analysis (c) Evolution of the three components of the C 1s level during the growth.*

respect to C_2. This outcome is remarkably different from what observed for the HTG process.

NEXAFS spectra (Fig. 4.6) acquired on the sample were considerably different than those described in the previous section for the HTG sample. It was still possible to individuate some structure that we could identify as belonging to $C\ 1s \rightarrow \sigma^*$ and $C\ 1s \rightarrow \pi^*$ transitions. However, the π^* structure at 285.3 eV did not show any appreciable dichroism as we observed for the HTG sample, while only a minor dichroic signal was detected for the σ^* component. This could indicate that the sample is constituted mainly by areas covered with carbon species with bonds different than sp^2 or whose sp^2 bonds are not oriented in an ordered lattice. However, a small portion of these bonds lies parallel to the surface and originates the modest dichroism of the σ^* peak. We speculate that this signal could be due to graphene-like

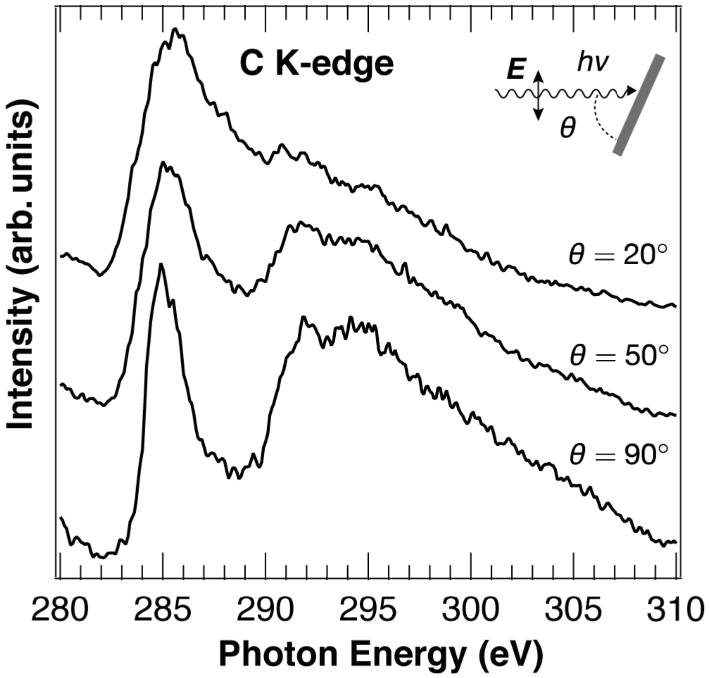

Figure 4.6: *C K-edge NEXAFS spectra acquired at different incidence angles of the photon beam.*

structures originating also the C_3 component in the C 1s core level.

In addition, the LEED pattern (not shown) showed only attenuated spots belonging to the Ag substrate, hinting at the growth of a disordered overlayer rather than graphene.

The second step of the TPG protocol consists in the annealing up to 1100 K of the carbon deposited sample with an heating ramp of 2 K/s. The evolution of the C 1s during this post-annealing is shown in Fig. 4.7. It can be noticed that, despite a change in the binding energy of the peaks, the overall shape of the C 1s level does not change with the temperature. Moreover, in contrast with what happens for the HTG growth, the carbon overlayer does not dissolve into the crystal bulk at high temperature. One can then imagine that the carbon species arriving on the Ag surface at RT do not have the necessary mobility to diffuse on the metal surface and to form an ordered graphene layer. Given the stability of the TPG sample even at high temperature and the shape of the C 1s core level we can speculate that amorphous carbon clusters form on the surface which do not dissolve into the crystal bulk.

These combined results highlight the crucial role of the temperature substrate during C deposition in order to obtain an ordered graphene layer. We found that 1000 K is the optimal temperature to avoid the formation of carbon clusters and promote the growth of graphene. Indeed a graphene growth attempt performed an intermediate temperature (800 K) returned a mixture of graphene and carbon clusters on the surface, as indicated by the C 1s and the NEXAFS measurements.

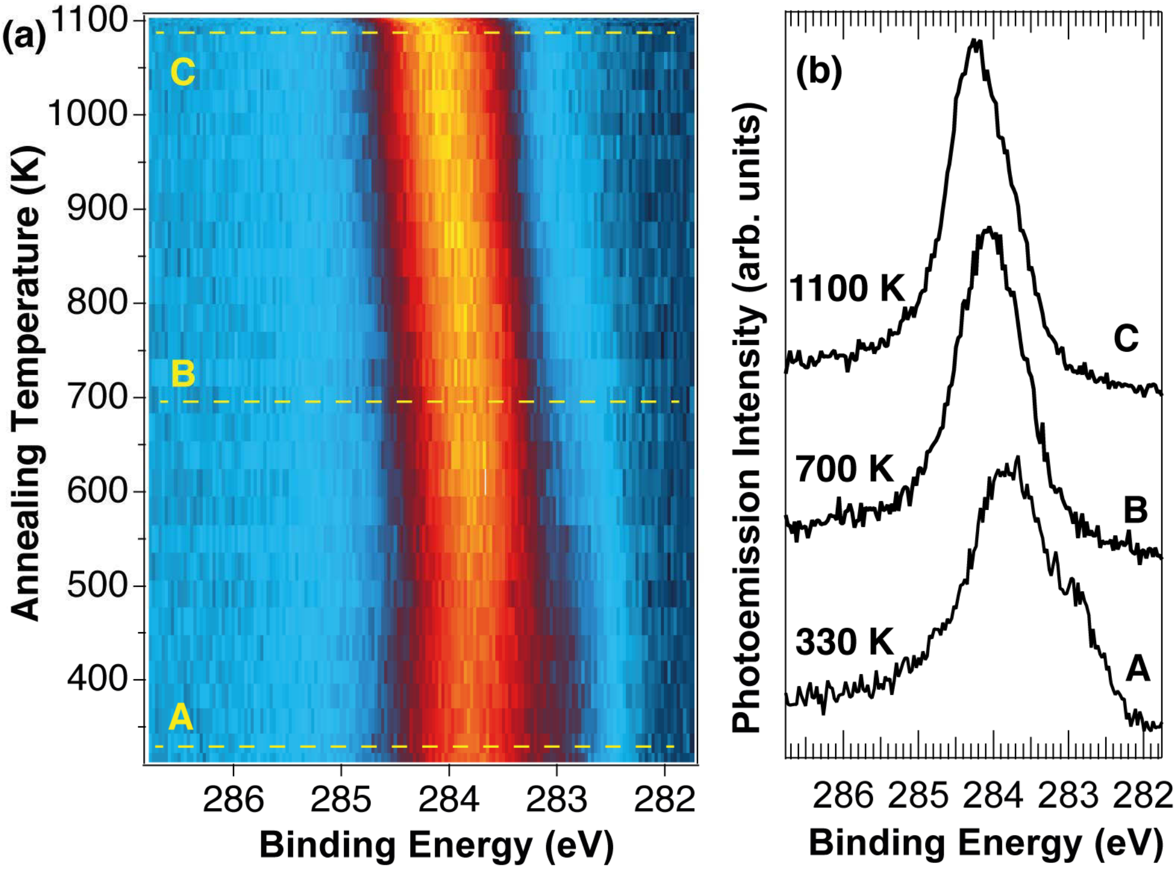

Figure 4.7: *(a) C1s intensity plot during the TPG growth annealing with heating rate of 2K/s. (b) Photoemission spectra acquired at different temperatures outlined by the cuts in (a).*

4.4 Conclusions

In summary, we have shown the importance of the sample temperature to achieve an ordered graphene layer when depositing carbon with an atomic C source on Ag(111). A combination of HR-XPS and NEXAFS measurements showed that the HTG deposition performed at 1000 K yields the formation of a graphene layer, which results to be n-doped. However, the acquisition of LEED patterns evidenced a ring-like structure corresponding to the lattice periodicity of graphene hinting at the presence of several rotated graphene domains. On the other hand, the TPG growth did not succeed in producing a graphene layer. The outcomes are instead indicative of the presence of amorphous carbon on the surface. A post-annealing after the deposition at room temperature did not alter significantly the situation, leaving the C 1s core level unaltered, which is at variance with the complete dissolution at 1100 K of the graphene layer produced with HTG.

Bibliography

[1] M. Batzill, *The surface sciennce of graphene: Metal interfaces, CVD synthesis, nanoribbons, chemical modifications, and defects*, Surf. Sci. Rep. **67**, 83-115 (2012).

[2] Y. Dedkov and E. Voloshina, *Graphene growth and properties on metal substrates*, Journ. of Phys.: Cond. Matt. **27**, 30 (2015).

[3] E. Voloshina and Y. Dedkov, *Graphene on metallic surfaces: problems and perspectives*, Phys. Chem. Chem. Phys. **14**, 13502-13514 (2012).

[4] A.J. Martínez-Galera, I. Brihuega, and J.M. Gómez-Rodríguez, *Ethylene Irradiation: A New Route to Grow Graphene on Low Reactivity Metals*, Nano Lett. **11**, 3576-3580 (2011).

[5] G. Pan, B. Li, M. Heath, D. Horsell, M.L. Wears, L. Al Taan, and S. Awan, *Transfer-free growth of graphene on SiO_2 insulator substrate from sputtered carbon and nickel films*, Carb. **65**, 349-358 (2013).

[6] J. Cai, P. Ruffieux, R. Jaafar, M. Bieri, T. Braun, S. Blankenburg, M. Mouth, A.P. Seitsonsen, M. Salex, X. Feng, K. Müllen, and R. Fasel, *Atomically precise bottom-up fabrication of graphene nanoribbons*, Nature **466**, 470-473 (2010).

[7] S. Linden, D. Zhong, A. Timmer, N. Aghdassi, J.H. Franke, H. Zhang, X. Feng, K. Müllen, H. Fuchs, L. Chi, and H. Zacharias, *Electronic Structure of Spatially Aligned Graphene Nanoribbons on Au(788)*, Phys. Rev. Lett. **108**, 216801 (2012).

[8] J. Tesch, P. Leicht, F. Blumenschein, L. Gragnaniello, M. Fonin, L.E.M. Steinkasserer, B. Paulus, E. Voloshina, and Y. Dedkov, *Structural and electronic properties of graphene nanoflakes on Au(111) and Ag(111)*, Sci. Rep. **6**, 23439 (2016).

[9] J. Park, W.C. Mitchel, L. Grazulis, H.E. Smith, K.G. Eyink, J.J. Boeckl, D.H. Tomich, S.D. Pacley, and J.E. Hoelscher, *Epitaxial Graphene Growth by Carbon Molecular Beam Epitaxy (CMBE)*, Adv. Mater. **22**, 4140-4145 (2010).

[10] B. Kiraly, E.V. Iski, A.J. Mannix, B.L. Fisher, M.C. Hersam, and N.P. Guisinge, *Solid-source growth and atomic-scale characterization of graphene on Ag(111)*, Nat. Commun. **4**, 2804 (2013).

[11] I. Hernández-Rodríguez, J.M. García, J.A. Martín-Gago, P.L. de Andrés, and J. Méndez, *Graphene growth on Pt(111) and Au(111) using a MBE carbon solid-source*, Diam. Rel. Mat. **57**, 58-62 (2015).

[12] S. Doniach, M.J. Šunjić, J. Phys. C: Solid State Phys. **3**, 285 (1970).

[13] S. Lizzit, G. Zampieri, L. Petaccia, R. Larciprete, P. Lacovig, E.D.L. Rienks, G. Bihlmayer, A. Baraldi, and P. Hofmann, *Band dispersion in the deep 1s core level of graphene*, Nat. Phys. **6**, 345-349 (2010).

[14] R. Larciprete, S. Ulstrup P. Lacovig, M. Dalmiglio, L. Bianchi, F. Mazzola, L. Hornekr F. Orlando, A. Baraldi, P. Hofmann, and S. Lizzit, *Oxygen Switching of the Epitaxial Graphene-Metal Interaction*, ACS Nano **6**, 9551-9558 (2012).

[15] R. Larciprete, P. Lacovig, F. Orlando, M. Dalmiglio, L. Omiciuolo, A. Baraldi, and S. Lizzit, *Chemical gating of epitaxial graphene through ultrathin oxide layers*, Nanoscale **7**, 2650-12658 (2015).

[16] D. Pacilé, M. Papagno, A.F. Rodríguez, M. Grioni, L. Papagno, C.O. Girit, J.C. Meyer, G.E. Begtrup, and A. Zettl, *Near-Edge X-Ray Absorption Fine-Structure Investigation of Graphene*, Phys. Rev. Lett. **101**, 066806 (2008).

[17] A.B. Preobrajenski, M.L. Ng, A.S. Vinogradov, and N. Mårtensson, *Controlling graphene corrugation on lattice-mismatched substrates*, Phys. Rev. B **78**, 073401 (2008).

[18] G. Levita, L. Petaccia, A. Comisso, S. Lizzit, R. Larciprete, A. Goldoni, and A. De Vita, *A Spectroscopic and ab Initio Study of the Formation of Graphite and Carbon Nanotubes from Thermal Decomposition of Silicon Carbide*, Nano Lett. **8**, 4335-4341 (2008).

[19] A. Barinov, O. B. Malcioğlu, S. Fabris, T. Sun, L. Gregoratti, M. Dalmiglio, and M. Kiskinova, *Initial Stages of Oxidation on Graphitic Surfaces: Photoemission Study and Density Functional Theory Calculations*, J. Phys. Chem. C **113**, 9009-9013 (2009).

[20] E. Miniussi, M. Pozzo, A. Baraldi, E. Vesselli, R. R. Zhan, G. Comelli, T. O. Mentes, M. A. Niño, A. Locatelli, S. Lizzit, and D. Alfè, *Thermal Stability of Corrugated Epitaxial Graphene Grown on Re(0001)*, Phys. Rev. Lett. **106**, 216101 (2011).

[21] D. Alfè, M. Pozzo, E. Miniussi, S. Günther, P. Lacovig, S. Lizzit, R. Larciprete, B.S. Burgos, T.O. Menteş, A. Locatelli, and A. Baraldi, *Fine tuning of graphene-metal adhesion by surface alloying*, Sci. Rep. **3**, 2430 (2013).

[22] F. Orlando, P. Lacovig, L. Omiciuolo, N.G. Apostol, R. Larciprete, A. Baraldi, and S. Lizzit, *Epitaxial Growth of a Single-Domain Hexagonal Boron Nitride Monolayer*, ACS Nano **8**, 12063-12070 (2014).

[23] S.S. Grønborg, S. Ulstrup, M. Bianchi, M. Dendzik, C.E. Sanders, J.V. Lauritsen, P. Hofmann, and J.A. Miwa, *Synthesis of Epitaxial Single-Layer* MoS_2 *on Au(111)*, Langmuir **31**, 9700-9706 (2015).

Chapter 5

Synthesis of sp^2 carbon on lead zirco-titanate (001)

5.1 Introduction

Ferroelectric materials are characterized by a spontaneous polarization that can be switched by applying an electric field. Recent studies have shown that graphene-ferroelectric systems open new possibilities in the creation of new transistor architectures. Graphene is supposed to constitute the conduction channel in a field effect transistor with a ferroelectric gate material. Novel memory properties may emerge from such a structure. Moreover, it has been reported that graphene field effect transistors prepared on $Pb(Zr,Ti)O_3$ (PZT) substrates of high quality exhibit a mobility in the range of 105 $cm^2V^{-1}s^{-1}$, considerably larger when compared to SiO_2–gated graphene devices [1]. For applications in electronics one needs a gap in the semiconducting material. However, intrinsic, single-layer graphene is gapless. The opening of a gap was reported when an electric field is applied perpendicular to a bilayer graphene [2, 3]. Hence, an out-of-plane ferroelectric polarization might help in this sense. It has to be noted also that graphene synthesized on ferroelectrics with alternate domains (with inward $P^{(-)}$ and outward polarization $P^{(+)}$) results in micrometric areas with excess electrons, respectively holes and the formation of micrometric p-n junctions inside the graphene layers [4]. The topology of these p-n junctions and their logical applications can be varied by the ferroelectric polarization distribution. Therefore, placing graphene layers on ferroelectrics may offer valuable solutions for engineering memory devices, controlled by the polarization of the substrate. The aim of the study exposed in this chapter was to undertake the first steps towards exploiting the remarkable conduction properties of graphene by synthesizing such layers on ferroelectric substrates.

5.1.1 Polarization state of the lead-zirco titanate surface

Fig. 5.1 shows the structure of lead zirco-titanate, Pb(Zr,Ti)O_3. The origin of the polarization P is due to the displacement of the central Ti and Zr ions which creates an electric field oriented in the same direction.

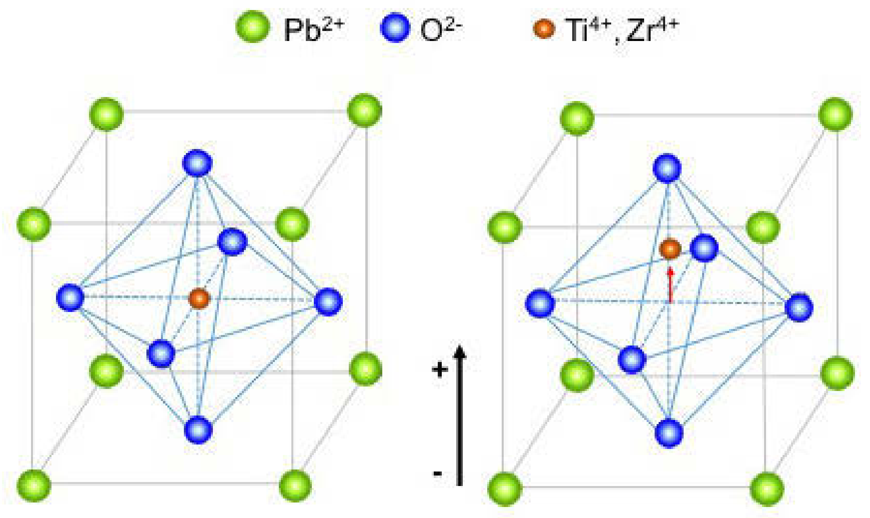

Figure 5.1: *The structure of the PZT crystal.*

A ferroelectric thin film with polarization P, assumed uniform inside the film, with polarization oriented out-of-plane, will develop a bound surface charge density of magnitude P and hence a depolarization field $E_d = P/(\varepsilon_0 \varepsilon_r)$, where ε_0 is the permittivity of vacuum and ε_r the dielectric constant of the material. For PZT, which is the ferroelectric material used throughout this chapter, $P \approx 1C/m^2$, $\varepsilon_r \approx 180$ [5], thus the depolarization field results as about 630 MV/m. This is huge compared with typical coercitive fields, in the range of 20 – 30 MV/m [6]. As a consequence, such state is highly instable and can adopt different solutions to eliminate this instability such as for example the use of compensating charges from adsorbates (e.g. hydroxyl, carboxyl radicals, or protons) to compensate from outside the bound charges, the use of compensating charges from metal electrodes in the case of metal / ferroelectric /

metal sandwich structures, or the use of compensation charges generated inside the ferroelectric crystal, generated by photoelectric or photovoltaic effects [7].

The compensating charges may be produced by the bottom electrode or generated by defects inside the film. In particular, oxygen vacancies are shallow donors with energies 0.06 – 0.3 eV below the minimum of the conduction band (E_C) [8]. The difference between the donor level and the Fermi level is found to be $E_F - E_D \approx 0.04$ eV [9], thus such levels are relatively easy to be thermally ionized. A particular case is that when the film thickness decreases under 100 nm. In that case, in order to obtain a sufficient surface charge density for the compensation of bound charges, the ferroelectric material should produce a larger amount of defects (oxygen vacancies), and indeed a thickness dependent study of sample compositions revealed the increase of the free carrier density together with that of oxygen vacancies when the film thickness decreases [9]. The various sources of electrons needed to compensate the depolarization field near the free surface for a PZT layer with outwards ($P^{(+)}$) orientation grown on a metal ($SrRuO_3$, SRO) are schematized in Fig. 5.2.

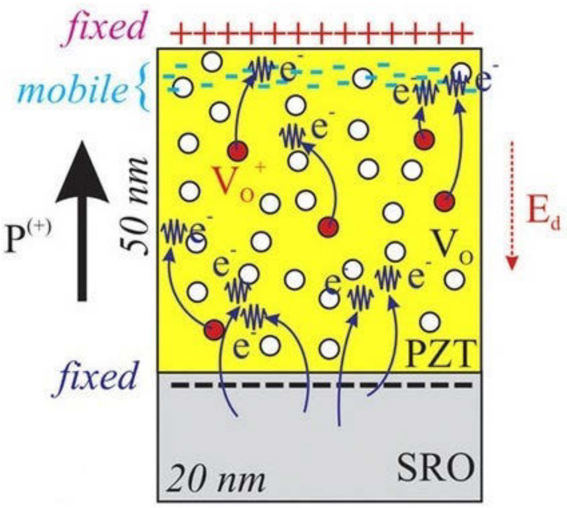

Figure 5.2: *Schematics of charge migration in order to compensate the depolarization field of a ferroelectric with outwards polarization. Red disks represent ionized oxygen vacancies, white disks represent neutral oxygen vacancies, and arrows represent migrating electrons. Adapted from [9].*

The compensating charges organize inside the ferroelectric in layers placed in the vicinity of the extremal surfaces [10]. When inside the ferroelectric the depolarization field is fully compensated, all bands are horizontal (see Fig.5.3). Then, near surfaces, more precisely in the region between the surface and the depolarizing charge sheet, some residues of the depolarization field subsist and this will induce a band bending whose magnitude may be written as $eP\delta/(\varepsilon_0\varepsilon_r)$, where e is the elementary charge. Again for the practical case of PZT discussed above, by supposing $\delta \approx 3$ nm [5], the obtained band bending is between 1 and 2 eV. This is a quite visible shift in X-ray photoelectron spectroscopy, provided all charging effects are properly taken into account.

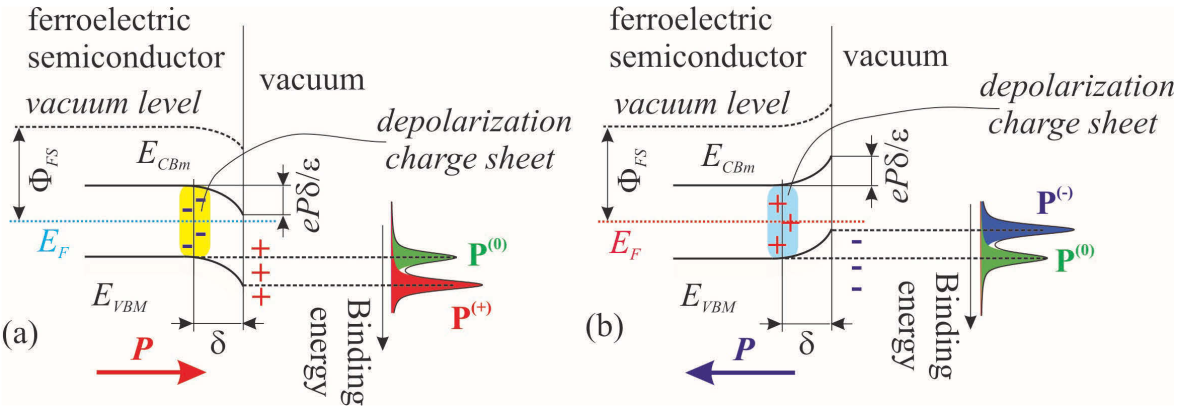

Figure 5.3: *Band diagrams near ferroelectric surfaces. (a) Polarization oriented outwards,* $P^{(+)}$*. (b) Polarization oriented inwards,* $P^{(-)}$*. The binding energies of core levels originating from regions near surface will be shifted to higher binding energies for (a) and to lower binding energies for (b). Reproduced from Ref. [11].*

Indeed, *in-situ* experiments from a $BaTiO_3$(001) single crystals sandwiched between electrodes revealed shifts in binding energies (Ba 3d, Ti 2p) by about 1.2 eV between states with polarization $P^{(+)}$ and $P^{(-)}$ [12]. For PZT(001), Figure 5.4 shows the XPS spectra of all core levels of single layers with outwards ($P^{(+)}$), inwards ($P^{(-)}$) and no out-of-plane polarization ($P^{(0)}$) [13].

The different polarization states were obtained as function on the contamination of the layers and concentration of oxygen vacancies. For instance, if the films are heated under ultrahigh vacuum, they loose oxygen and then the oxygen vacancies are in sufficient number to create an electron depolarizing sheet near surface, such as in Fig. 5.3 (a). If the films are extensively outgassed in oxygen atmosphere such as to remove carbon-containing molecules from their surface, then a state with cation vacancies may be stabilized, and these cation vacancies produce holes such as to re-create the situation from Fig. 5.3 (b). The layer with no out-of-plane polarization

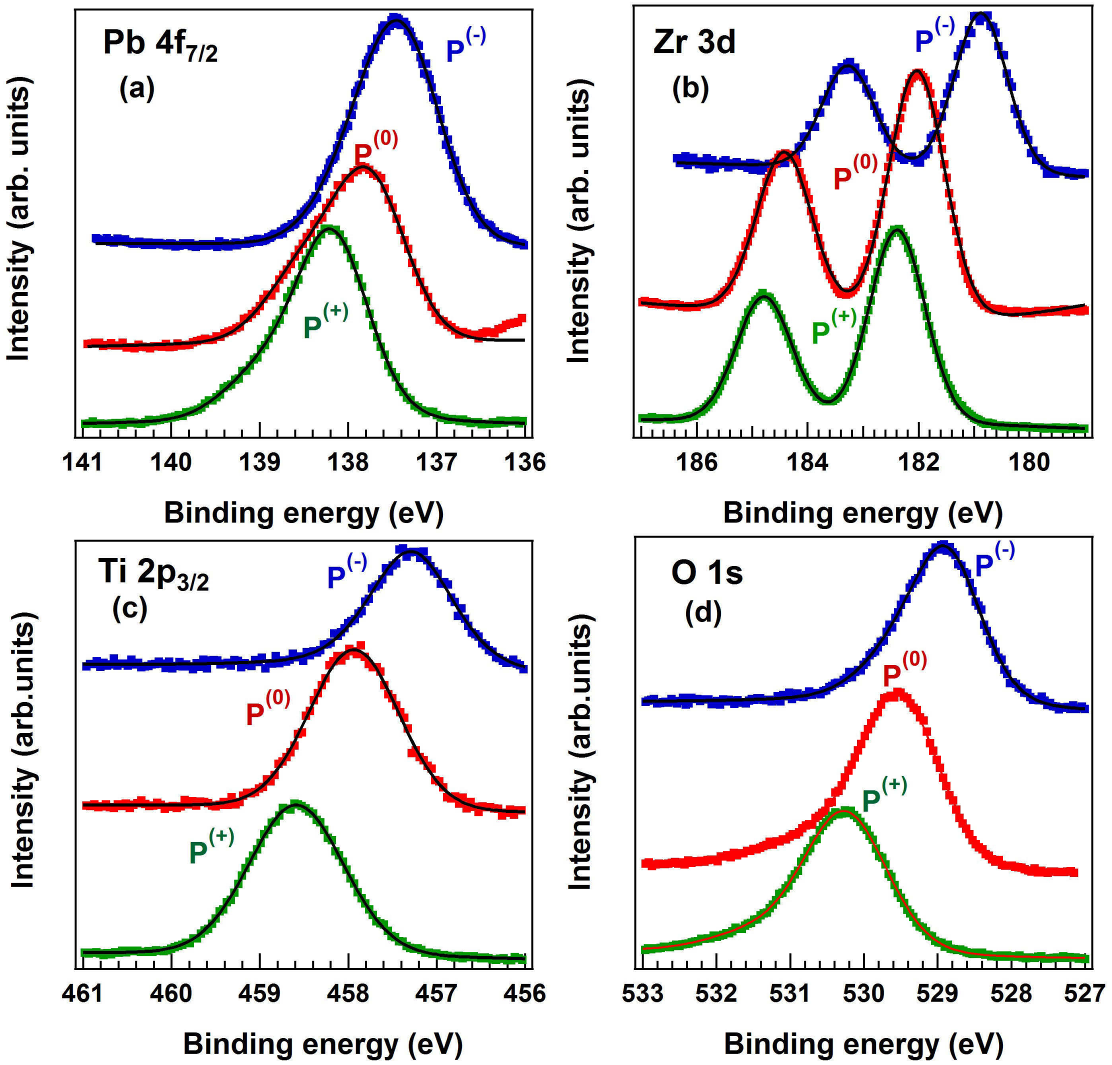

Figure 5.4: *X-ray photoelectron spectroscopy spectra of (a) Pb* $4f_{7/2}$*; (b) Zr 3d; (c) Ti* $2p_{3/2}$*; (d) O 1s for similar PZT(001) samples (20 nm thick) with different polarization states. Adapted from [13].*

was a highly defective layer obtained by repeated annealing cycles. It is clear then that binding energies may be used not only to derive the surface composition but also to assess the polarization state of the film near surface.

5.2 Experimental methods

Single crystals 10 nm thick PZT layers were grown by pulsed laser deposition (PLD) on Pt(001) by the group of Dr. Pintilie at the NIMP in Magurele, Romania. The PLD setup is operated with KrF radiation (248 nm wavelength), 0.7 J x 20 ns pulses, repetition rate 5 Hz, laser fluence 2 J cm^{-2}. During growth, the substrate was annealed to 850 K in a partial O_2 pressure of 0.2 mbar [14]. Under these preparation conditions, there is a general agreement that the preferred polarization of the PZT layers is $P^{(+)}$ [15, 16]. The samples were exposed to air, then introduced in the UHV analysis chamber.

The measurements related to the cleaning procedure of the PZT samples in UHV were performed at the CoSMoS facility at Elettra. Different photon energies were used to measure the core levels of the different elemental species: Pb 4f and Zr 3d were measured at 260 eV, Ti 2p and O1s at 600 eV, C1s at 400 eV and valence band at 120 eV photon energy, respectively. The overall energy resolution (photon beam plus analyzer) was always better than 100 meV. The measurements were performed at room temperature. The measurements on the growth of sp^2 carbon on PZT were performed in the SuperESCA chamber. The carbon-dose set-up used for carbon deposition was the same as the one used in the experiments of chapters 3 and 4, with same evaporation rates. In order to calibrate the carbon coverage on PZT we compared the C 1s intensity with the one of graphene on Pt(100), which was achieved by standard CVD with ethylene at a temperature of 970 K. All the core level spectra are referenced to the Fermi level measured on an Ag foil placed in the vicinity of the sample. The NEXAFS spectra were measured in Auger Yield mode by collecting the Auger KLL electrons with the electron energy analyzer in an energy window of 10 eV. All spectra were analyzed by using Doniach Šunjić functions with asymmetry set to zero (Voigt profiles) and associated backgrounds for accounting inelastic losses [17, 18]. The integral amplitudes were then used, calibrated by the atomic photoionization cross sections [19] at different photon energies and by the flux of the undulator, to obtain approximate compositions of the layers.

5.3 Cleaning procedure in ultrahigh vacuum

In general, the composition of lead zirco-titanate $PbZr_{0.2}Ti_{0.8}O_3(001)$ may change during the annealing needed for the cleaning process of the surface after introduction in UHV. For this reason, we developed a specific cleaning procedure, in UHV which consists in prolonged cycles of oxygen dose at a specific temperature followed by annealing. The most efficient conditions were found to be O_2 partial pressure of 5 x 10^{-5} mbar at 670 K for a total time of 5 hours, followed by annealing in UHV at 870 K for having a PbO terminated surface which changes to (Ti, Zr)O_2 termination after 1 hour annealing to 850 K in 5 x 10^{-5} mbar O_2 pressure. The XPS spectra are represented in Fig. 5.5 and in Table 5.1 are presented the ratios between the different components of the PZT after each single treatment. The integral intensities were normalized with the photoionization cross section (2.142 Mb for Pb 4f at hν= 260 eV, 4.716 for Zr 3d at hν = 260 eV, 1.203 for Ti 2p at hν = 600 eV, 0.412 for O 1s at hν = 600 eV) [19] and a further correction of I(260 eV)/I(600 eV) = 2.31 was considered for the variation of the synchrotron beam intensity I at the two different photon energies. The *as introduced* sample has a clear excess of Pb and oxygen, since the PZT target of the PLD set-up is enriched in PbO. After the first oxygen treatment at 670 K, the initial carbon peak of Fig. 5.5 (e) almost disappears and the oxygen content in the sample drastically increases. However, only after the subsequent annealing in UHV to 870 K the C 1s peak intensity goes to zero and the Pb/(Zr+Ti) decreases towards unity. A second oxygen treatment at 670 K did not lead to appreciable changes. Values of Pb/(Zr+Ti) larger than 1 are to be expected from photoelectron inelastic mean free path (IMFP) effects. The ratio $Pb/(Zr + Ti) \approx exp(\pm c/(2\lambda cos\theta)$, where c is the out-of-plane lattice constant, λ the IMFP, and the photoelectron take-off angle θ which was of 40°. The IMFP is considered roughly the same for all core levels analyzed, since the photon energies were chosen such that the measurement is highly surface sensitive. The sign ‚+' is valid for PbO termination, while the sign ‚–' is valid for (Ti,Zr)O_2 termination (see sketch from Fig. 5.1). From the values from Table 5.1, one obtains $\lambda \approx$ 6.1 Å for the surface after the second O_2 treatment (assumed to be PbO – terminated) and $\lambda \approx$ 4.6 Å for the surface after the final annealing to 850 K in O_2 atmosphere (assumed to be (Ti,Zr)O_2 – terminated). These values are in reasonable agreement with the expected values of 5-7 Å from the universal curve of IMFP for kinetic energies between 70 and 140 eV [20]. Therefore we can derive with a good approximation which is the termination of the layers. Note also that the O/(Zr + Ti) ratio exceeds in both cases the estimated ratio 1 + $2exp(-c/(2\lambda cos\theta)]$, or $2 + exp(-c/(2\lambda cos\theta)$ for PbO and (Ti,Zr)O_2 terminations, respectively. This points towards a lack of cations near surface. Since the polarization is clearly $P^{(+)}$, as found from the binding energy position of the peaks which is consistent with accumulation of electrons near surface and this implies the creation of oxygen vacancies, we believe that this method is partially inadequate for of a precise determination of compositions. Thus, the ratios from Table 5.1 will not be taken as absolute values, but we will rather investigate their relative variations. However, the Pb/(Zr + Ti) ratio seems more adequate to be analyzed in the following.

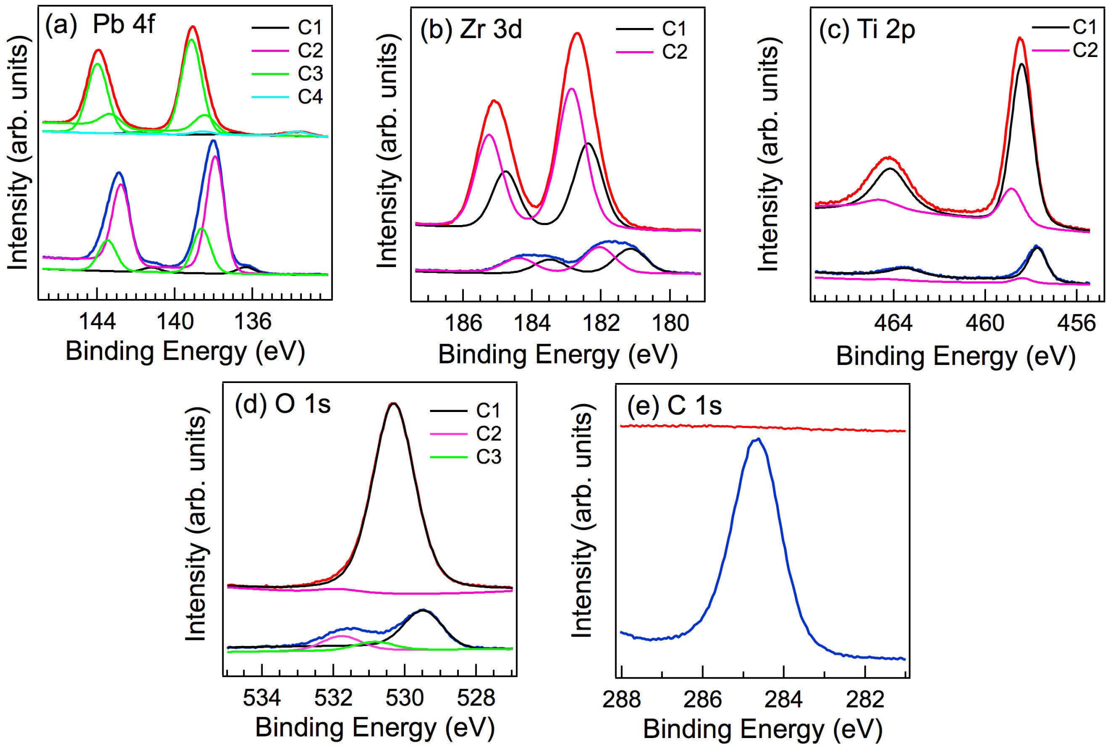

Figure 5.5: *X-ray photoelectron spectroscopy spectra of (a) Pb 4f; (b) Zr 3d; (c) Ti 2p; (d) O 1s; (e) C 1s. Bottom curves are for the "as introduced" sample while top curves are after the last treatment of Table 5.1. The curves are vertically shifted for displaying purpose. Adapted from [21].*

		Core level binding energies (eV)					
Sample	Comp.	Pb $4f_{7/2}$	Zr $3d_{5/2}$	Ti $2p_{3/2}$	O 1s	Composition	
"as introduced"	C1	136.355	181.151	457.713	529.470	Pb/(Zr+Ti)	5.383
	C2	137.923	182.041	458.392	530.840	O/(Zr+Ti)	4.321
	C3	138.626	-	-	531.770	Zr/(Zr+Ti)	0.534
First O_2 treatment. 5 x 10^{-5} mbar. 670 K. t= 5 h then cool down in O_2	C1	136.626	180.937	457.541	529.928	Pb/(Zr+Ti)	5.427
	C2	137.726	181.596	458.651	529.107	O/(Zr+Ti)	7.543
	C3	138.367	-	-	530.979	Zr/(Zr+Ti)	0.419
	C4	132.468	-	-	-		
Annealing in UHV at 870 K	C1	136.923	182.388	458.403	530.072	Pb/(Zr+Ti)	1.376
	C2	138.416	182.325	458.832	531.151	O/(Zr+Ti)	3.942
	C3	138.761	-	-	-	Zr/(Zr+Ti)	0.474
	C4	133.274	-	-	-		
Second O_2 treatment. 5 x 10^{-5} mbar. 670 K t= 3h then cool down in O_2	C1	136.485	181.299	457.822	529.578	Pb/(Zr+Ti)	1.535
	C2	138.414	182.046	458.230	531.151	O/(Zr+Ti)	4.443
	C3	137.885	-	-	-	Zr/(Zr+Ti)	0.486
	C4	132.730	-	-	-		
Annealing at 850 K in 5 x 10^{-5} mbar O_2 pressure	C1	137.119	182.066	458.909	530.306	Pb/(Zr+Ti)	0.568
	C2	139.152	182.731	458.389	531.861	O/(Zr+Ti)	2.924
	C3	138.437	-	-	-	Zr/(Zr+Ti)	0.630
	C4	133.694	-	-	-		

Table 5.1: *Binding energies and compositions extracted from the XPS data for all core levels (Pb 4f, Zr 3d, Ti 2p, O 1s), and for all components, denoted with C1, C2, C3 and C4 used in the fit for the "as introduced" sample and after the cleaning procedure. The integral intensities are normalized by the photoionization cross section and by the photon flux at a specific photon energy.*

5.4 Experimental results

The growth of carbon layers was achieved by dosing carbon with the solid carbon source, on the (Ti, Zr)O_2 terminated PZT(001)/Pt(001) keeping the substrate at high temperature. This is needed to increase carbon mobility on the surface which is important to achieve a high quality carbon layer.

Photoelectron spectroscopy was used to investigate the polarization state of the substrate, by following the core level shifts due to the surface band bending. After surface preparation, as explained in previous paragraph, a first carbon deposition was performed at 670 K for 30 min, then the layer was annealed. Keeping the temperature at 820 K carbon was removed (Fig. 5.6 (a) and (b)). In the second deposition (Fig. 5.7), the layer was initially heated to 820 K, then C evaporation was initiated and the temperature was decreased to 730 K, where carbon sticking on the surface increased considerably. The sample was then again annealed up to 780 K during carbon dose in order to provide the highest surface mobility to the carbon atoms. After deposition 2 we added further carbon by performing the following depositions 3 and 4 always at 780 K. All depositions were characterized by photoelectron spectroscopy as shown in the figures, while depositions 2, 3 and 4 were analyzed also by NEXAFS at the carbon K-edge.

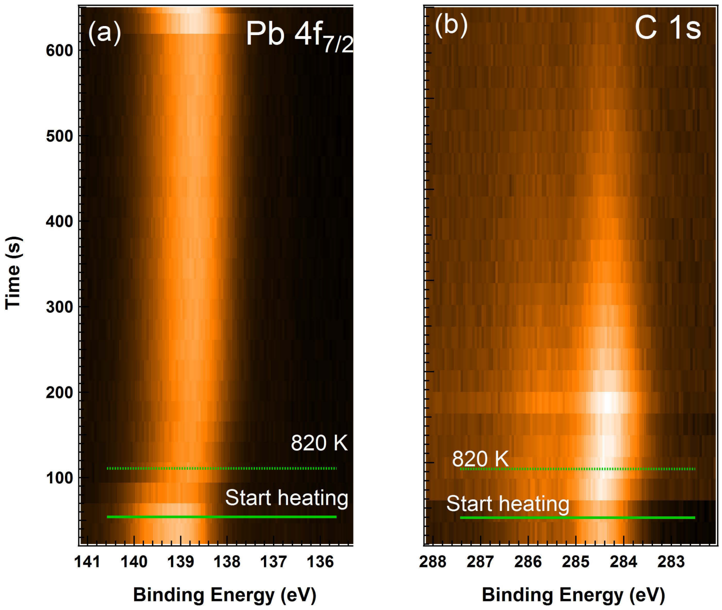

Figure 5.6: *Time evolution shown as a two- dimensional plot of (a) Pb 4 $f_{7/2}$ and (b) C 1s during annealing at 820 K after deposition 1. Adapted from [21].*

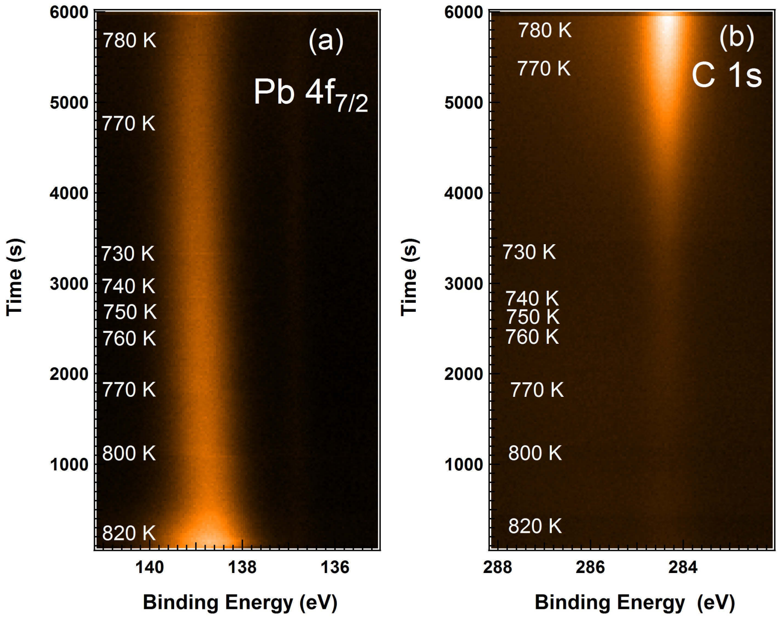

Figure 5.7: *Two dimensional plot of the time evolution of (a) Pb $4f_{7/2}$ and (b) C1s during deposition 2. Carbon starts to adsorb on PZT film at a temperature of 730 K. The polarization of the substrate (binding energy of the Pb core level) is unchanged. Adapted from [21].*

In Fig. 5.8 is presented the evolution of the main peaks for the various depositions. All binding energies of the main lines from the substrate (Pb $4f_{7/2}$, Zr $3d_{5/2}$, Ti $2p_{3/2}$, O 1s) are consistent with the $P^{(+)}$ polarization of the PZT (001) as explained in the previous paragraph. This polarization state does not change upon carbon deposition.

The results of the analysis of the peaks obtained after the various carbon depositions are summarized in Table 5.2.

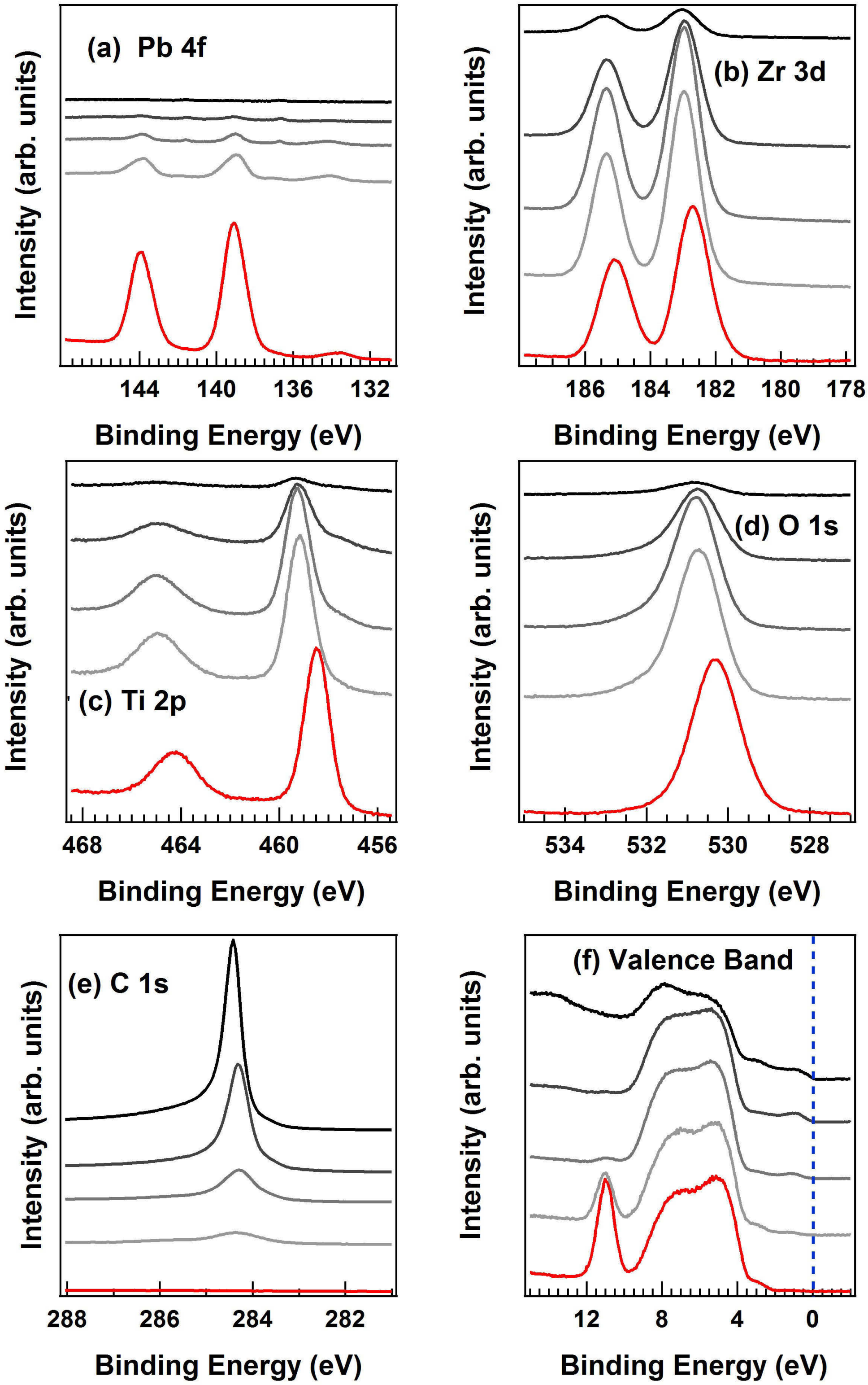

Figure 5.8: *X-ray photoelectron spectroscopy of Pb(Zr, Ti)O_3 layers for cleaned (red curves) and after carbon deposition (grey curves, which represent from bottom to top: deposition 1, deposition 2, deposition 3 and deposition 4): (a) Pb 4f, $h\nu = 260$ eV; (b) Zr 3d, $h\nu = 260$ eV; (c) Ti 2p, $h\nu = 600$ eV, (d) O 1s, $h\nu = 600$ eV, (e) C 1s, $h\nu = 400$ eV; (f) valence band, $h\nu = 120$ eV. The spectra are vertically shifted for displaying purpose. Adapted from [21].*

Core level binding energies (eV)							
Sample	Comp.	Pb $4f_{7/2}$	Zr $3d_{5/2}$	Ti $2p_{3/2}$	O 1s	Composition	
Clean sample	C1	137.119	182.066	458.909	530.306	Pb/(Zr+Ti)	0.568
	C2	139.152	182.731	458.389	531.861	O/(Zr+Ti)	2.924
	C3	138.437	-	-	-	Zr/(Zr+Ti)	0.630
	C4	133.698	-	-	-		
Deposition 1 t= 30 min	C1	137.205	182.816	458.662	530.713	Pb/(Zr+Ti)	0.134
	C2	138.851	183.144	459.081	531.962	O/(Zr+Ti)	3.412
	C3	139.588	182.048	459.495	-	Zr/(Zr+Ti)	0.492
Annealing 820 K	C1	137.144	181.924	458.654	530.615	Pb/(Zr+Ti)	0.411
	C2	138.754	182.912	459.072	531.806	O/(Zr+Ti)	3.507
	C3	139.459	-	459.473	-	Zr/(Zr+Ti)	0.491
	C4	132.730	-	-	-		
Deposition 2 t= 100 min (fig. 5.7)	C1	136.747	182.970	457.904	530.770	Pb/(Zr+Ti)	0.036
	C2	138.866	-	458.995	531.954	O/(Zr+Ti)	2.993
	C3	139.336	-	459.452	-	Zr/(Zr+Ti)	0.515
	C4	138.083	-	-	-		
Deposition 3 t=75 min	C1	136.714	182.939	457.986	530.719	Pb/(Zr+Ti)	0.028
	C2	138.999	-	458.923	531.944	O/(Zr+Ti)	2.670
	C3	140.065	-	459.408	-	Zr/(Zr+Ti)	0.564
	C4	137.802	-	457.221	-		
Deposition 4 t= 50 min	C1	136.670	183.010	457.661	530.770	Pb/(Zr+Ti)	0.005
	C2	139.021	-	458.837	-	O/(Zr+Ti)	2.537
	C3	-	-	459.433	-	Zr/(Zr+Ti)	0.632

Table 5.2: *Binding energies and compositions extracted from the XPS data for all core levels (Pb 4f, Zr 3d, Ti 2p, O 1s), for samples after different C depositions and treatments.*

After the first deposition, it can be observed that the Pb/(Zr + Ti) ratio decreases drastically (from about 0.57 to about 0.13). This deposition implies a quite small amount of carbon, far below one monolayer as will be explained in the following. Thus, this decrease in the intensity from Pb means either that some Pb is ejected from the sample by carbon deposition, or some Pb is 'pushed' inside the ferroelectric layer. After the annealing to 820 K and removal of all carbon (see Fig.5.6 (b)), the ratio Pb/(Zr + Ti) is partially recovered, to about 0.41. It is therefore likely that Pb is pushed inside the film somehow, by the presence of carbon at the surface, thus it recovers at the surface upon carbon desorption. Larger amounts of carbon deposited (depositions 2, 3 and 4)(though still below the surface density of graphene) yield quite low amount of detectable Pb signals (Pb/(Zr + Ti) decreases to 5 x 10^{-3}). A reaction such as $Pb(Zr,Ti)O_3 + C \rightarrow (Zr,Ti)CO_3 + Pb$ could be possible, but no carbonate peak is visible in the C 1s or in the Ti 2p spectra. The C 1s spectra of the depositions 1 and 2 (see Fig. 5.9) are fitted with two components with binding energies of 284.3 eV and 285.8 eV. The first should be a C–C bond, whereas the second peak may be attributed to C-O bonds [22]. Thus, we may rule out a chemical reaction like the one proposed above (moreover, such reaction should be at least partly reversible, according to the observations with the partial retrieval of the Pb intensity after carbon desorption). This should rather be a physical process leading to the Pb burying inside the film.

A strong decrease of the peak from the valence band with about 11 eV binding energy is also observed (Fig. 5.8 (f)). Practically, this peak is seriously reduced starting already with deposition 2. Theoretical calculations [23] traced the origin of this feature as a mix of Pb 6s and O 2p states. The fact that the occupancy of these states is strongly reduced by carbon ad-atoms is consistent with the strong decrease of the Pb signal due to the migration of Pb inside the PZT bulk.

In Fig. 5.10 is presented the evolution of the C 1s spectra, for the different carbon doses together with the deconvolutions by using either two Voigt profiles (1^{st} and 2^{nd} deposition) or Doniach- Šunjić function (deposition 3 and 4, and graphene on Pt(100)). We index the C1s spectra with the surface area occupied by one carbon atom, which, for graphene, is 2.62 $Å^2$. The peak corresponding to C–O bonds at about 285.8 eV decreases in intensity for the 2^{nd} deposition (Fig. 5.9), whereas for the 3^{rd} and 4^{th} deposition was not detected anymore (Fig 5.10). At the same time, the C 1s signal starts to be better described by a Doniach-Šunjić lineshape combined with a Gaussian distribution [24], which is a sign that the C layer behaves like a metal. This happens, indeed, when the C surface density approaches that of graphene (one carbon per 2.85 $Å^2$, as compared with one carbon per 2.62 $Å^2$ for graphene). From this

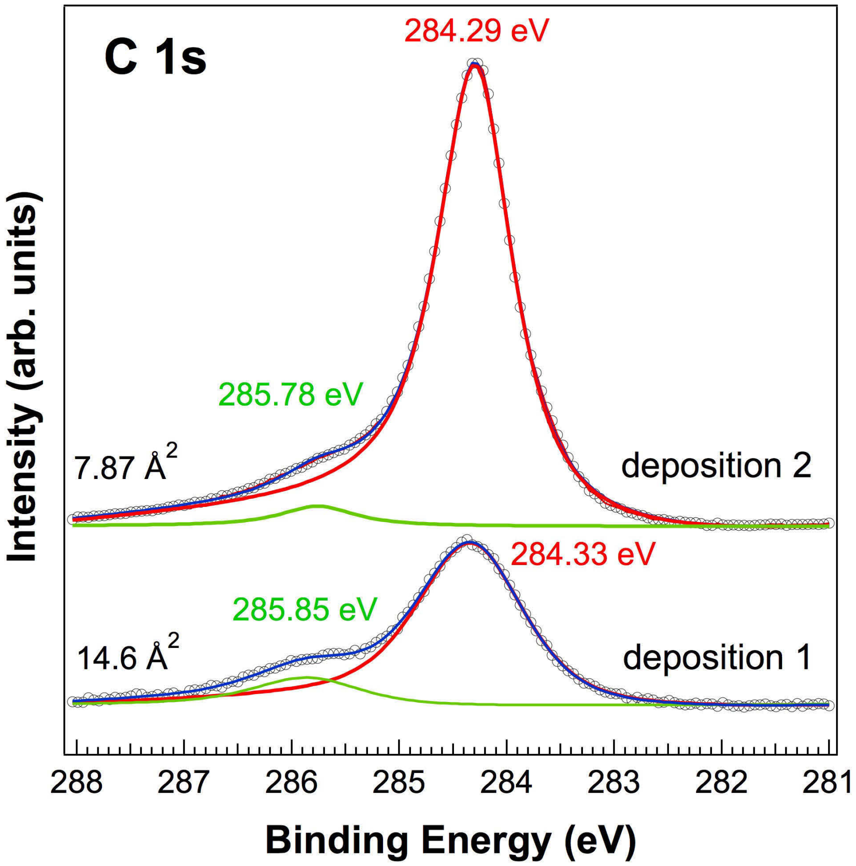

Figure 5.9: *XPS spectra for C 1s core level after deposition 1 and deposition 2. The black circles represent the experimental data, the grey line is the fit and the color lines are each separate component. The spectra were fitted with a Voigt function . The spectra are vertically shifted for displaying purpose. Adapted from [21].*

we may state that carbon layers may be synthesized with a surface density similar to graphene, with electrons delocalized and no (or weak) chemical bond with the substrate. The value of the Doniach-Šunjić asymmetry α parameter obtained from the fit, was close to that obtained for the graphene grown on Pt(001): $\alpha \approx 0.12$ for graphene/Pt(001), 0.18 for the deposition 3 (1 C / 3.49 Å^2) and 0.28 for the deposition 4 (1 C / 2.84 Å^2)(Fig 5.10).

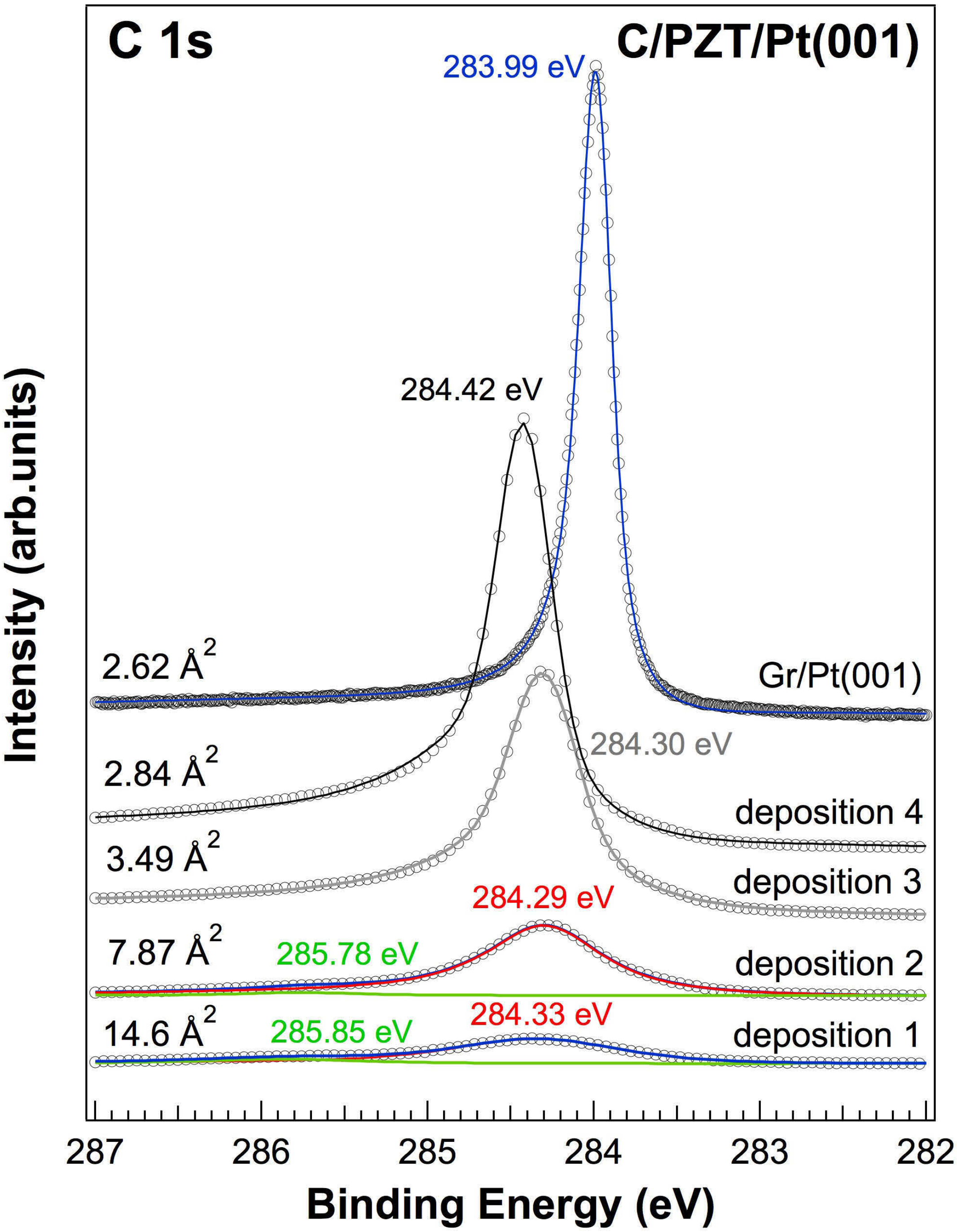

Figure 5.10: *XPS spectra for C 1s core level after each Carbon deposition and for Graphene deposited on Pt(001). The black circles represent the experimental data, the grey line is the fit and the color lines are each separate component. The spectra of deposition 1 and 2 were fitted with a Voigt function, while all other spectra were fitted with a Doniach-Šunjić convoluted with a gaussian broadening. A Shirley background was included in the fits.Adapted from [21].*

The two dimensional character of the deposited carbon layers is quantified by NEXAFS measurements. In general, NEXAFS spectra of graphitic systems present well-defined π^* (built from p_z orbitals) and σ^* (built from p_{xy} orbitals) resonances [25]. Taking into account that the photoabsorption cross section implies mostly transitions on p orbitals oriented along the direction of the incoming electric field, it follows that a different ratio between π^* and σ^* lines (the so called dichroism) is observed when the direction of the electric field is varied with respect to the surface . Normal incidence absorption ($\theta = 90°$) results in the increase of the σ^* resonances and a quenching of the π^*, while the opposite is observed when the electric field is normal to the surface (grazing incidence) [26]. In the ideal case, like Gr/Pt, σ^* resonances disappear at grazing incidence, while π^* resonances disappear at normal incidence [26, 27]. We have performed measurements on the Gr/Pt(100) sample and the result is shown in Fig. 5.11. An almost complete dicroism is observed for this sample, as expected from the previous considerations. The fitting of the σ^* and π^* resonances with $sin^2\theta$ and $cos^2\theta$ dependence, respectively, confirms that the sp^2 bonds of graphene are aligned parallel to the surface.

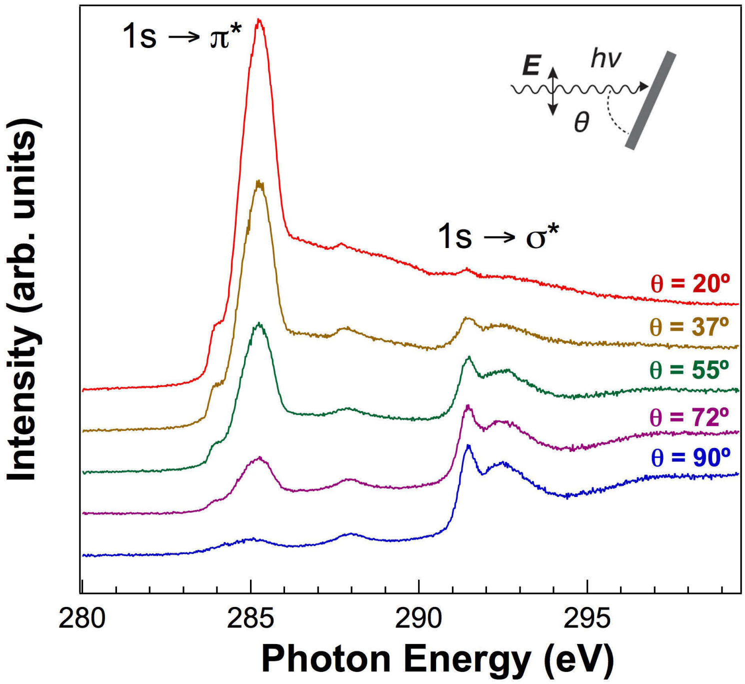

Figure 5.11: *NEXAFS spectra at C K edge for different incidence angles, in the case of Gr/Pt(001). The inset shows the geometry of the experiment. Adapted from [21].*

In the case of the carbon layers deposited on PZT (see Fig. 5.12), we detected a clear σ^* and π^* resonances with a noticeable dichroism for deposition 2 (Fig. 5.12 (a)) and a weaker effect for deposition 3, (Fig. 5.12 (b)) while for deposition 4, the dichroism vanishes (Fig. 5.12(c)). This shows that the carbon layers have a graphitic character and start to grow with the sp^2 bonds parallel to the PZT surface but, at increasing coverage, this order is lost and the sp^2 bonds tend to be randomly oriented.

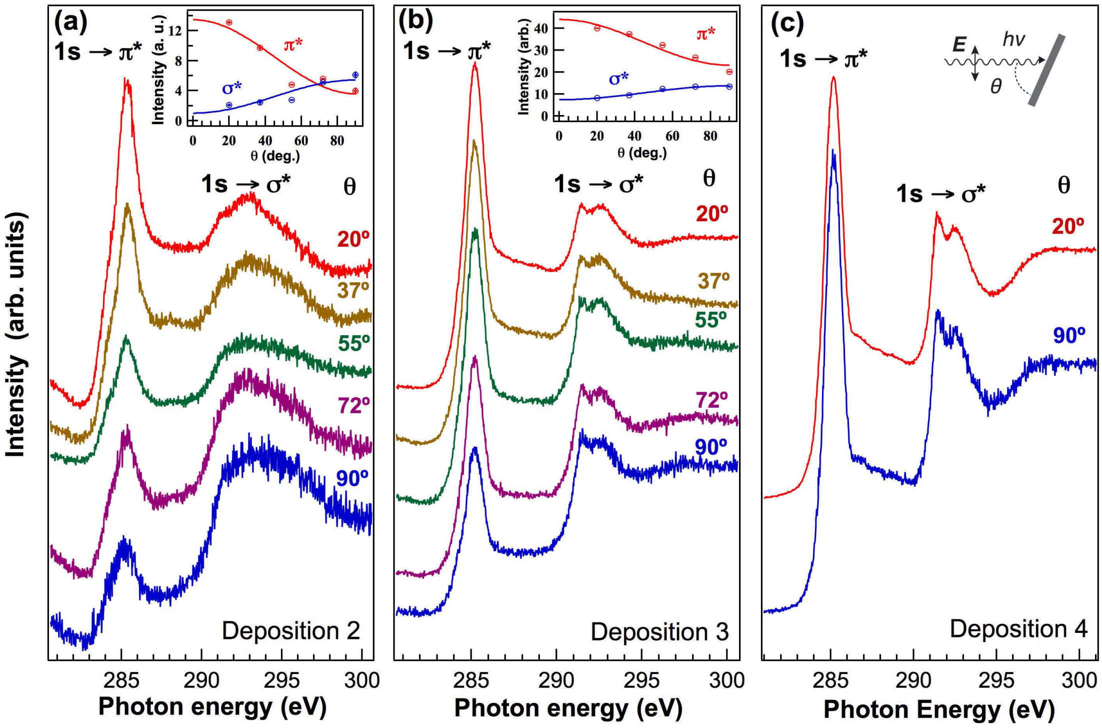

Figure 5.12: *(a) NEXAFS spectra at C K edge of (a) deposition 2 (b) deposition 3 (c) deposition 4 taken at different angles θ. Inserts in (a) and (b) are the fits of the intensities of σ^* and π^* with $\sin^2\theta$ and $\cos^2\theta$ dependence, respectively. The inset in (c) shows the geometry of the experiment. Adapted from [21].*

5.5 Conclusions

This set of experiments are the first evidence that carbon layers can be grown on PZT(001) without influencing the $P^{(+)}$ polarization of the ferroelectric. A key role is played by the deposition temperature which should not exceed 780 K in order for the C atoms to adsorb on the surface. The dichroism of the C K- edge NEXAFS shows the prevalence of in-plane sp^2 bonds for layers whose effective coverage is below the graphene surface density. A side effect is the quenching of the Pb signal upon carbon adsorption, which is probably due to the Pb migration inside the PZT. Carbon does not substitute lead (otherwise, it should form titanium and zirconium carbonates with different signatures in XPS, which are not observed). We may also speculate that the small amount of Pb left on the surface has binding energy close to that of metallic Pb. Moreover, we cannot exclude the formation of Pb–C bonds on the surface.

Bibliography

[1] X. Hong, A. Posadas, K. Zou, C.H. Ahn, J. Zhu, *High-mobility few-layer graphene field effect transistors fabricated on epitaxial ferroelectric gate oxides*, Phys. Rev. Lett. **102**, 136808, (2009).

[2] F. Schwierz, *Graphene transistors* Nat. Nanotech. **5**, 487-496 (2010).

[3] K.F. Mak, C.H. Lui, J. Shan and T.F. Heinz, *Observation of an electric-field-induced band gap in bilayer graphene by infrared spectroscopy*, Phys. Rev. Lett. **102**, 256405 (2009).

[4] C. Baeumer, S.P. Rogers, R.J. Xu, L.W. Martin, M.S. Shim, *Ferroelectrically driven spatial carrier density modulation in graphene*, Nano Lett. **13**, 1693-1698 (2013).

[5] L. Pintilie, I. Boerasu, M.J.M. Gomes, T. Zhao, R. Ramesh, M. Alexe, *Metal-ferroelectric-metal structures with Schottky contacts. II. Analysis of the experimental current-voltage and capacitance-voltage characteristics of Pb(Zr,Ti)O3 thin films*, J. Appl. Phys. **98**, 124104 (2005).

[6] I. Pintilie, C.M. Teodorescu, C. Ghica, C. Chirila, A.G. Boni, L. Hrib, I. Pasuk, R. Negrea, N.G. Apostol, L. Pintilie,*Polarization-control of the potential barrier at the electrode interfaces in epitaxial ferroelectric thin films*, ACS Adv. Mater. Interf. **6**, 2929-2939 (2014).

[7] D.G. Popescu, M.A. Huşanu, L. Trupină, L. Hrib, L. Pintilie, A. Barinov, S. Lizzit, P. Lacovig, C.M. Teodorescu, *Spectro-microscopic photoemission evidence of charge uncompensated areas in Pb(Zr,Ti)O3(001) layers*, Phys. Chem. Chem. Phys. **17**, 509-520 (2015).

[8] T. Shimada, T. Ueda, J. Wang, T. Kitamura, *Hybrid Hartree-Fock density functional study of charged point defects in ferroelectric* $PbTiO_3$, Phys. Rev. B **87**, 174111 (2013).

[9] L. Pintilie, C. Ghica, C.M. Teodorescu, I. Pintilie, C. Chirila, I. Pasuk, L. Trupina, L. Hrib, A.G. Boni, N.G. Apostol, L.E. Abramiuc, R. Negrea, M. Stefan, D. Ghica, *Polarization induced self-doping in epitaxial* $Pb(Zr_{0.20}Ti_{0.80})O_3$ *thin films*, Sci. Rep.**5**, 14974 (2015).

[10] L. Pintilie, M. Alexe, *Metal-ferroelectric-metal heterostructures with Schottky contacts. I. Influence of the ferroelectric properties*, J. Appl. Phys. **98**, 124103 (2005).

[11] N.G. Apostol, C.M. Teodorescu, *Band bending at metal-semiconductor interfaces, ferroelectric surfaces and metal-ferroelectric interfaces investigated by photoelectron spectroscopy*, Surf. Sci. Charact. Techn. for Nanomat., C. Kumar (Ed.), Springer, Berlin, pp. 405-461 (2015).

[12] F. Chen, R. Schafranck, W. Wu, and A. Klein, *Reduction-induced Fermi level pinning at the interfaces between* $Pb(Zr,TI)O_3$ *and Pt, Cu and Ag metal electrodes*, J. Phys. D: Appl. Phys. **44**, 255301 (2011).

[13] L.C. Tănase, N.G. Apostol, L.E. Abramiuc, C.A. Tache, L. Hrib, L. Trupină, L. Pintilie, C.M. Teodorescu, *Ferroelectric triggering of carbon monoxide adsorption on lead zirco-titanate (001) surfaces*, Sci. Rep. **6**, 35301 (2016).

[14] N.G. Apostol, L.E. Stoflea, G.A. Lungu, C.A. Tache, L. Pintilie, and C.M. Teodorescu, *Band Bending at Ferroelectric Surfaces and Interfaces Investigated by X-ray Photoelectron Spectroscopy* , Mater. Sci. Eng. B **178**, 1317–1322 (2013).

[15] L. Pintilie, V. Stancu, L. Trupina, I. Pintilie, *Ferroelectric Schottky diode behavior from a SrRuO3-*$Pb(Zr_{0.2}Ti_{0.8})O_3$*-Ta structure*, Phys. Rev. B **82**, 085319 (2010).

[16] N.G. Apostol, L.E. Stoflea, G.A. Lungu, C. Chirila, L. Trupina, R.F. Negrea, C. Ghica, L. Pintilie, C.M. Teodorescu, *Charge transfer and band bending at* $Au/Pb(Zr,Ti)O_3$ *interfaces investigated by photoelectron spectroscopy*, Appl. Surf. Sci. **273**, 415-425 (2013).

[17] C.M. Teodorescu, J.M. Esteva, R.C. Karnatak, A. El Afif, *An approximation of the Voigt I profile for the fitting of experimental x-ray absorption data*, Nucl. Instrum. Meth. Phys. Res. A **45**, 141-147 (1994).

[18] D. Mardare, D. Luca, C.M. Teodorescu, D. Macovei, *On the hydrophilicity of nitrogen-doped* TiO_2 *thin films*, Surf. Sci. **601**, 4515-4520 (2007).

[19] J.J. Yeh, I. Lindau, *Atomic subshell photoionization cross sections and asymmetry parameters:* $1 \leq Z \leq 103$, At. Data Nucl. Data Tables **32**, 1-155 (1985).

[20] S. Hüffner, *Photoelectron Spectroscopy: Principles and Applications*, Springer, Berlin (2003).

[21] N.G. Apostol, G.A. Lungu, I.C. Bucur, **C.A. Tache**, L. Hrib, L. Pintilie, D. Macovei and C.M. Teodorescu, *Non-interacting, sp2 carbon on a ferroelectric lead zirco-titanate: towards graphene synthesis on ferroelectrics in ultrahigh vacuum*, RSC Advances **6**, 67883 (2016).

[22] M. Iliut, C. Leordean, V. Canpean, C.M. Teodorescu, S. Astilean, *A new green, ascorbic acid-assisted method for versatile synthesis of Au-graphene hybrids as efficient surface-enhanced Raman scattering platforms*, J. Mater. Chem. C **1**, 4094-4104 (2013).

[23] J. Robertson, W.L. Warren, B.A. Tuttle, D. Dimos, D.M. Smyth, *Shallow* Pb^{3+} *hole traps in lead zirconate titanate ferroelectrics*, Appl. Phys. Lett. **63**, 1519-1521 (1993).

[24] J.J. Joyce, M. Del Giudice, J.H. Weaver, *Quantitative analysis of synchrotron radiation photoemission core level data*, J. Electr. Spectrosc. Relat. Phenom. **49**, 31-45 (1989).

[25] P. Batson, *Carbon 1s near-edge-absorption fine structure in graphite*, Phys. Rev. B: Condens. Matter Mater. Phys. **48**, 2608-2610 (1993).

[26] O. Wessely, M.I. Katsnelson and O. Eriksson, *Ab Initio Theory of Dynamical Core-Hole Screening in Graphite from X-Ray Absorption Spectra*, Phys. Rev. Lett. **94**, 167401 (2005).

[27] E. Voloshina, R. Ovcharenko, A. Shulakov and Y. Dedkov, *Theoretical description of X-ray absorption spectroscopy of the graphene-metal interfaces*, J. Chem. Phys. **138**, 154706 (2013).

[28] J. Guyonnet, *Ferroelectric Domain Walls. Statics, Dynamics, and Functionalities Revealed by Atomic Force Microscopy*, Springer Theses: Recognizing Outstanding Ph.D. Research, Springer, Berlin (2014).

Outlook and perspectives

The main goal of the research activity presented in this PhD thesis was to develop new methods of growing graphene beyond the usual Chemical Vapour Deposition (CVD). The strategy followed for doing this was the molecular beam epitaxy (MBE), where C atoms are directly delivered on the surface. The initial activity was focused on the design and construction of a solid C source, and on its subsequent use on different substrates like Ir(111), where the CVD technique is well established, Ag(111) and PbZr$_{0.2}$Ti$_{0}$.8O$_3$ (PZT(001)), which is a ferroelectric oxide, where CVD is precluded.

For most of the samples two different strategies were used: the Temperature Programmed Growth (TPG), in which C is deposited on the substrate at low temperature followed by annealing at high temperature and the High Temperature Growth (HTG), in which the substrate is hold at high temperature during C dose. We used TPG on Ir(111) to understand the incipient stage growth mechanism of graphene. We firstly performed C deposition at T=80K in order to reduce surface diffusion. The C1s XPS measurements, coupled to DFT calculations, revealed that at very low coverage not only C monomers, but also C dimers are present on the surface, while with increasing C coverage and substrate temperature also C clusters with 3, 4 and 5 atoms form. By using HTG we were able to grow graphene on Ir(111) of high quality, comparable to that grown by CVD. Moreover, with HTG it was possible to produce more than one layer of graphene. The growth of a second and third layer takes places at the Ir surface after C intercalation through the first graphene layer.

In the case of Ag(111), we were able to grow single layer graphene using the HTG method, at a sample temperature of 1000 K, while with TPG the carbon deposited at room temperature did not convert into graphene upon annealing. Annealing Temperatures of the graphene layer higher than 1000 K led to the dissolution of graphene into the Ag bulk, while at lower deposition temperatures the graphene quality decreased, as seen with XPS, LEED and Near Edge X-ray Absorption Spectroscopy (NEXAFS). In any case also the best graphene layer produced presented azimuthal disorder with no preferential orientation, while the NEXAFS spectra as a function of the incidence angle of the photon beam with respect to the substrate confirmed that the sp^2 bonds were aligned with the sample surface. From the position of the C1s peak it was also possible to estimate that the graphene layer on Ag(111) is slightly n-doped. The growth of graphene on top of PZT(001) turned out to be quite challenging. Prior to C deposition, we developed a method to clean the as-introduced samples in UHV, which consisted in prolonged cycles of oxygen dose at high temperature followed by annealing in UHV. This procedure produced a PbO terminated PZT(001), while the $(Ti,Zr)O_2$ termination was obtained after further prolonged annealing in oxygen atmosphere at high temperature. Although the polarization state of the atomically clean PZT(001) surface is able to polarize the CO molecules leading to their adsorption and partial dissociation, ethylene, that is commonly used in the CVD growth of graphene, does not adsorb on PZT(001), nor does it dissociate. Therefore, the need of using the carbon source to attempt graphene growth. The C layers grown on PZT(001) exhibited a nearly two dimensional character, up to a carbon surface density approaching that of graphene. The dichroism of C K-edge NEXAFS showed the prevalence of in-plane sp^2 bonds. However, a side effect of the carbon dose was a strong quenching of the Pb signal, most probably due to Pb migration into the PZT bulk.

This work has to be continued on several aspects. Other experiments with more systematic investigations and on other substrates where CVD is precluded need to be done. One particular case is the direct growth of graphene on top of Al_2O_3 formed by oxidation of the Ni_3Al alloy. This system has been already studied but the graphene layer was first produced on Ni3Al, then the substrate was oxidized via oxygen intercalation through graphene. The comparison between the two methods would give further insight into the strategy to be used to grow a high quality graphene on an insulator. Photoemission spectroscopy and NEXAFS measurements should be complemented with scanning tunneling microscopy investigations in order to determine the structure of the system at the atomic level.

Publications

Papers related to the thesis:

- N.G. Apostol, G.A. Lungu, I.C. Bucur, **C.A. Tache**, L. Hrib, L. Pintilie, D. Macovei and C.M. Teodorescu, *Non-interacting, sp2 carbon on a ferroelectric lead zirco-titanate: towards graphene synthesis on ferroelectrics in ultrahigh vacuum*, RSC Advances **6**, 67883 (2016).
- F. Presel, **C.A. Tache**, H. Tetlow, D. Curcio, P. Lacovig, L. Kantorovich, S. Lizzit, A. Baraldi, *Carbon monomers and dimers on Ir(111): and experimental and theoretical C1s core level shift study*, to be submitted.
- L. Bignardi, **C.A. Tache**, P. Lacovig, D. DeAngelis, D. Curcio, A. Baraldi and S. Lizzit, *Temperature-driven graphene growth on Ag(111) using a solid carbon source*, to be submitted.

Other paper realized during the thesis:

- L.C. Tănase, N.G. Apostol, L.E. Abramiuc, **C.A. Tache**, L. Hrib, L. Trupină, L. Pintilie and C.M. Teodorescu *Ferroelectric triggering of carbon monoxide adsorption on lead zirco-titanate (001) surfaces*, Scientific Reports **6**, 35301 (2016).

Acknowledgments

The end of this PhD would be for sure a milestone in my carrier and a life experience which I would never forget. This amazing experience wouldn't be so great if it wasn't for the people who supported me all these years.

First of all, I would like to offer my sincere gratitude to my supervisor Alessandro, for the great opportunity that he offers me three years ago to start this PhD project. And for all the continuous support, motivation and immense knowledge that guided me in all these years.

Secondly, I would like to offer a great recognition to my co-supervisor Silvano, for all the fruitful discussion, which have completed my knowledge of this research. Their guidance helped in all the time of PhD and writing of the thesis. Thank you for everything!

I would also want to offer a special thanks to my colleagues from the SuperEsca beamline and Surface Science Laboratory from Elettra. Thank you Naila, Francesco, Davide, Elisabeta, Harsh, Dario, Paolo, and Luca for all the great time spent together and for your friendship. Thank you guys! I would never forget you!

Nevertheless, I would like give a special recognition to Dr. Cristian Teodorescu and to Dr. Nicoleta Apostol from National Institute of Materials in Magurele, for all the advises, encouragements and fruitfull discussions which have contributed in the realization of this work. Also I would like to thanks to all the members in the group led by Dr. Lucian Pintilie for all the help given in the synthesis of ferroelectric substrates studied in this work.

Finally I would like to thanks my parents, for their care, love and patience during this years. I wouldn't reach this goal without their encouragement and support.

And last, to Alexandra for her love, patience and for her unconditioned

support in any decision that I made and because that I am sure that we can face any challenge together.